Source Localization by Inverse Methods (SLIM)

Jens Havskov Sørensen[1] (co-ordinator)
Henrik Feddersen[1]
Kasper Skjold Tølløse[1]
Rostislav Kouznetsov[2]
Mikhail Sofiev[2]
Heiko Klein[3]
Magnus Ulimoen[3]
Lennart Robertson[4]
Jan Pehrsson[5]
Bent Lauritzen[6]
Dan Bohr[7]
Agnieszka Hac-Heimburg[7]
Carsten Israelson[7]
Anna Maria Blixt Buhr[8]
Jonas Lindgren[8]
Tero Karhunen[9]
Tuomas Peltonen[9]

[1]Danish Meteorological Institute (DMI)
[2]Finnish Meteorological Institute (FMI)
[3]Norwegian Meteorological Institute (MET Norway)
[4]Swedish Meteorological and Hydrological Institute (SMHI)
[5]PDC-ARGOS, Denmark
[6]Technical University of Denmark (DTU)
[7]Danish Emergency Management Agency (DEMA)
[8]Swedish Radiation Safety Authority (SSM)
[9]Radiation and Nuclear Safety Authority (STUK), Finland

Abstract

In early October 2017, the IAEA was informed that low concentrations of Ru-106 were measured in high-volume air samples in Europe from routine monitoring networks. However, no information was given that an accidental release of Ru-106 had taken place. Such events signify the need for prompt and accurate responses from national radiation protection authorities in such cases. This requires that methodologies, suited for operational use, are developed for spatial and temporal localization of the source of contamination based on available monitoring data.

For operational use, nuclear decision-support systems should be extended with modules handling such monitoring data automatically, e.g. by employing EURDEP, and conveying selected data to the national meteorological centre accompanied by a request to run an atmospheric dispersion model in inverse mode. The aim would be to determine a geographical area in which to find the potential release point as well as the release period.

 The following results are obtained:

- Two case studies are identified and selected, viz. the European Tracer Experiment (ETEX-1) and the October 2017 case of Ru-106 in Europe.
- Methods for temporal and spatial source localization are developed, implemented and described.
- Deterministic NWP model data are derived from the ECMWF corresponding to the selected cases.
- Quality-controlled measurement data of ground-level concentration are obtained from filter stations.
- The inverse methods for source localization are applied by using the DERMA, MATCH and SNAP atmospheric dispersion models to both cases using the deterministic meteorological data.
- A high-resolution limited-are ensemble prediction system based on the Harmonie NWP model has been set up and applied to the two selected cases.
- The inverse methods for source localization are applied by using the DERMA, MATCH, SILAM and SNAP atmospheric dispersion models to both cases using the ensemble-statistical meteorological data.

Key words

Source Localization by Inverse Methods (SLIM) – final report

Final Report of the NKS-B SLIM activity

(Contract: AFT/B(20)3)

Jens Havskov Sørensen[1] (co-ordinator)
Henrik Feddersen[1]
Kasper Skjold Tølløse[1]

Rostislav Kouznetsov[2]
Mikhail Sofiev[2]

Heiko Klein[3]
Magnus Ulimoen[3]

Lennart Robertson[4]

Jan Pehrsson[5]

Bent Lauritzen[6]

Dan Bohr[7]
Agnieszka Hac-Heimburg[7]
Carsten Israelson[7]

Anna Maria Blixt Buhr[8]
Jonas Lindgren[8]

Tero Karhunen[9]
Tuomas Peltonen[9]

[1]Danish Meteorological Institute (DMI)

[2]Finnish Meteorological Institute (FMI)

[3]Norwegian Meteorological Institute (MET Norway)

[4]Swedish Meteorological and Hydrological Institute (SMHI)

[5]PDC-ARGOS
[6]Technical University of Denmark (DTU)

[7]Danish Emergency Management Agency (DEMA)

[8]Swedish Radiation Safety Authority (SSM)

[9]Radiation and Nuclear Safety Authority (STUK)

Table of contents

Introduction

In early October 2017, the International Atomic Energy Agency (IAEA) was informed by Member States that low concentrations of Ru-106 were measured in high-volume air samples in Europe from routine monitoring networks. However, no information was given that an accidental release of Ru-106 had taken place. Such events, indicating the release of anthropogenic radionuclides to the environment, signify the need for prompt and accurate responses from national radiation protection authorities. This requires that methodologies, which are suited for operational use, are developed for spatial and temporal localization of the source of contamination based on available monitoring data.

For operational use, nuclear decision-support systems (DSSs) should be extended with modules handling such monitoring data automatically, e.g. by employing the European Radiological Data Exchange Platform (EURDEP), and conveying such data to the national meteorological centre accompanied by a request to run an atmospheric dispersion model in inverse mode, i.e. to run the adjoint model backwards in time. The aim would be to determine a geographical area in which to find the potential release point, the release period, and possibly the quantities of radionuclides released to the environment.

In the SLIM project, the following results are obtained:
- Two case studies are identified and selected, viz. the ETEX-1 and the October 2017 case of Ru-106 in Europe.
- Methods for temporal and spatial source localization are developed, implemented and described. The methods can be applied both to a deterministic weather prediction model data set, and to an ensemble-statistical data set the describing the inherent meteorological uncertainties.
- Quality-controlled measurement data of ground-level concentration are obtained.
- Deterministic numerical weather prediction (NWP) model data are derived from the European Centre for Medium-Range Weather Forecasts (ECMWF) corresponding to the selected cases.
- The inverse methods for source localization are applied by using the DERMA, MATCH and SNAP atmospheric dispersion models to both case studies using the deterministic meteorological data.
- A high-resolution limited-area ensemble prediction system based on the Harmonie numerical weather prediction model has been set up and applied to the two selected cases.
- The inverse methods for source localization are applied with the DERMA, MATCH, SILAM and SNAP atmospheric dispersion models to both cases using the ensemble-statistical meteorological data.

In the previous NKS-B project MUD (Sørensen *et al.,* 2014), a methodology was developed for quantitative estimation of the uncertainty of atmospheric dispersion modelling stemming from the inherent uncertainties of meteorological model predictions. Subsequently, in the projects FAUNA (Sørensen *et al.,* 2016) and MESO (Sørensen *et al.,* 2017), the implications for nuclear emergency preparedness and management were studied also for short-range models and by applying the methodology to the Fukushima Daiichi emergency. Furthermore, a methodology was developed in the AVESOME project (Sørensen *et al.,* 2019; 2020) quantifying the combined effects of uncertainties of the source-term descriptions and the meteorological data on atmospheric dispersion prediction. Means to implement the uncertainties in DSSs, and the impacts on real-time emergency management, were described.

Atmospheric Dispersion Models

Danish Emergency Response Model of the Atmosphere (DERMA)

The Danish Emergency Response Model of the Atmosphere (DERMA) (Sørensen *et al.,* 2007; Sørensen, 1998) is a comprehensive numerical regional and meso-scale atmospheric dispersion model developed at the Danish Meteorological Institute (DMI). The model is used operationally for the Danish nuclear emergency preparedness, for which the Danish Emergency Management Agency (DEMA) is responsible (Hoe *et al.*, 2002). Besides, the model is employed for veterinary emergency preparedness (Sørensen *et al.*, 2000; 2001; Mikkelsen *et al.*, 2003; Gloster *et al.,* 2010a; 2010b), where it is used for assessment of airborne spread of animal diseases, e.g. foot-and-mouth disease. DERMA may also be used to simulate atmospheric dispersion of chemical substances, biological warfare agents and ashes from volcanic eruptions, and it has been employed for probabilistic nuclear risk assessment (Lauritzen *et al.,* 2006; 2007; Baklanov *et al.*, 2003; Mahura *et al.*, 2003; 2005).

The main objective of DERMA is to predict the dispersion of a radioactive plume and the accompanied deposition. However, the model may also be used in situations where increased levels of radioactivity have been measured but no information is revealed on a radioactive release. In such cases, inverse (adjoint) modelling may be applied whereby potential sources of radioactivity may be localised and release rates estimated.

The three-dimensional model is of Lagrangian type making use of a hybrid stochastic particle-puff diffusion description, and it is currently capable of describing plumes at downwind distances up to the global scale (Sørensen *et al.*, 1998). The model utilizes aerosol size dependent dry and wet deposition parameterisations as described by Baklanov and Sørensen (2001).

Currently, DERMA makes use of analysed and forecasted meteorological data of various deterministic versions at DMI of the NWP model Harmonie (Bengtsson *et al.,* 2017) covering North-western Europe, Greenland and the Faeroes, and from the global model developed and operated by the European Centre for Medium-range Weather Forecasts (ECMWF). Further, DERMA utilizes the COMEPS ensemble prediction system, which is based on the Harmonie model.

DERMA is interfaced with the Accident Reporting and Guidance Operational System (ARGOS) (Hoe *et al.,* 1999; 2002), a PC based nuclear decision-support system developed by the Prolog Development Center (PDC). The integration of DERMA with the ARGOS system is effectuated through automated online digital communication and exchange of data between the ARGOS system and the DMI High Performance Computing (HPC) facility.

Multi-scale Atmospheric Transport and Chemistry model (MATCH)

The Multi-scale Atmospheric Transport and Chemistry model (MATCH) (Robertson *et al.,* 1999) is multi-purpose Eulerian chemical transport model (CTM) developed by the SMHI. The model is used for emergency application such as nuclear and natural events (volcanos), aerosol dynamics and optics (Andersson *et al.,* 2015), complex chemistry, and data assimilation (Robertson and Langner, 1998; Kahnert, 2008; Kahnert, 2018). The MATCH model is used operationally for chemical forecasts in CAMS (Copernicus Atmospheric Monitoring Service) and for SSM (Swedish Radiation Safety Authority) serving the ARGOS system needs (Hoe *et al.,* 1999; 2002). Other applications are studies for air quality and health

issues in climate projections. In most applications MATCH is used as a limited-area model on various possible scales, but also for global applications.

The MATCH model is basically an Eulerian model but for emergency applications a Lagrangian particle model is used in the near field of the emission location.

A wide range of possible driving meteorological data is applicable like analyses and forecasts from HARMONIE, IFS (ECMWF) and WRF.

System for Integrated modeLling of Atmospheric coMposition (SILAM)

SILAM (System for Integrated modeLling of Atmospheric coMposition, , last access: 5 Jan 2021) is an offline 3D chemical transport model (Sofiev *et al.,* 2015). SILAM features a mass-conservative positive-definite advection scheme that makes the model suitable for long-term runs. The model can be run at a range of resolutions starting from a kilometre scale in a limited-area up to a global coverage. The vertical structure of the modelling domain consists of stacked layers starting from the surface. The layers can be defined either in z- or hybrid sigma-pressure coordinates. The model can be driven with a variety of NWP (numerical weather prediction) or climate models.

The model is used for emergency-response applications and includes radioactive transformation mechanism and various passive tracers.

Severe Nuclear Accident Program (SNAP)

The Norwegian Meteorological Institute (MET-Norway) is responsible for modelling atmospheric dispersion of radioactive debris in the event of a nuclear emergency related to a nuclear accident or detonation. An additional task of the MET-Norway in a nuclear emergency is to identify unknown sources of radiation indicated by elevated levels of measurement. The basic tool used by the MET-Norway for such events is the Severe Nuclear Accident Program (SNAP) (Bartnicki *et al.,* 2011; Klein and Bartnicki, 2018).

The SNAP model was developed at the MET-Norway in 1994 as a Lagrangian particle model. The present version is fully operational at the MET-Norway and takes into account atmospheric transport and deposition of gases, noble gases and particles of different size and density emitted during nuclear accidents or explosions. SNAP can also be run remotely by experts from the Norwegian Radiation and Nuclear Safety Authority (DSA) where the Norwegian Crisis Committee is located.

Once released into the air, radioactive gases and particles are subject to advection, turbulent diffusion and deposition (dry and wet). In the SNAP calculations, the advection process is immediately followed by the diffusion process. A random walk approach is used to parameterise horizontal and vertical diffusion. When large and dense particles are released, gravitational settling is more effective than vertical diffusion, and this process is taken into account. The SNAP model has been used both for simulations of historical events, e.g. nuclear detonations in Novaya Zemlya, Chernobyl Accident (Bartnicki *et al.,* 2016), and real-time simulations, e.g. the Fukushima accident. It was tested in the ETEX-1 experiment and showed good agreement with observations (Saltbones *et al.,* 1998). SNAP is the dispersion model currently used by the MET-Norway in the Center of Excellence: CERAD CoE.

ETEX-1

After the Chernobyl accident in April 1986 and the adoption of the Convention on Early Notification of a Nuclear Accident (IAEA, 1986), the International Nuclear Safety Advisory Group (INSAG) of the International Atomic Energy Agency (IAEA) recommended inter alia that the IAEA should, in collaboration with the World Meteorological Organisation (WMO), review and intercalibrate the models of atmospheric transport of radionuclides over short and long distances and of radionuclide deposition on terrestrial surfaces, and establish a database for validation studies of these models.

Following this recommendation, the joint IAEA/WMO Atmospheric Transport Model Evaluation Study (ATMES) was initiated in November 1986. The objective of ATMES was to compare the evolution of the radioactive cloud (I-131 and Cs-137) with the evolution predicted by mathematical models for atmospheric dispersion, using as input only the estimated source term of the Chernobyl accident.

The ATMES suffered, however, from a number of weaknesses regarding lack of monitoring data and large uncertainties regarding the source term. Therefore, it was decided to carry out a tracer experiment in Europe. The sponsoring organisations were the European Commission (EC), the World Meteorological Organization (WMO) and the International Atomic Energy Agency (IAEA), and later joined by the US Department of Energy (USDOE).

The experiment was named ETEX, European Tracer Experiment (Graziani, Klug and Nodop, 1998; ETEX web-site, 2019). It was designed to test the readiness of interested services to respond in the case of an emergency, to organise the tracer release and compile a data set of measured air concentrations and to investigate the performance of long-range atmospheric transport and dispersion models using that data set. In total, thirty-six organisations around the world were involved in the project.

Sampling network

The sampling network consisted of 168 ground-level sampling stations in western and eastern Europe. National meteorological services hosted the samplers at a number of WMO synoptic stations over their territory. Thus, ETEX could take advantage of this existing network, which is homogeneously distributed throughout Europe and linked to the WMO.

A final number of 168 sampling stations were selected, almost all located at existing WMO stations. Three samplers were located in the North Sea: one on a Dutch oil platform, the other two on gas platforms. The average spacing between two sampling stations in the resulting configuration was about 80 km.

Each station was labelled with one or two letters identifying the Country where it was located, and numbered sequentially.

It was planned to start the sampling operations at each station about 6 hours before the expected time of tracer arrival to obtain contemporaneous measurements of the tracer background levels and to ensure that the plume arrival was not missed. Each station was designed to sample over a period of 72 consecutive hours (24 three-hour samples), with sampling starting time progressively delayed from West to East. The stations closest to the source started sampling 3 hours before the release start; the most distant stations ended sampling 90 hours after the release start. The sampling network is depicted in Figure 1.
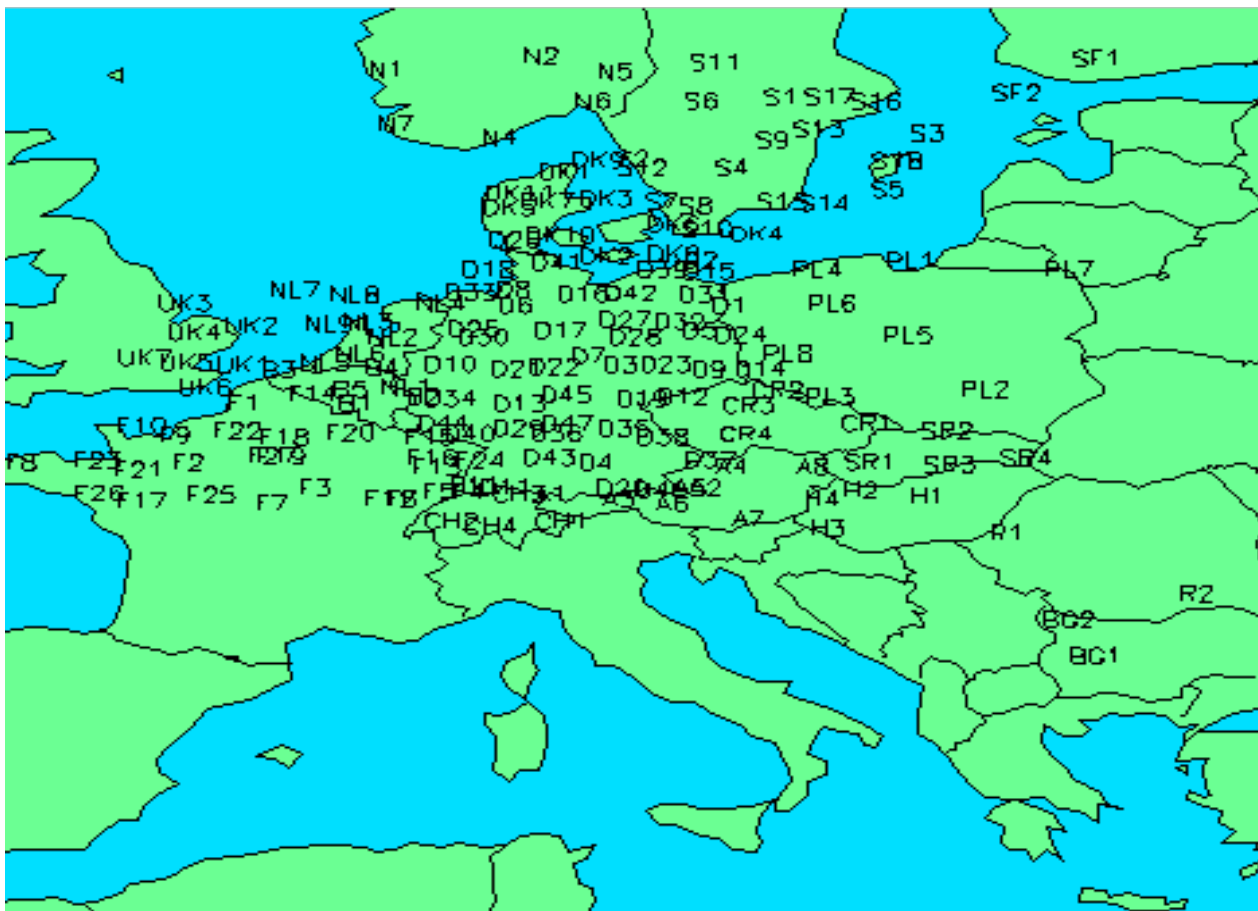
Figure 1 ETEX Sampling network (ETEX web-site, 2019).

Synoptic situation

Weather predictions suggested the following conditions on Sunday 23 October, 1994:

- the presence of a rather strong West to South-westerly flow, advecting the tracer during the experiment over several tracer stations
- no centre of high- or low-pressure, and no extending ridges or troughs, would have passed close to the release site
- no frontal systems would have passed the release site shortly before, during or after the release

Therefore, on Friday 21 October, 1994, the alert procedure was started.

23 October, 1994

A deep low, 975 hPa, to the East of Scotland was slowly moving north, maintaining a strong south-westerly flow over the release-site (Rennes). The advected air was unstable, with showers, some accompanied by thunder and squall-lines. Similar observations could be made from satellite pictures. The 12:00 UTC radio sounding of Brest showed a temperature profile which was unstable with respect to moist air, allowing the development of shower clouds up to about 28000 ft. Also the radio sounding of Paris showed an unstable atmosphere but with lower water vapour content. At both locations, the upper winds were Southwest and rather strong. The release started at 16:00 UTC.

24 October, 1994
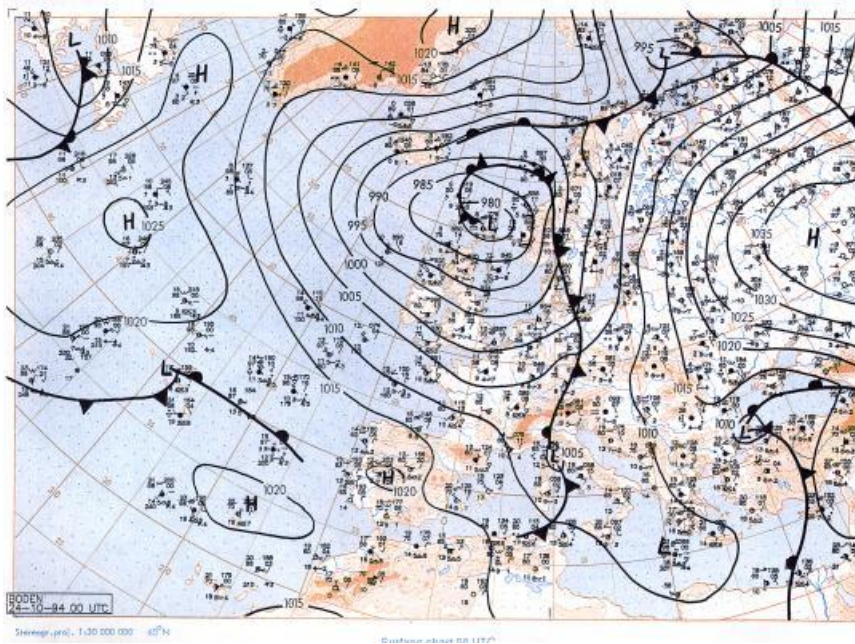
Figure 2 24 October, 1994, 00 UTC (ETEX web-site, 2019).

There was still an unstable flow over the release site and the advection area. However, because of the northerly movement of the controlling low over the North Sea, the wind in the advection area decreased. The expected cold front was to be seen south of Ireland.

25 October, 1994
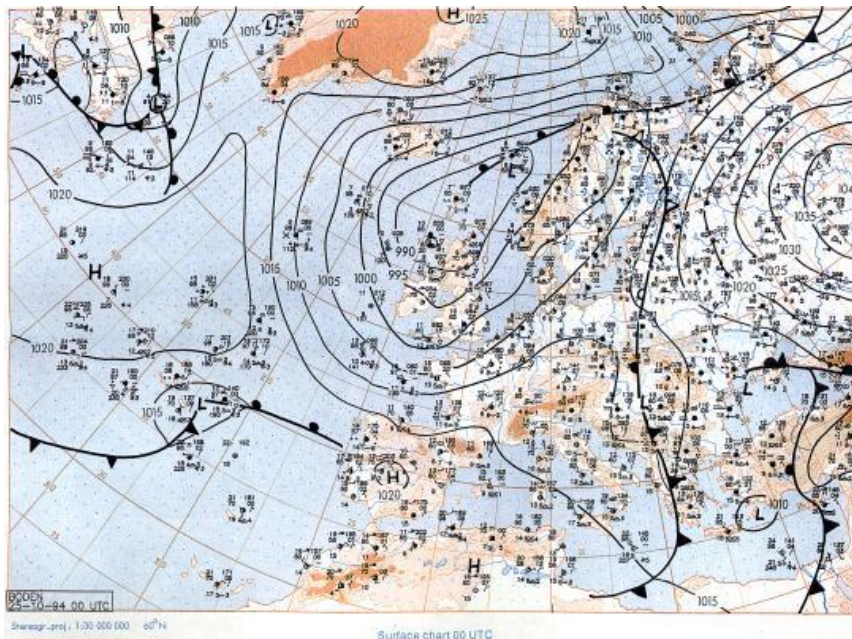
Figure 3 25 October, 1994, 00 UTC (ETEX web-site, 2019).

The further deepening of the mentioned cold front had not developed. The system was to be seen as a minor secondary low, at 52°N, 5°E. The cold front over The Netherlands, an instability front with showers, had the pressure pattern of a trough. The wind was backing more to the south with the approach of the front during the day, and after the passage of this front the wind was veering to the Southwest.

26 October, 1994
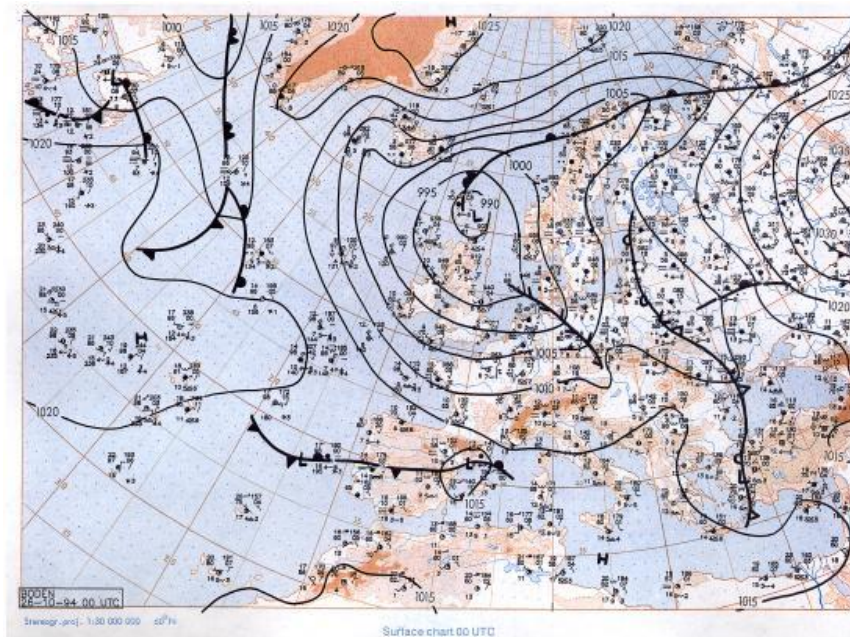
Figure 4 26 October, 1994, 00 UTC (ETEX web-site, 2019).

There was still a complex low-pressure system over the North Sea and Scotland. Shower weather with a wind tending to veer a bit over Western Europe towards west-southwest. The high-pressure cell over the Black Sea indicated that southerly winds could block any further movements of the tracer cloud towards the East.

Tracer release

Atmospheric tracers were released in the form of a homogeneous air stream containing a few percent of perfluoromethylcyclohexane (PMCH) tracer. The gas stream passed through a small chimney where the gas was released at the top.

The release started at 16:00 UTC on October 23, 1994, and lasted 11 hours and 50 minutes. 340 kg of the non-depositing inert gas PMCH (perfluoromethylcyclohexane) were released from Monterfil (48°03'30"N, 2°00'30"W) at an average flow rate of 8.0 g/s.

Harmonie Ensemble Prediction System runs

The two ensemble experiments were run using a special version of HarmonEPS, the HARMONIE ensemble prediction system developed by the HIRLAM consortium (Frogner *et al.,* 2019). In order to afford running ensemble experiments on the two relatively large domains, a hydrostatic configuration, using ALARO physics (Termonia *et al.,* 2018), was chosen. ALARO was developed by the ALADIN consortium to handle resolutions in the "grey zone" between meso-scale and convection-permitting and has been run operationally by a number of ALADIN members.

For the SLIM experiments, we chose an ensemble size of 21 members (1 control + 20 perturbed members). With this ensemble size, we can afford a horizontal resolution of 5 km × 5 km and 65 vertical levels up to 10 hPa. The model is run on a Lambert conformal conic projection grid, all members run surface data assimilation, and for the control member it is blended with upper air data from the ERA5 reanalysis (Hersbach *et al.,* 2020). The initial condition perturbations are based on random field perturbations (Schubert and Suarez, 1989;

Magnusson *et al.,* 2009), i.e. they are created by scaling the difference between two ERA5 model states that are picked from two random dates (same time of the year and same time of the day) and interpolated to the 5 km Lambert grid. The perturbations are then added to or subtracted from the blended analysis of the control member. The scaling factor is determined so that the total energy of the perturbation (Keller *et al.,* 2008) is similar to that used for operational forecasts at DMI. A similar approach is used to perturb the lateral boundary conditions where we use model states of the short ERA5 forecasts. ERA5 ensemble forecasts are also available, but the ensemble size is only 10, so instead we use random field perturbations that can easily be generated in a much higher number than we need here. The forecast length of the ensemble members is 18 h, and new ensemble forecasts are run every 12 h, following the ERA5 forecasts, i.e. with initial times at 06 and 18 UTC. The domains for the ETEX-1 and Ru-106 experiments are shown in Figure 5. Output parameters from the HARMONIE-ALARO ensemble include temperature, wind, specific humidity, cloud water and cloud ice on all 65 model levels as well as a number of 2d variables, including surface pressure, total cloud cover, mixing layer depth and total precipitation.
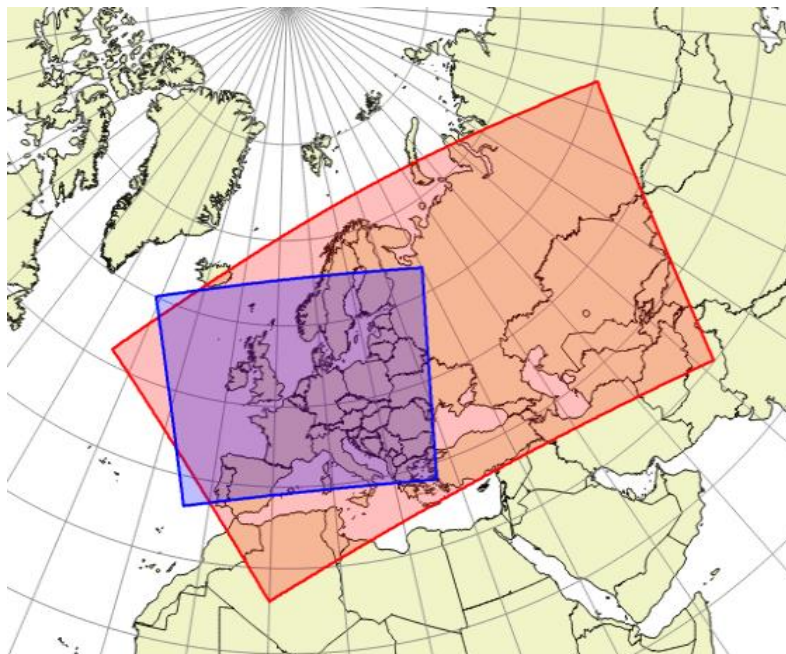
Figure 5 HARMONIE-ALARO domains for the ETEX-1 (blue) and Ru-106 (red) experiments.

Harmonie Ensemble Prediction System runs for ETEX-1

For the ETEX-1 experiment, the HARMONIE-ALARO ensemble forecasts cover the period 22–28 October 1994 following a spin-up period from 15–22 October. The figures in the following illustrate the spread in the ensemble. Figure 6 and Figure 7 show mean sea level pressure and 10 m wind for 9 h forecasts of the control run and the 20 perturbed members valid on 15 UTC 23 October 1994, i.e. one hour before the tracer gas release in Rennes. The variation of the perturbed members indicate the ensemble spread.

MSLP 1994102306+09h
Valid on Sunday 23 Oct 15:00 UTC
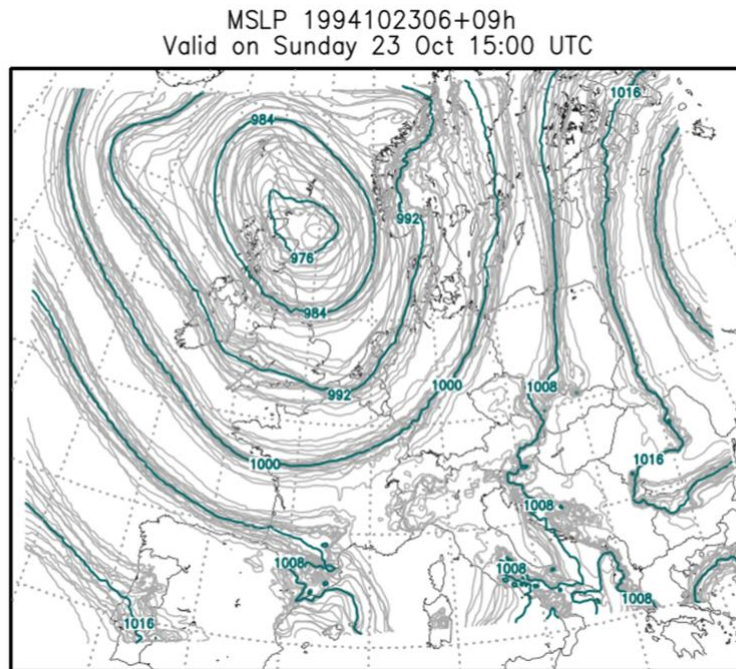
Figure 6 Mean sea level pressure spaghetti plot valid one hour prior to the release in Rennes. Unperturbed control run is coloured, the 20 perturbed members are grey.

10m wind 1994102306+09h
Valid on Sunday 23 Oct 15:00 UTC
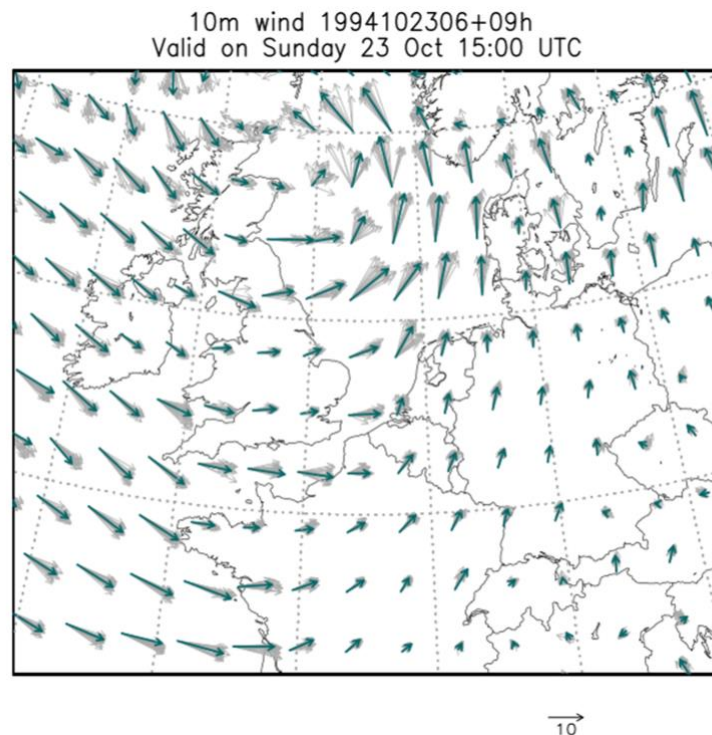
Figure 7 As Figure 6, but for 10 m wind vectors. The magnitude of a 10 m/s vector is shown in the legend.

Figure 8 shows 3-hourly precipitation around the release time for all members in the ensemble. We note that all members have showers downstream of the release, but the exact location and intensity vary.
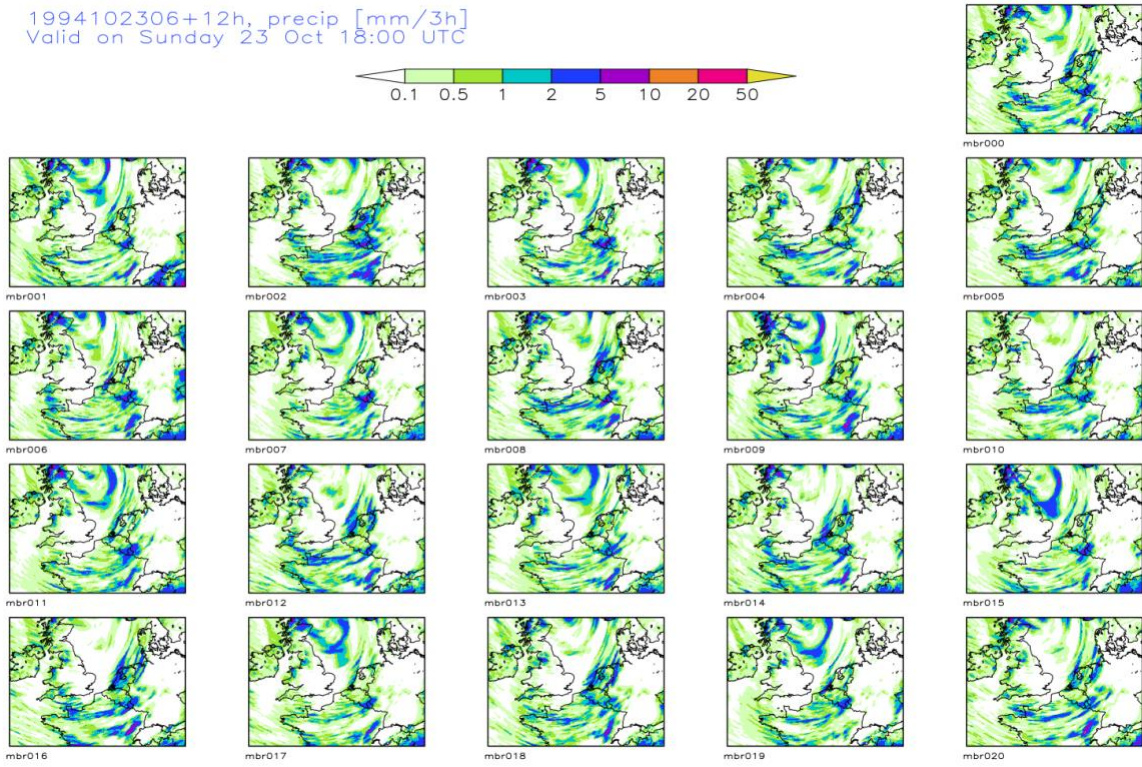
Figure 8 Precipitation "postage stamp" valid from 15–18 UTC 23 October 1994 for the control run (mbr000) and the 20 perturbed members.

Deterministic results of DERMA

For each of the ETEX-1 filter station measurements corresponding to non-zero three-hour average tracer concentrations (in total 939 data), i.e. omitting any measurement data below threshold, the DERMA model has been run in inverse mode backwards in time using a negative time step (Sørensen, 2018). Thereby the whereabouts of the released substance, PMCH, is estimated before arriving at the filter stations (Rao, 2007; Pudykiewicz, 1998); see Figure 9 for a few examples. The observed time-average concentration values are used by the dispersion model by tracing PMCH back in time from the filter stations at measurement heights with start concentration values within the averaging time periods given by the measured average values. We assume that the detected PMCH originates from the same geographically fixed ground-level release location allowing for the release to have taken place during a finite time period.

Model calculated influence functions, e.g. concentration, are shown at 2 m above ground. Obviously, the influence functions extend further in the vertical, but concentration values aloft are not shown here. As depicted in Figure 9, individual measurements do not pin-point the location of the potential release point giving rise to extended geographical sectors only. However, by identifying the intersection, or overlap, of the inverse plumes, one obtains a better localization. The slight inconsistencies between some of the inverse plumes may well be accounted for by the inherent meteorological uncertainties.
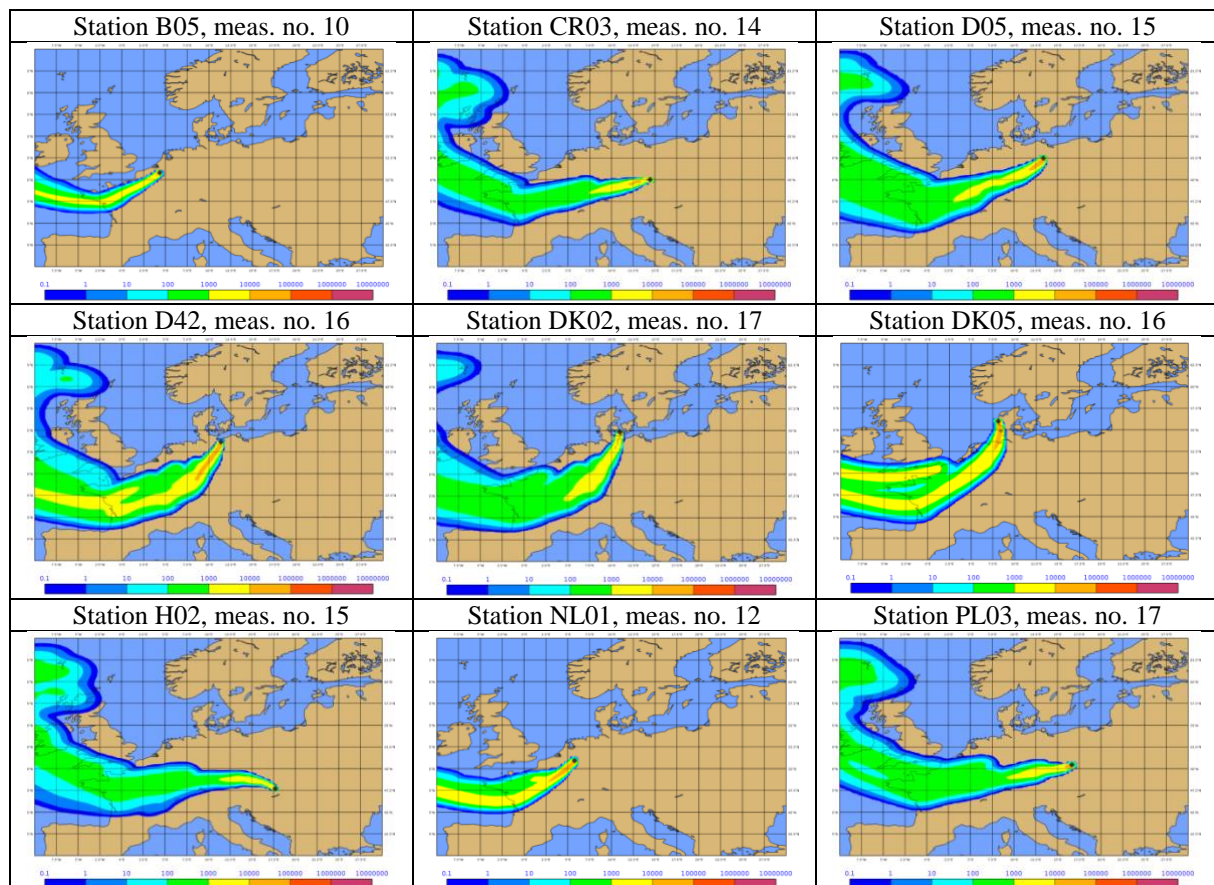

Figure 9 Time-integrated 2-m concentration in arbitrary units of inverse PMCH plumes valid at 1994-10-22, 06 UTC. The filter stations are indicated by black diamonds. For a given filter station, the measurement number (meas. no.) indicates the data point used in the 30-member time series of three-hour average concentration values measured.

In the following, both the temporal and the spatial behaviour of the inverse plumes are studied, i.e. the concentrations are correlated both in time and space. We are attempting to identify the geographic and temporal intersection of the plumes, since a release from the intersection will influence all stations with measurement valuess above the detection limits. This methodology resembles the variational approach applied to the adjoint of an Eulerian model presented by Robertson and Langner (1998) and Robertson (2004). The origin of this approach is a single iteration in the variational approach where the gradient of the model error is determined by the observations. Seibert (2000, 2001, 2002) used a Lagrangian model run in backward mode to determine the source, e.g. in the context of the Comprehensive Nuclear-Test-Ban Treaty (CTBT).

Considering the ensemble of individual inverse plumes, one may apply ensemble statistical methods to the results of forward dispersion calculations for a numerical weather prediction ensemble combined with a source-term ensemble describing the inherent meteorological and source-term uncertainties, cf. Sørensen *et al.* (2019). One may e.g. calculate the ensemble average of each time step involved in the time series of inverse instantaneous concentrations, cf. Figure 10. The ensemble average is not ideal for localizing the release point. However, it is useful for illustrating the mechanism of the inverse methodology.
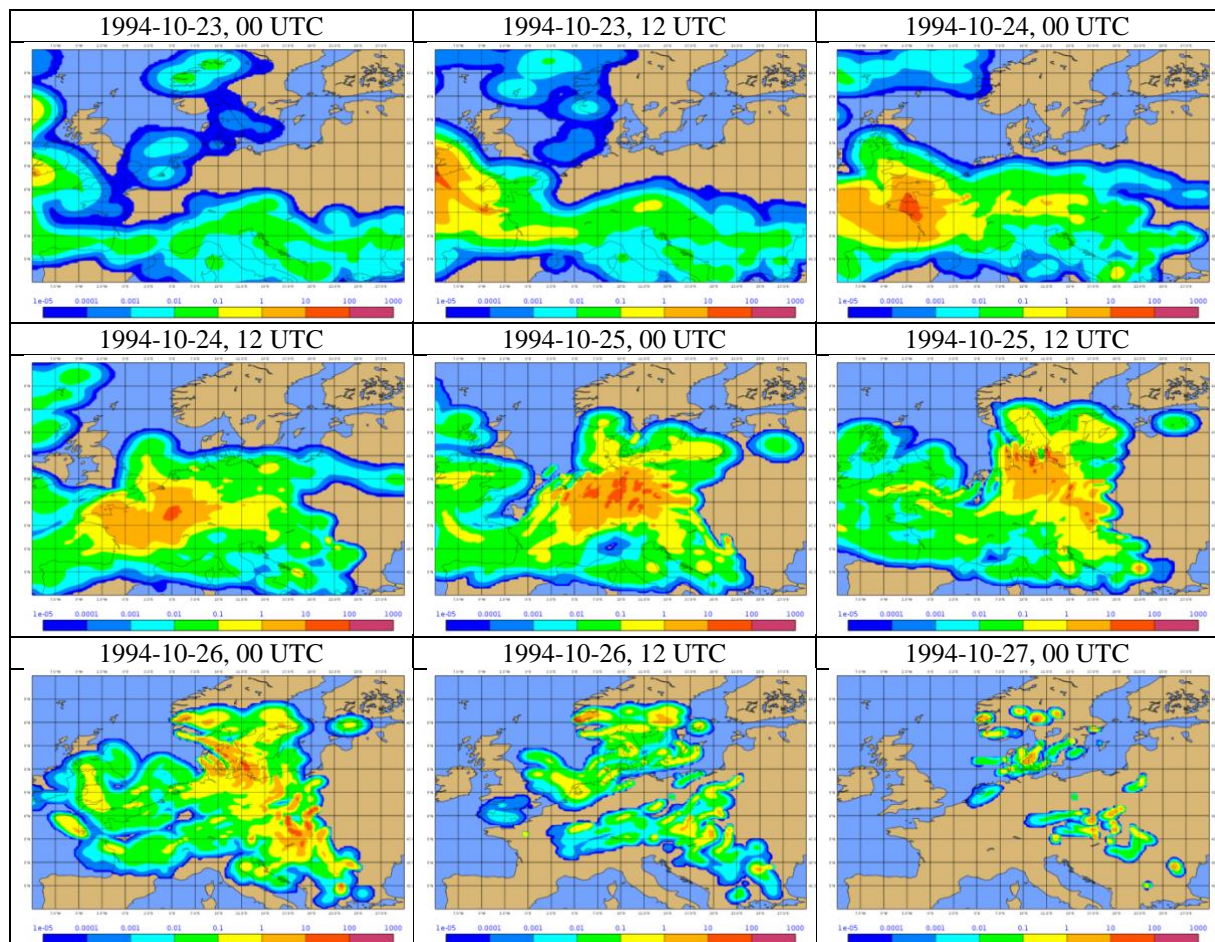
Figure 10 Time series of the set of ensemble-average inverse concentration values corresponding to the filter station measurements.

The release is assumed to have taken place from a ground-level location which can be found in the overlap of the instantaneous inverse concentration plumes. With accurate measurements

representing the plume well both geographically and temporally, this overlap can be described in terms of the ensemble percentiles. It should, however, be noted that in the early phase of an accidental release where only few measurements are available, the problem is likely to be ill-conditioned.

For operational use, the best percentage value to be used for the quantile calculation is not known a priori. This value depends on how well-conditioned the problem is, i.e. how well the observations match the plume geographically and temporally, as well as on the distribution of the measured average concentration data. Thus, the recommendation is to calculate a range of percentiles, which is feasible from a computational point of view. By employing the percentile method, outliers are disregarded, and effectively a level-of-agreement approach is applied.

Low concentration values close to the detection limit or close to a potentially fluctuating background pose a difficulty due to the large relative uncertainties involved. In general, it is likely that such measurements do not represent the actual release but instead fluctuations in the background. On the other hand, there might be valuable information in such low or zero-value measurements. Imposing a threshold concentration value for the calculations aiming at localizing the point source, and thereby disregarding information, requires knowledge of the detection limits for the stations involved. For the current scenario involving PMCH, the natural background value is expected to be close to zero, and in the calculations presented here, all non-zero measurement data are included.

In Figure 11, the time series of the 70th percentile of the set of inverse concentration values is shown corresponding to the filter station measurements.
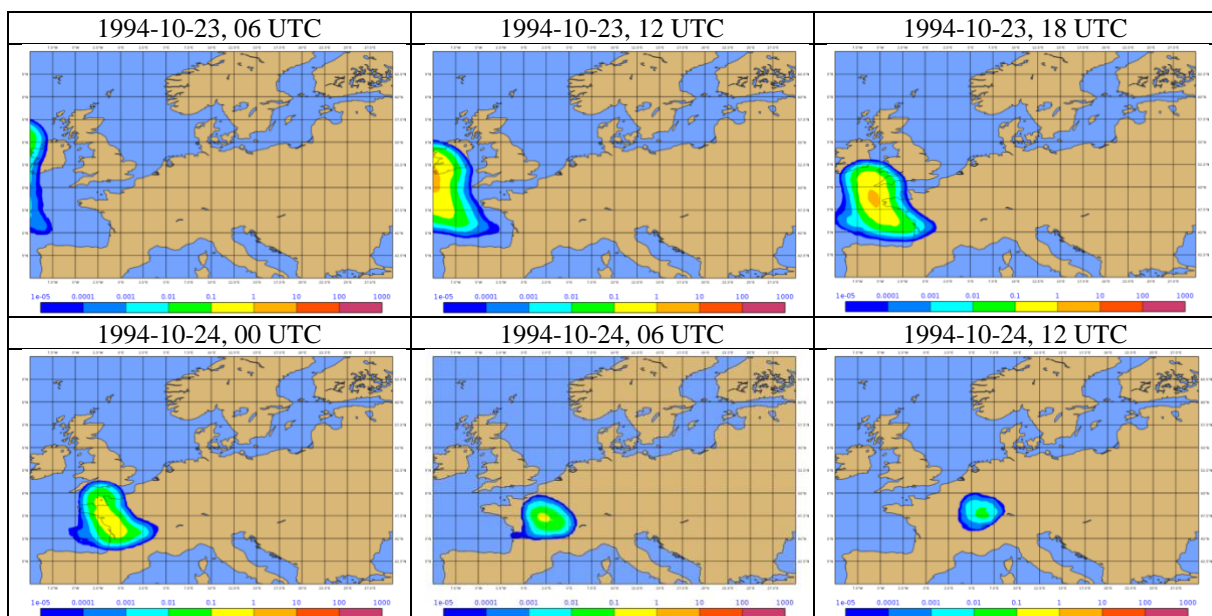
Figure 11 Time series of the 70th percentile of the set of inverse concentration values corresponding to the filter station measurements.

According to the calculated percentile maps, the release point should be found in western France in regions Brittany, Normandy or Pays de la Loire, or in the Celtic Sea. Further, the model calculations show that a release from the actual ETEX release site in Brittany near Rennes should have taken place between around 15 UTC on 23 October and 3 UTC on

24 October. The actual release started at 16 UTC on 23 October, and lasted until 4 UTC on 24 October.
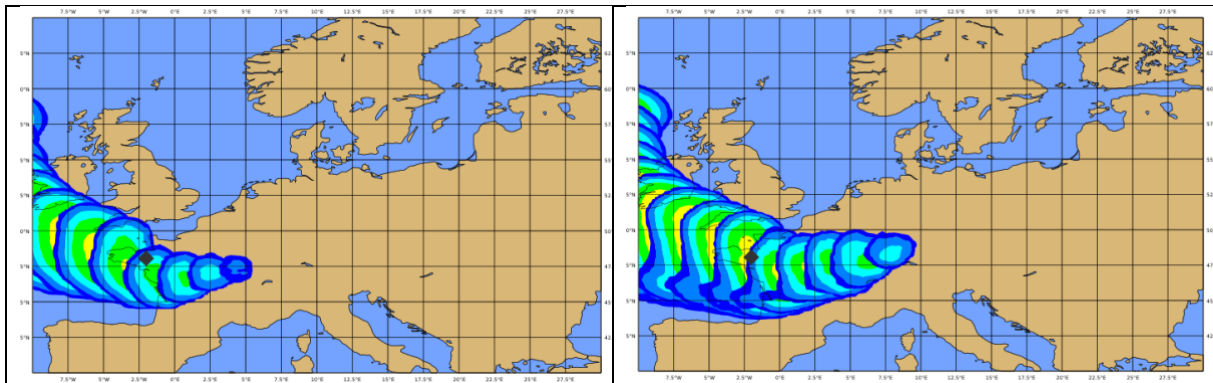
Figure 12 Estimates of the potential location of the release site. The left-hand figure consists of the overlapping time series of three-hourly 60th percentile inverse concentration maps, the right-hand figure 70th percentile maps. The maps range from 1994-10-23, 00 UTC, to 1994-10-24, 15 UTC. With a black diamond, the ETEX release point is indicated.

The time series of these 60th percentile maps has been combined in one plot in the left panel of Figure 12, which thereby depicts the estimate of the potential location of the release of PMCH. In the right panel, the corresponding figure using the 70th percentile maps is shown. The larger the percentage used for the percentile, the larger the disagreement between the individual inverse concentration calculations corresponding to measured values is accepted.

From a computational point of view, the method for point source localization is very efficient on a high-performance computing (HPC) facility. This is due to the independency between the backward calculations corresponding to each of the measurement data, which implies that the scalability, i.e. the level of parallelization, is at optimum. The parallelization can either be integrated in the dispersion model employed, or be obtained by running the model natively in parallel for each measurement. The former, which is employed by DERMA, is preferable due to the reduction of the amount of input data (the three-dimensional numerical weather prediction model data), which for the latter will have to be repeated for each measurement.

Ensemble-statistical results of DERMA

For each of the ensemble prediction model members described in section "Harmonie Ensemble Prediction System runs", the DERMA atmospheric dispersion model system has been set up to run in inverse mode using the same observational data set as described in the previous section. This amounts to 939 non-zero observational data which multiplied by 21 ensemble members equals nearly twenty thousand time series of inverse concentration fields, which constitutes the input to the localization procedures.

Overlap method

The overlap method (Sørensen, 2018) is applied to the combined set of 19,719 time series of inverse instantaneous concentration fields, and percentiles are calculated.
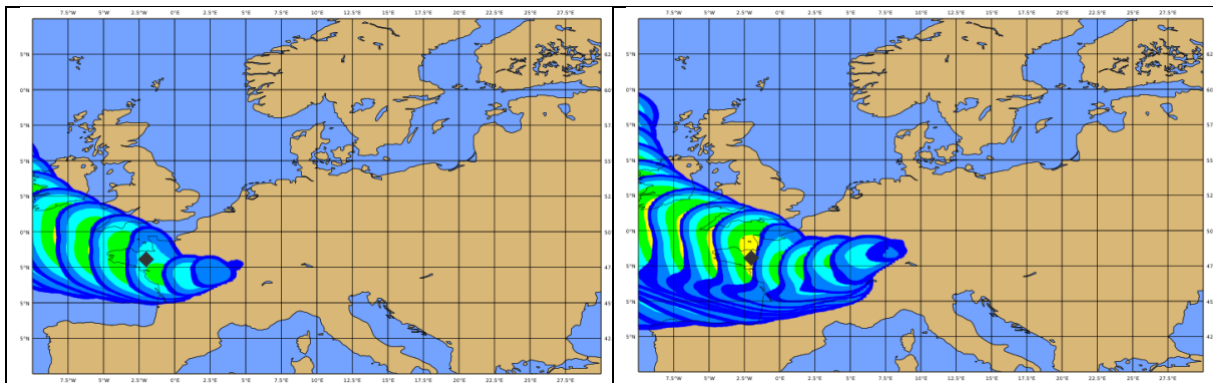
Figure 13 Estimates of the potential location of the release site using the NWP model ensemble. The left-hand figure consists of the overlapping time series of three-hourly 60th percentile inverse concentration maps, the right-hand figure 70th percentile maps. The maps range from 1994-10-23, 00 UTC, to 1994-10-24, 15 UTC. With a black diamond, the ETEX release point is indicated.

In the left-hand side of Figure 13 are shown the time series of the 60th percentile maps combined in one plot, which thereby depicts the estimate of the potential location of the release of PMCH. In the right-hand side is shown the corresponding figure using the 70th percentile maps.

The geographic zones depicted in Figure 13 agree well with the corresponding zones estimated by the deterministic calculation, Figure 12.

As for the deterministic results of DERMA, according to the calculated percentile maps, the release point should be found in western France in regions Brittany, Normandy or Pays de la Loire, or in the Celtic Sea. Further, the model calculations show that a release from the actual ETEX release site in Brittany near Rennes should have taken place between around 15 UTC on 23 October and 3 UTC on 24 October. The actual release started at 16 UTC on 23 October, and lasted until 4 UTC on 24 October.

In Figure 14 are shown similar results, for each of the individual meteorological ensemble members. From this multi-plot, the effects of the inherent meteorological uncertainties on the localization of the source can be readily seen.
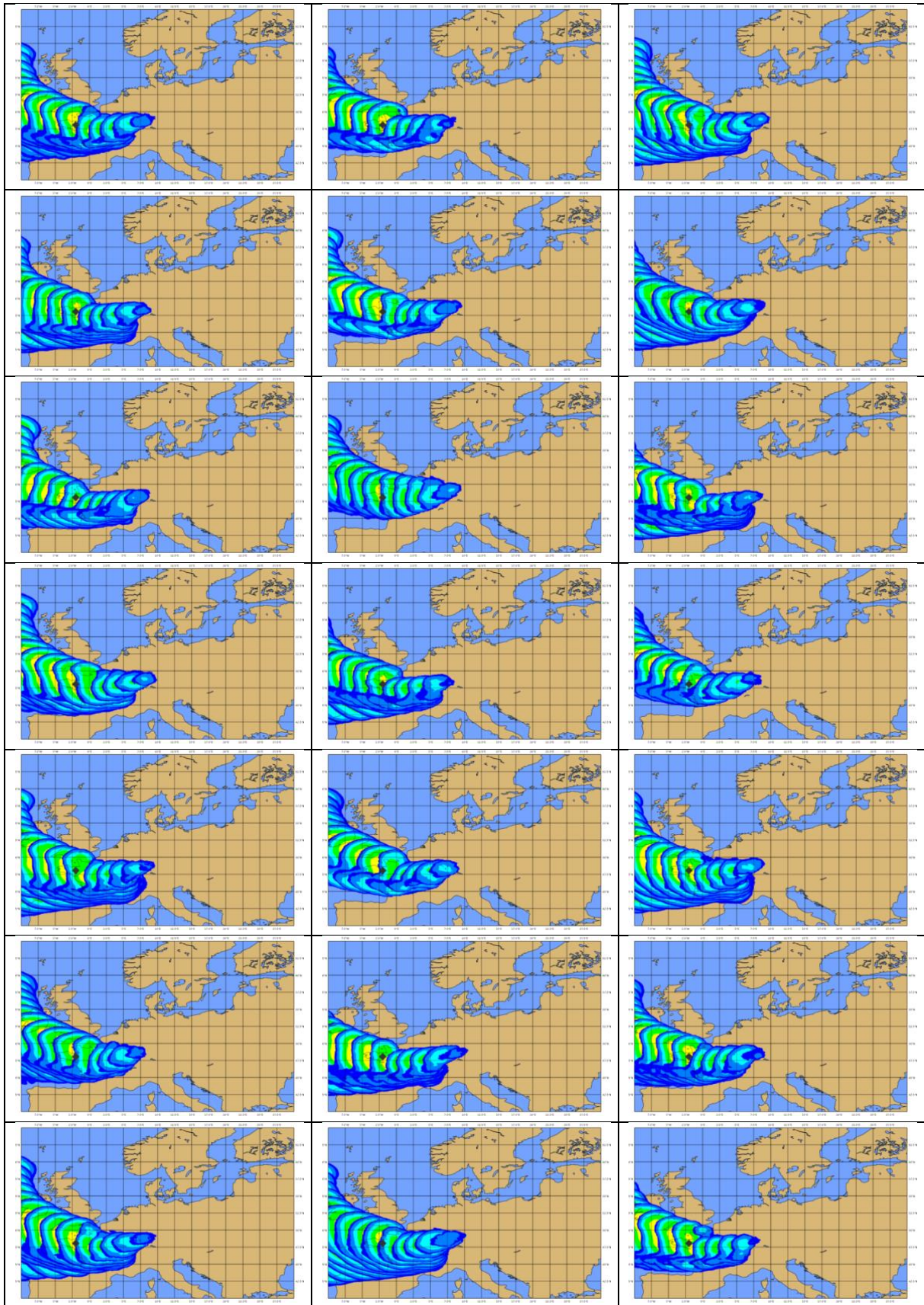
Figure 14 Estimates of the potential location of the release site for each of the NWP model ensemble members. For details, cf. Figure 13.

Bayesian inversion combined with an adjoint dispersion representation

To further restrict the location of the source, Bayesian inference is used to quantify the probability of different source locations. Examples of usage of Bayesian inference for source localization include Keats *et al.* (2006; 2008).

First, a source term model is defined as a vector containing all relevant source term parameters, $\boldsymbol{m} = (\boldsymbol{x}, \boldsymbol{q})$, where $\boldsymbol{x}$ is the coordinates of the source location, and $\boldsymbol{q}$ is a vector describing the temporal evolution of the release. Here, we have chosen a quite simple source description, where the release rate is assumed constant, such that $\boldsymbol{q} = (t_s, \Delta t, Q)$, i.e. start time, duration and release rate. The probability distribution for $\boldsymbol{m}$ is obtained by Bayes' theorem

$$P(\boldsymbol{m}|\boldsymbol{d}, I) = \frac{P(\boldsymbol{m}|I)P(\boldsymbol{d}|\boldsymbol{m}, I)}{P(\boldsymbol{d}|I)},$$

where $\boldsymbol{d}$ is a vector containing all the observations, and I is any available background information about the source. $P(\boldsymbol{m}|\boldsymbol{d}, I)$ is the *posterior* probability distribution for the source term parameters, $P(\boldsymbol{m}|I)$ is the *prior* probability distribution for the source term parameters, and $P(\boldsymbol{d}|\boldsymbol{m}, I)$ is the likelihood (the probability of observing $\boldsymbol{d}$ given a proposed source term model $\boldsymbol{m}$), and $P(\boldsymbol{d}|I)$ is a normalization constant called the evidence. The posterior probability distribution can be sampled using Markov Chain Monte Carlo (MCMC) methods, such as Metropolis-Hasting or Gibbs (Hastings, 1970; Casella and George, 1992). The basic idea behind these methods is to iteratively propose source term models and *accept* them with a probability proportional to $P(\boldsymbol{m}|\boldsymbol{d}, I)$. When a sufficient number of models are accepted, the posterior statistics can be extracted from the selection of accepted models. Traditionally, this requires a forward model, which relates the source term model $\boldsymbol{m}$ to a set of expected/ modelled detections, $\boldsymbol{R}$. This means that each MCMC iteration requires a run with the dispersion model using the proposed source term. However, it is possible to instead relate $\boldsymbol{R}$ to a set of adjoint concentration fields C_i^*

$$R_i(\boldsymbol{m}) = Q \int_{t_s}^{t_s + \Delta t} C_i^*(\boldsymbol{x}, t)\mathrm{d}t,$$

where we have used the definition $\boldsymbol{q} = (t_s, \Delta t, Q)$ and $\boldsymbol{x}$ the proposed source location. C_i^* is the adjoint concentration field, obtained by running the adjoint dispersion model from the location and time of the i'th measurement. The source strength should be equal to the inverse of the measurement duration, i.e. Δt_i^{-1}, such that the integrated release is 1. For details on this method, see Keats *et al.* (2006). The advantage of this approach is that the dispersion model only needs to be run once per observation instead of for every proposed source term model. Now, the likelihood can be quantified

$$P(\boldsymbol{d}|\boldsymbol{m}, I) = \left(\prod_i \frac{1}{\sqrt{2\pi}\sigma_i} \right) e^{-\frac{1}{2}\Sigma_i \left(\frac{d_i - R_i}{\sigma_i} \right)^2},$$

where all errors are assumed Gaussian and mutually independent. Following Keats *et al.* (2006), it is further assumed that σ_i^2 can expressed as the sum of the individual contributions
$$\sigma_i^2 = \sigma_{d_i}^2 + \sigma_{R_i}^2,$$

where $\sigma_{d_i}{}^2$ is related to measurement uncertainties, and $\sigma_{R_i}{}^2$ is related to the dispersion model uncertainties. In the following, we assume that the measurement uncertainties are 5% of the observed value but larger than or equal to the detection limit; for ETEX-1 this means that $\sigma_{d_i} = \max(0.01, 0.05d_i)$.

Quantifying model uncertainties

There are two main contributions to the dispersion model uncertainties: errors due to inaccurate physics parameterizations, and errors in the input meteorological fields. Assuming that the meteorological errors are dominant, it should be possible to quantify the model uncertainty using a meteorological ensemble. A first natural guess of an adequate probabilistic model description is simply using the ensemble members to compute a mean and standard deviation of the adjoint concentrations, i.e. C_i^* and $\sigma_{C_i^*}$. By using standard rules of error propagation, we can then obtain a probabilistic forward model with mean and standard deviations $R_i(\boldsymbol{m})$ and $\sigma_{R_i}(\boldsymbol{m})$, respectively. However, following this approach, we encountered two problems, which distorted the resulting posterior probability distribution.

The first issue is that when solving the forward problem for the true source term, $\boldsymbol{m}^{(t)}$, there are several cases, where $R_i(\boldsymbol{m}^{(t)}) = \sigma_{R_i}(\boldsymbol{m}^{(t)}) = 0$, while $d_i > 0$. Hence, these are cases, where the dispersion model fails to predict useful values; however, since the uncertainty is estimated to be zero, their contribution to the likelihood is much larger than the contribution of the predictions that contain useful information. This indicates that the predictions are subject to other significant sources of uncertainty, which are not explained by the meteorological ensemble: either errors in the turbulence parameterization or meteorological errors, which are not captured by the ensemble prediction. As an attempt to solve this problem, a minimum value for $\sigma_{C_i^*}$ is introduced, such that the uncertainty is never zero, even when the predicted adjoint concentration is. Thus, the standard deviation of C_i^* is redefined as $\tilde{\sigma}_{C_i^*} = \max(\sigma_{\min}, \sigma_{C_i^*})$.

The second issue is that the maximum likelihood values differ enormously in magnitude even between neighbouring locations. This seems to be mainly due to the fact that the normalization constant of the likelihood, $\prod_i (\sqrt{2\pi}\sigma_i)^{-1}$, is very sensitive to changes in the uncertainty estimates. It is obviously not appropriate that the most likely location is determined mainly by the normalization constant – i.e. the most likely location will be where the predictions have the smallest uncertainties. To try to compensate for this, the standard deviation of R_i is redefined: $\tilde{\sigma}_{R_i}(\boldsymbol{m}) = \beta \sigma_{R_i}(\boldsymbol{m})$, where the proportionality "constant" β is a function of σ_{R_i} making sure that the quantity $\prod_i \sigma_{R_i}{}^{-1}$ remains constant. To obtain this, β is defined as

$$\log(\beta) = \alpha - \langle \log\left(\sigma_{R_i}(\boldsymbol{m})\right)\rangle, \quad \text{where} \ \ \alpha = \langle \log\left(\sigma_{R_i}^{(t)}\right)\rangle.$$

Here, $\langle \cdot \rangle$ denotes the average, and $\sigma_{R_i}^{(t)}$ is the true (but unknown) standard deviation. Thus, we have introduced the two hyperparamters $\sigma_{\min}$ and α, and one needs to specify both in order to evaluate the likelihood. $\sigma_{\min}$ is related to some unknown contribution of uncertainties, whereas α is related to the "expected posterior distribution width". However, the exact interpretation of these parameters is perhaps more complex, and we therefore need to examine how these affect the posterior distribution. This discussion is continued in the result section.

Proposed method for direct marginal posterior estimation

As described previously, the posterior probability distribution for m can be sampled using an MCMC method. However, we propose a different approach, which is loosely inspired by the Gibbs sampling method (Casella and George, 1992). In the Gibbs algorithm, the posterior distribution is sampled by "fixing" a random set of the model parameters, e.g. x, and generating a number of samples from the *conditional posterior distribution, $P(q|x, d, I)$*. The best of the generated samples is then accepted with a probability proportional to its posterior probability.

In the present application, there are a few advantages of fixing the location x and then sampling the conditional distribution for q. This is mainly because the forward model that relates m to R depends on x. However, when fixing x, the forward model becomes linear (with matrix elements independent of q), which ensures efficient evaluation of the likelihood. The idea is to iterate over selected locations, and for each location sample the conditional distribution for q, which can then be related to the marginal distribution for x (the quantity of interest). In practice, we first select all grid points from a coarse grid in the $x = (lat, lon)$ domain. After the likelihood values for this initial grid are sampled, a finer grid search is conducted only near the grid points with high likelihood. This process is continued iteratively for finer grids until an area of the finest grid structure (the domain grid) is sampled. If the posterior distribution has reasonably well defined maxima, this method is very robust and does not require many iterations. For each proposed location, the conditional distribution $P(q|x, d, I)$ is sampled using the extended Metropolis algorithm (Mosegaard and Tarantola, 1995). The marginal posterior probability for x is then assumed to be proportional to the maximum conditional likelihood

$$P(x|d, I) \propto \max\bigl(P(d|x, q, I)\bigr).$$

This simplified assumption means that two locations with the same maximum likelihood are interpreted as equally likely, although they may have different likelihood distribution widths.

Results for ETEX-1

The described methodology has been applied to the ETEX-1 data set. In Figure 15, the results are shown for a selection of values of $\sigma_{\min}$ and α.
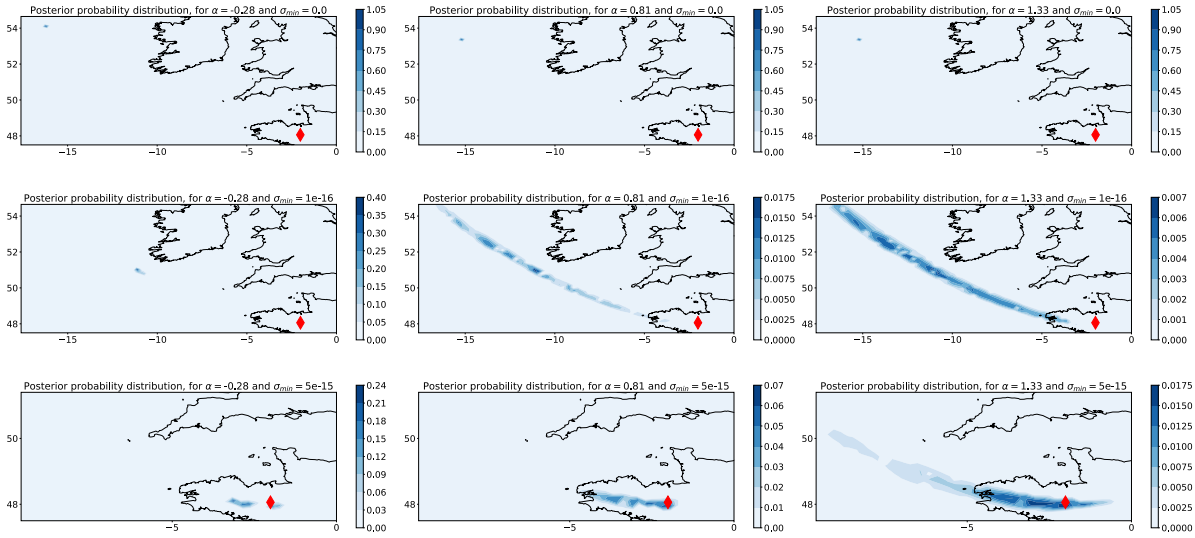
Figure 15 Posterior probability distributions for ETEX-1 case. The red diamond shows the true source location. The figures differ only by the values of $\boldsymbol{\sigma}_{\min}$ and $\boldsymbol{\alpha}$ (shown in the figure titles).

We see that the quantity $\sigma_{\min}$ is particularly important in order to correctly locate the source, whereas α mainly seems to determine the width of the posterior distribution, which is what we would expect. For a "high enough" value of $\sigma_{\min}$, this approach quite accurately predicts the true source location in the ETEX-1 case. However, if the $\sigma_{\min}$ value is too low, the model uncertainty is underestimated enough to significantly change the most likely source location. In particular, setting $\sigma_{\min} = 0$ gives an extremely narrow distribution in the Atlantic Ocean west of Ireland (the upper row in Figure 15), and in this case, changing α does not have a significant impact.

Next, we should ask the question: Does the meteorological ensemble in fact contribute with useful information? For comparison, therefore, we have conducted a similar experiment, but where the standard deviation $\sigma_{C_i^*}$ is set to $\sigma_{C_i^*} = 0.5\, C_i^*$. Hence, the uncertainty is simply assumed to scale with the adjoint concentration values. The result is shown in Figure 16 (right) and compared to the ensemble-based approach in Figure 16 (left). We see that the posterior distribution using the ensemble-based approach does seem to have its peak slightly closer to the correct release location. That said, the two approaches give quite similar results, which indicates that there is no significant benefit from using a meteorological ensemble to quantify the model uncertainty, at least not in the ETEX-1 case.
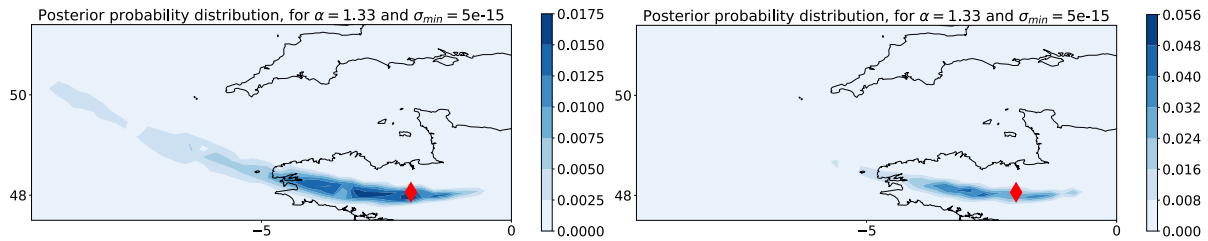
Figure 16 The left figure shows the result using the standard deviation of the ensemble members to estimate the model uncertainty, whereas the right figure shows the result assuming $\sigma_{C_i^*} = 0.5\, C_i^*$.

One clear downside of this approach is that neither of the constants $\sigma_{\min}$ and α are based on theoretical considerations but rather tuned by hand, in order to make the error distribution behave according to the expected Gaussian distribution. This is only possible because we know the true source location, and the method may therefore be difficult to apply to other cases. Thus, we can conclude that the meteorological ensemble did not directly provide the adequate estimate of the adjoint dispersion model uncertainty, we had hoped for. It seems that several additional assumptions are needed to get useful results, and we have even shown that similar results can be obtained without a meteorological ensemble. However, based on the ETEX-1 case, it is difficult to conclude whether this result is also true for other meteorological situations.

Finally, we showed that Bayesian inference can be used to quantify the probability of the different source locations found using the overlap-method. If an adequate uncertainty quantification method is used, Bayesian inference clearly shows that the probability is highest close to the correct source location and then decreases further down-stream.

25

Deterministic results of MATCH

The MATCH model have been run for two setups: Markov Chain Monte Carlo (MCMC) and the approach adopted for the DERMA model described above. The MCMC approach belongs to the family of Bayesian inference methods (Smith and Gelfand, 1992), where the probabilities of source locations are evaluated stepwise in order to find the most likely location (Keats *et al.,* 2006; Keats *et al.* 2008; Yee, 2008; Yee 2012).

The main differences between the two approaches are:

- MCMC is searching through the probability landscape for the most likely source location in time and space.
- The DERMA approach leads to likely source location areas at different times from the ranked overlap of individual observation contributions.
- MCMC may use all available observations.
- The DERMA may be applied to a reduced set of observations to limit the computational load.
- The both approaches could be computational demanding.
- The MCMC may not always converge to the proper source location.
- The DERMA approach is rather robust.

Markov Chain Monte Carlo

The MCMC approach is dependent on forward calculations where neither the location nor the source term is known beforehand. A way to close this is to use an adjoint simulation fed by the observed values as an indication of both the temporal and vertical profiles of the emissions. This simulation is valid over the entire grid so any location could be suggested. The amplitude of the source is then still missing. This could be retrieved by performing a test forward run followed by a bias correction against the observations. This will then scale up or down the source term used. In the end, the square difference between the model and the observations (cost function, J) is derived. Assuming Gaussian probabilities, J is also the negative exponent of a Gaussian posterior probability ($\exp(-J)$) for this location.

The process is to first select a start position for the very first source to evaluate. Here some expert judgement is needed. Having evaluated the probability for this location a random step is taken into the neighbourhood, and the process is repeated. If the new probability increases, the next step is taken from the new location. If the probability decreases, a new location is kept or discarded by the probability given by the ratio of the two probabilities (Metropolis-Hastings approach (Hastings, 1970)). A random number (0–1) will then be evaluated against the ratio probability. If the random number is less than the ratio probability, the new location is accepted for taking a new step, otherwise discarded, and a new try is made from the previous step. This will make up a trace where the underlying probability landscape is step by step revealed. If converging, the algorithm will give a trail that in the end is circulating around the location of most likely location.

Figure 17 shows a (successful) example of the MCMC search pattern. The panel to the left shows the posterior probabilities for visited locations, and to the right the mean search path of possible source locations (weighted mean by means of the probability of each location).
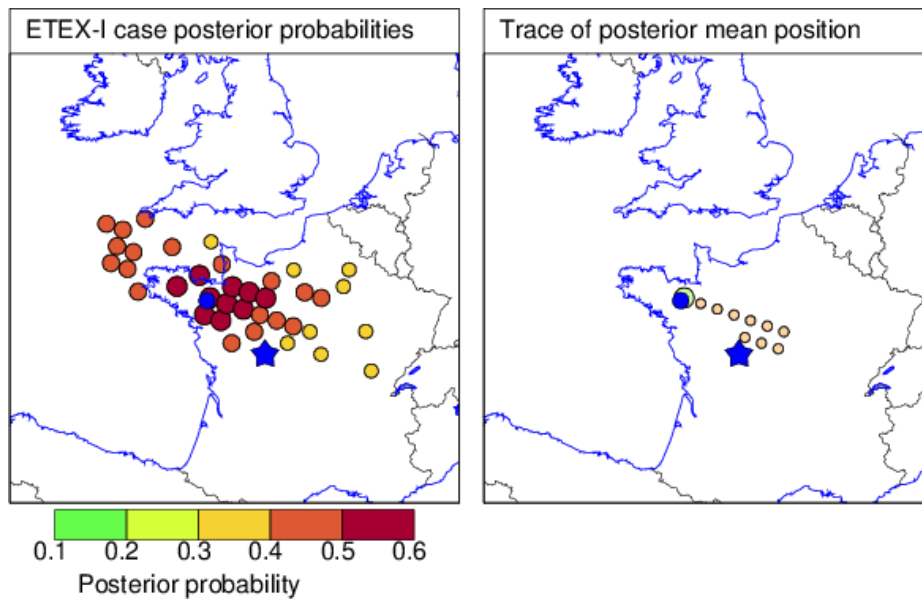
Figure 17 Successful localisation of the ETEX-1 source. The posterior probabilities for visited locations are shown to the left and the mean path to the right (start at the blue star and end green circle). The true release location is marked with a blue bullet.

Figure 18 illustrates when the localisation is not fully successful, and fails in one of the showed cases.
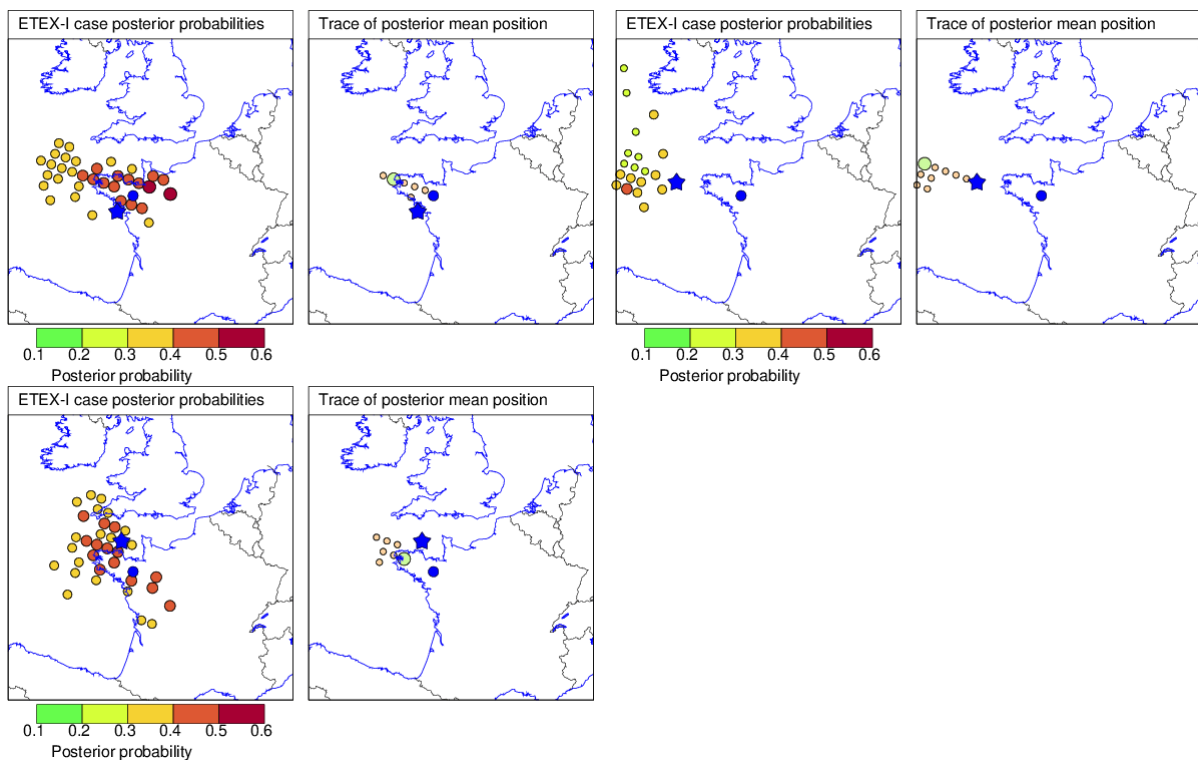
Figure 18 Example of somewhat less successful localisations of the ETEX-1 release site. Posterior probabilities are shown to the left and the mean search path to the right. Start point is denoted by a blue star and the true location by a blue bullet. The upper right illustrates when the algorithm end up confused.

In conclusion the MCMC has some potential but need expert judgement in order to select the initial location for the procedure.

Percentiles of individual adjoint plumes

The DERMA percentile approach described above was also evaluated using the MATCH model. In this case a subset of 50 filter measurements were selected (in the presentation above with DERMA all measurements were used). The 10 measurements with the highest values were first selected, and then additional 40 measurements were randomly selected by weighted bootstrapping (conditional on measured values). Figure 19 shows the selected sites that are well spread over the area.
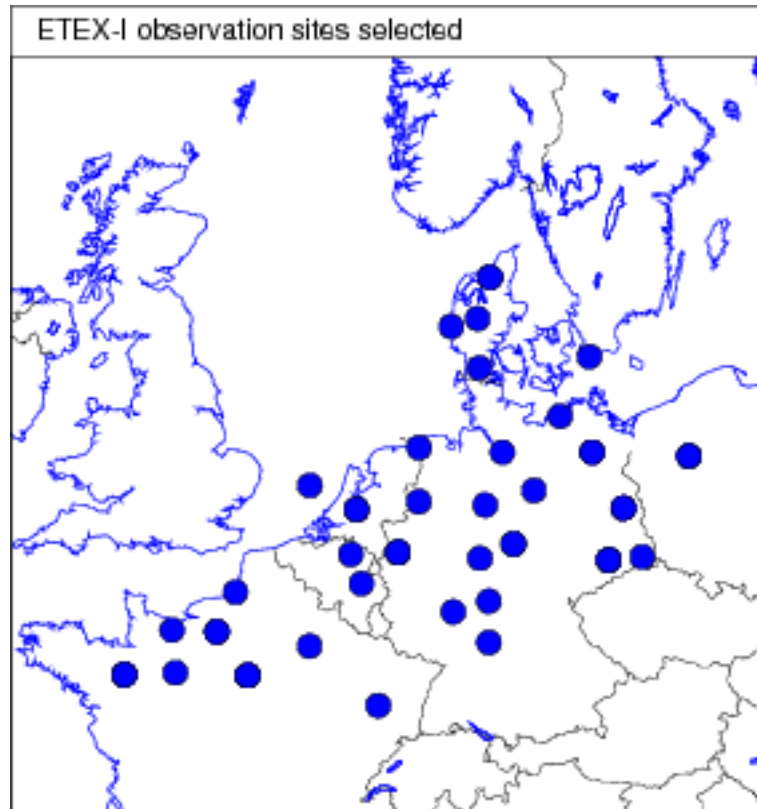

Figure 19 The locations from which 50 measurements where selected for the percentile approach. Some sites were represented with more than one filter measurement.

The individual adjoint runs were made for each measurement by assigning a unit response assumed valid over a depth of 50 m and distributed over the time-interval for the measurement (3 hours). Each such backward plume where then scaled by the measured value in a post-processing step. Figure 20 illustrates the difference between a single adjoint simulation using all ETEX-1 filter measurements versus superimposing a set of individual adjoint plumes. As the source may have a vertical extension, the total column values are used. The essential features are present when using a reduced set of measurements for adjoint calculations. Figure 21 shows the 70th percentile of inverse total columns. The percentiles are normalised to simplify equal colour legend. The major difference to results of the DERMA model (Figure 12) is that the percentiles (and release site potential) become more elongated in MATCH with longer inverse transport.
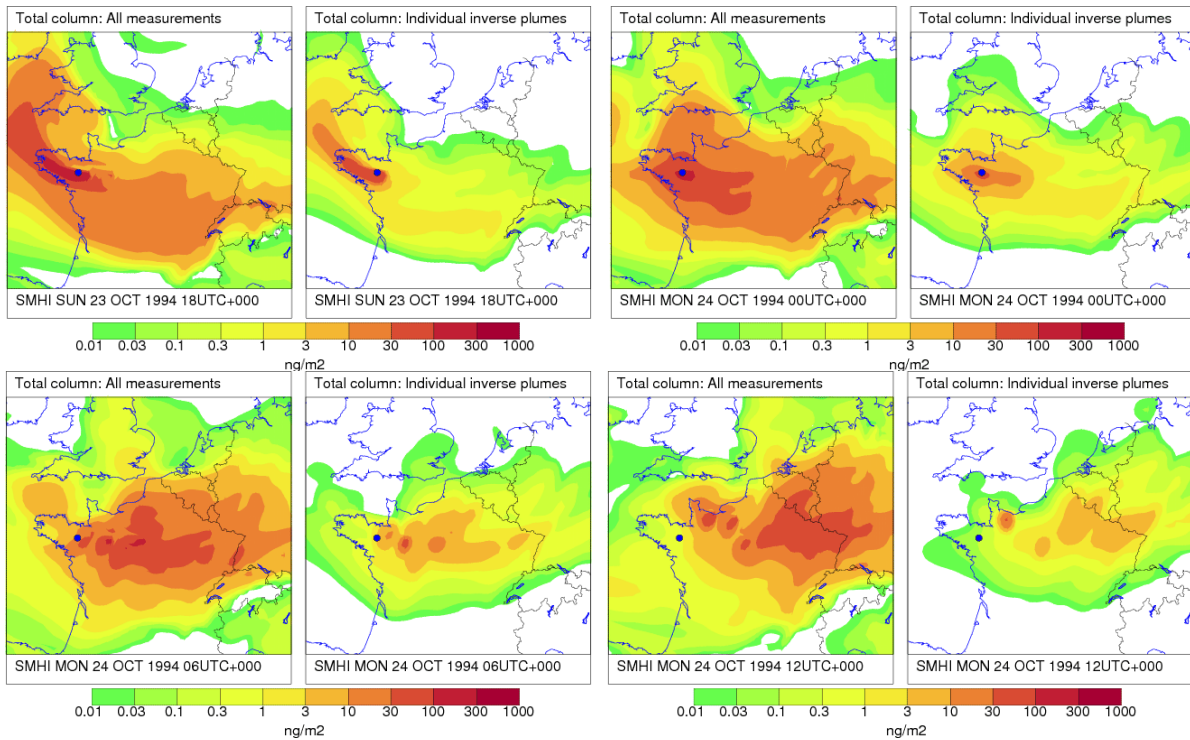
Figure 20 Illustration of the difference between adjoint backward simulations for single run using all measurements (left frame in each panel) and superimposed 50 individual adjoint runs (right frame). The total column values are plotted. The ETEX-1 release site is marked with a dark bullet. The dates goes from 23 Oct 18 UTC, 1994 (top left), 24 Oct 00 UTC (top right), 24 Oct 06 UTC (bottom left) and 24 Oct 12 UTC (bottom right).
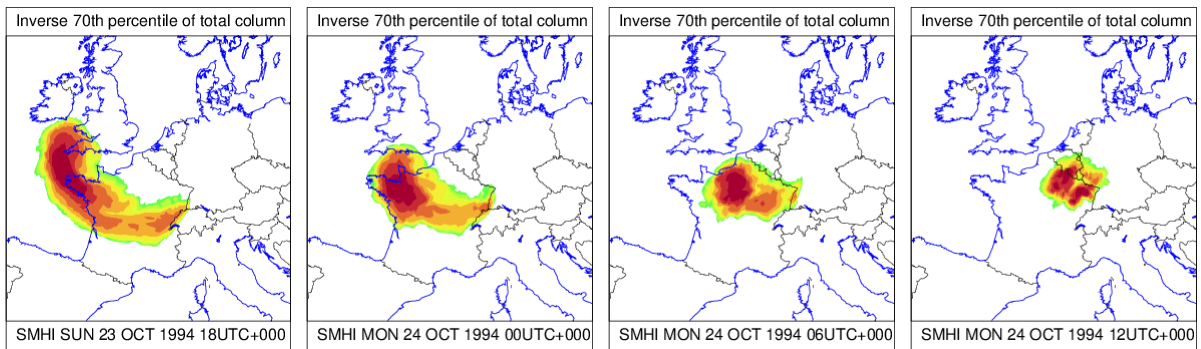
Figure 21 Assignments of possible source areas as given by 70th percentile of total column values from 50 individual inverse plumes. The percentiles are normalised to make the plots share the colour scale. The plots cover the dates 23 Oct 18 UTC to 24 Oct 12 UTC (1994) in steps of 6 hours.

Ensemble-statistical results of MATCH

The MATCH results are for the ensemble weather data confined to inverse plumes of individual observations taken as column integrated inverse plumes. The observation set is the same as above and presented in Figure 19. A development step that was made from the first year of SLIM to enable MATCH handling all observations separately in a single run for each of the used ensemble weather predictions. The calculations have been made on a selected number of weather ensemble members namely members 0, 5, 10, 15 and 20. The selected ensemble members are a bit arbitrary but assumed to be a representative random selection for illustrating the ensemble spread.

We will present the following statistics

- Sum of plumes, 90 percentiles, level of agreement (voting) for a few ensemble members
- Overlay plots including several time-steps for 90 percentile and voting for a few ensemble members
- Overlay plots with mean and median of 90 percentile and voting.

The level of agreement (voting) is made up by counting the number of adjoint plumes that are above a given threshold, normalised by the number of plumes available. The threshold is crucial for this measure and for the ETEX case set to 10^{-9}.

In Figure 22 we illustrate the various outputs with sum of plumes, 90 percentiles and voting for the members 0, 10 and 15 at 00 UTC 24 October, 1994. The figure illustrates that the 90 percentile is very much confined while the voting is broader and as expected the full sum is mostly spread. A general impression from this meteorological dataset is that the transport speed appears to be larger than seen in the MATCH deterministic case above.
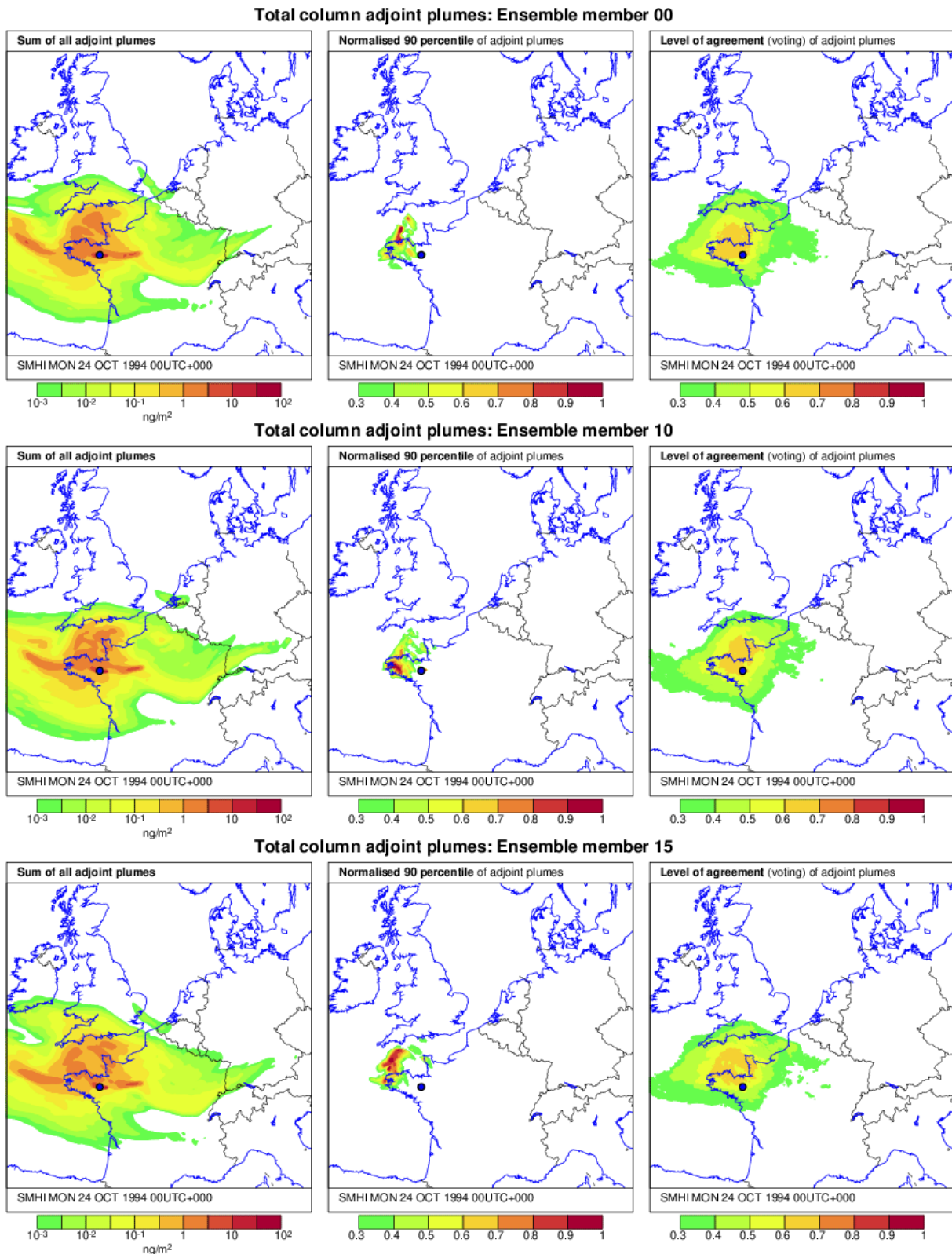
Figure 22 Example of statistics for 00Z 24 October, 1994, for 3 ensemble members: 0 (top), 10 (middle) and 15 (bottom), where the sum of adjoint plumes are shown together with the 90 percentile and level of agreements (voting).

In Figure 23 and Figure 24 are overlay plots where selected timesteps are plotted together for the member 0 and 15, and for 90 percentile and level of agreement, respectively. This is similar to what is shown for DERMA in e.g. Figure 13. Here the time difference is 6 hours in order not to produce too messy image. The colour scheme is alternating in order to separate the time-steps somewhat more. The two alternating colour schemes goes from green to red and blue to red, respectively. The 90 percentiles provide a more restricted adjoint response while the level of agreement aggregates more of the information from the individual adjoint plumes. There are differences in the outcome using the ensemble weather predictions but the main feature remains similar. The setup with consecutive ensemble runs where each member is disconnected from its predecessor with the same member number may contribute to the similarities.
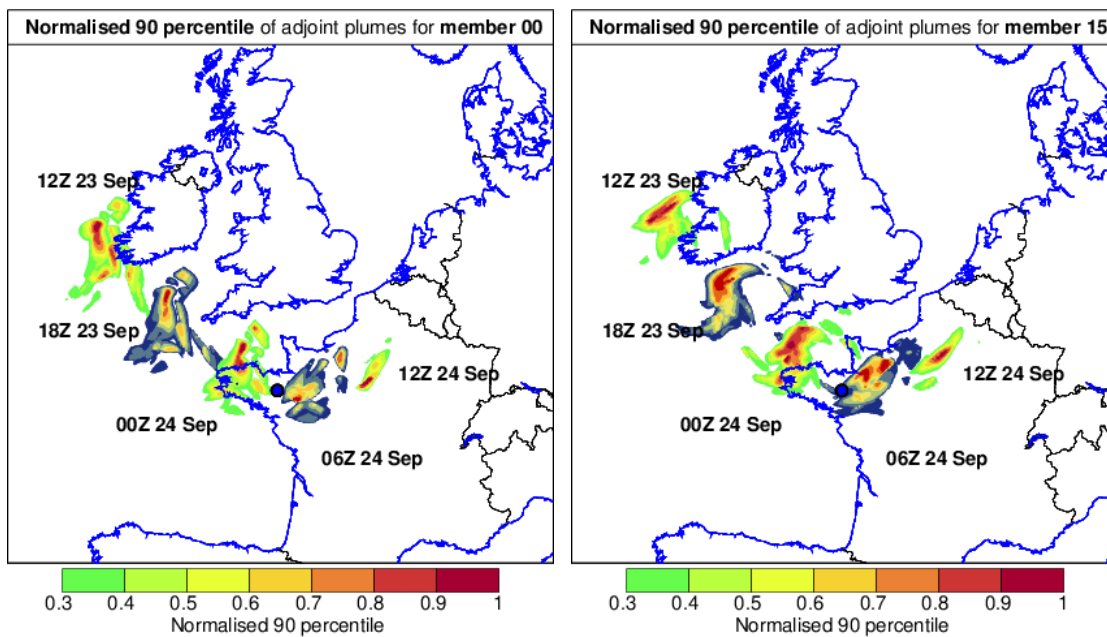
Figure 23 Overlay figure for selected dates for **90 percentiles** for member 0 and 15. Alternating colour schemes are used to separate the time-steps.
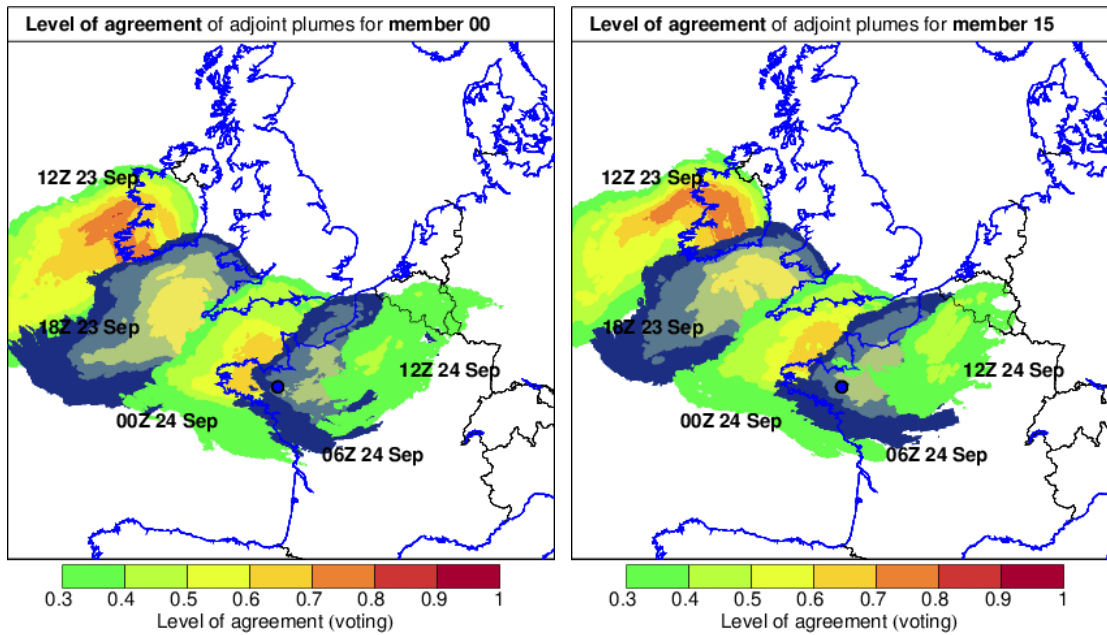
Figure 24 Overlay figure for selected dates for **level of agreement** (voting) for member 0 and 15. Alternating colour schemes are used to separate the time-steps.

In Figure 25 and Figure 26 the ensemble mean and median (of this restricted number of members) are shown for 90 percentile (Figure 25) and level of agreement (Figure 26). These figures may represent the final output comprising the ensemble runs. Apparently the 90 percentile provides a more user-friendly output.
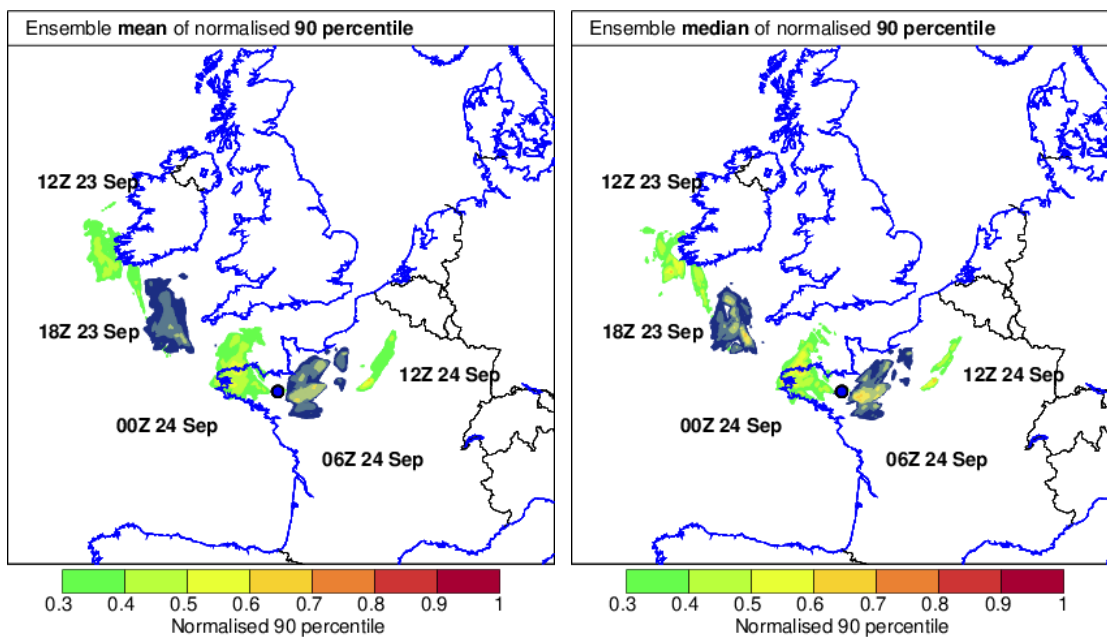
Figure 25 Overlay figure for selected dates for **ensemble mean** and **median** of **90 percentiles**, Alternating colour schemes are used to separate the time-steps.
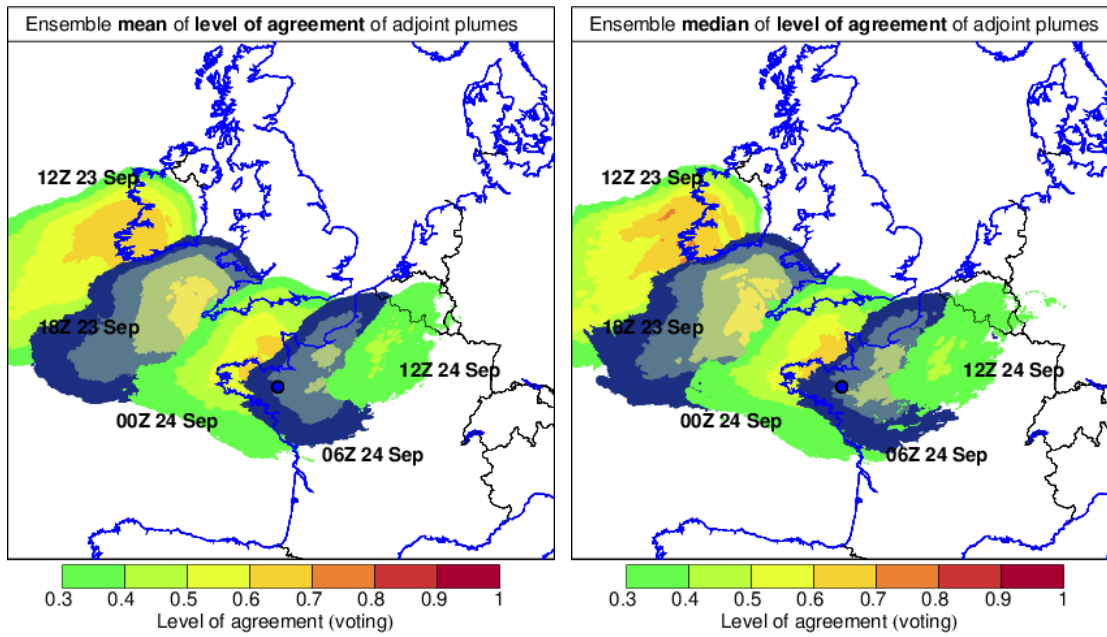
Figure 26 Overlay figure for selected dates for **ensemble mean** and **median** of **level of agreement** (voting). Alternating colour schemes are used to separate the time-steps.

Deterministic results of SNAP

A run of the atmospheric dispersion model results in a field containing the concentrations at a given point in time. We can label the field above a chosen threshold as the Field Of Regard (FOR), using the same terminology as Wotawa *et al.* (2003). Any point in the FOR, when run with the adjoint model, will encapsulate the original point in the adjoint FOR. An example of the FOR for adjoint runs is shown in Figure 27.
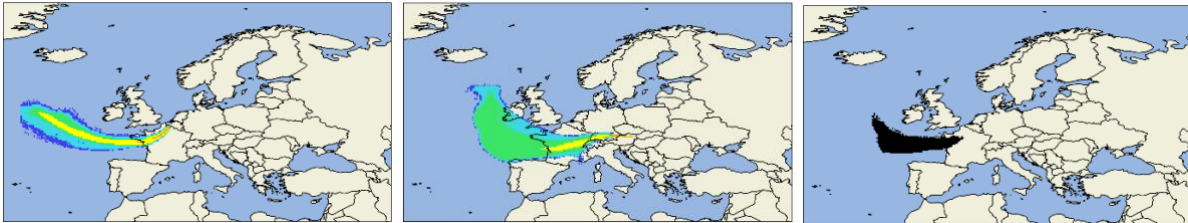
Figure 27 FOR from adjoint plumes from two measurements (acting as sources in the adjoint model) (left and middle), and intersection of FOR (right).

A single receptor will through the adjoint FOR give information on a likely area of release. Masking can be used to combine several FOR from two or more measurements. This approach is illustrated in Figure 27, with two arbitrary adjoint plumes from receptors combined (adjoint concentration exceeding a threshold/not exceeding) into a mask showing locations that are likely to have contained the release. This approach can be further extended by including measurements below the Limit Of Detection (LOD). The adjoint FOR for such a measurement does not contain the release location, or is unlikely to be above the threshold.

This gives a straight-forward method of using all measurements from all stations. Such inclusion of measurements below LOD are shown on the right in Figure 28, which combines the result of Figure 27 with the adjoint plume on the left of Figure 28. These stations and measurements were selected to illustrate this method in the optimal case.

Figure 28 FOR from adjoint plume for a station which had measurement below LOD (left), intersection of Figure 27 and the left figure (right).

This approach is, however, not scalable with more measurements, as the potential area will be a decreasing set which might not converge to the true area. This is especially prominent when errors are present, either due to uncertainties in atmospheric conditions, detection limits, or inaccuracies in the models, including incompleteness of the FOR due to numerical limitations of particles in the Lagrangian model. The following contains a simplified Bayesian approach utilizing a similar methodology, retaining the ease and efficiency of the previous model.

The overlap of adjoint plumes provides information as to where the release would have the highest likelihood. We view areas with adjoint concentrations above a certain threshold as in the field-of-regard. A higher overlap of the different FOR results in a higher probability of a

35

release from the locations in the overlap, whilst areas not covered by the FOR have a lower probability. From a single measurement and the corresponding FOR, one can assign a probability that the threshold is exceeded. As a first approximation, we could assign the probabilities

$$\Pr\left(T_i > T \mid \text{rel}_{\{x,y,\bar{t}\}} \right) = \begin{cases} p_0 & \text{if FOR from } \text{rel}_{\{x,y,\bar{t}\}} \\ p_1 & \text{if not} \end{cases}$$

for threshold exceedance. Here $\text{rel}_{\{x,y,\bar{t}\}}$ is a singular release scenario at (x,y) over the time $\bar{t}$ (corresponding to the sampling time), $T_i > T$ is the hypothesis of threshold exceedance given this release, and $p_0 + p_1 = 1$. p_0 should be higher than p_1 as the FOR provides more evidence, but the ratio between these probabilities does not have to be fixed. Setting $p_0 = p_1$ will not contribute any evidence, and $p_0 = 1, p_1 = 0$ is the intersection from the above section.

For stations with measurements under LOD, an analogous probability can be set by

$$\Pr\left(T_i < T \mid \text{rel}_{\{x,y,\bar{t}\}} \right) = \begin{cases} p_2 & \text{if FOR from } \text{rel}_{\{x,y,\bar{t}\}} \\ p_3 & \text{if not} \end{cases}$$

where the hypothesis is now that the threshold will not be exceeded given such a release. The probabilities $p_2 + p_3 = 1$, with $p_2 > p_3$. The optimal probabilities are not known a priori, but values can be adjusted a posteriori based on heuristics.

To determine how well a release would fit all the measurements (consistency), we start with the following equation, which yields the consistency requirement of the measurements.

$$\Pr\left(\text{measurements consistent with rel.} \mid \text{rel}_{\{x,y,\bar{t}\}} \right)$$
$$= \prod_i \Pr_i\left(T_i > T \mid \text{rel}_{\{x,y,\bar{t}\}} \right) \prod_j \Pr_j\left(T_i < T \mid \text{rel}_{\{x,y,\bar{t}\}} \right)$$

Where T is a threshold set by the detection limit of each station. The index i goes over all measurements above LOD, while the j indexes across all measurements below LOD. This formulation also appears in (Yee, 2017; Senocak *et al.*, 2008), but including different functionals to estimate per station probabilities. Applying Bayes' rule gives the following relation, relating the release location and duration to the consistency of the measurements:

$$\Pr\left(\text{rel}_{\{x,y,\bar{t}\}} \mid \text{consistent} \right) \propto \Pr\left(\text{consistent} \mid \text{rel}_{\{x,y,\bar{t}\}} \right) \Pr\left(\text{rel}_{\{x,y,\bar{t}\}} \right)$$

The prior $\Pr\left(\text{rel}_{\{x,y,\bar{t}\}} \right)$ is set to be uniform, as we have no knowledge regarding location of the source term before adding the signal from the measurements. Information regarding likely sources could here be added by stakeholders, to limit the search space to probable release areas such as radiological facilities.

The probabilities in the hypothesis should be determined by a relation between the adjoint concentration and source parameters. A full model should take into account LOD and sampling times for the stations, dilution volumes, and other expert knowledge, atmospheric dispersion parametrisation, and atmospheric uncertainty. For performance reasons these probabilities have been set to constants. This simplified approach still yields good results for the ETEX-1 case. The weighting between the two hypotheses could be adjusted based on the number of samples per group, to take into account sample size bias.

The implementation takes the following form. An adjoint run with uniform unit release lasting the length of the measurement (or non-measurement) is run as far back in time as deemed necessary. The resulting fields can be iterated over windows of size 1, 2, … n hours, adding the FORs to a merged FOR, to find the dependence on release duration. The probabilities can so be estimated by collapsing the merged FORs through the probability hypotheses given above. To find the most likely locations, the fields containing the highest performing members can be presented. An overlapping time series can also be produced for a given release duration, allowing an estimate of time of release. Estimates for location can also be found by combining the largest probabilities over a certain period of time.

This method only requires building a listing of adjoint runs for each measurement, with later adaptations and adjustments of probabilities being able to run quickly on the produced ensemble of runs. All the steps above can be performed in parallel on supercomputers, allowing rapid estimates of likely source locations. Additional measurements arriving from online radioactivity measurements could be added to the ensembles, allowing renewed probabilities and adjusted location estimate.

Applied to the ETEX-1 case

The hypothesis probabilities are set to $(0.75, 0.25)$ for both hypotheses. Applying the method to the ETEX-1 case using all the measurements results in fields for both a variable start time and a variable duration. Sorting these by highest occurrence of probability gives a way to determine the locations of highest probability. Figure 29 shows the areas in which the 9 highest ranked maps are displayed. These show qualitatively the same areas, and estimates the location somewhat north-east of the actual release location. The initial start time of the release is overestimated, and is from 1-4 hours after the actual start. The duration of the release is both under- and over-estimated, but within 6 hours.
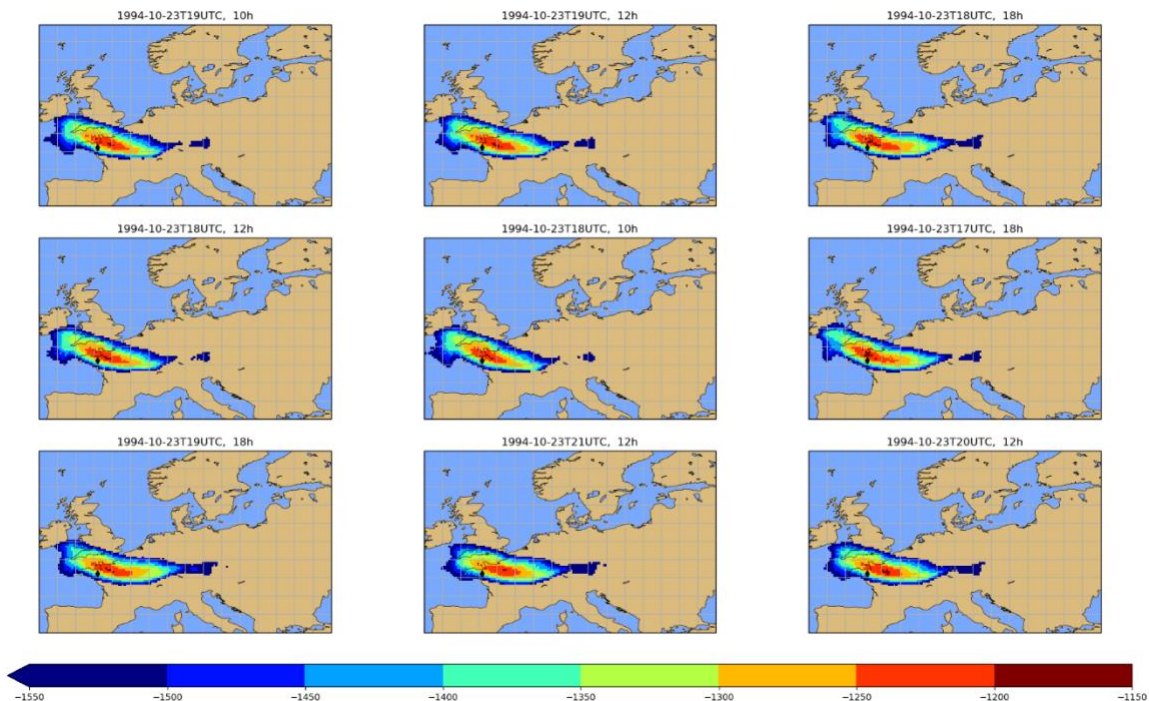

Figure 29 Nine plots showing the highest probabilities for the ETEX-1 case. Black diamond shows the known release location, with the colours showing the logarithmic probability density. The times on the top of each subfigure shows the start time of the estimate, with the duration of the release given in hours. Compare with the actual release at 1994-10-23, 16 UTC and 12 hour duration.

The overlapping time series of probabilities in Figure 30 shows how the probability density changes with time, becoming gradually more dispersed both forwards and backwards in time from the most likely starting time. The difference in maximum probability between the two subplots shows the larger duration as more probable than a shorter duration. This is further supported in Figure 31, which shows the probability density integrated in time, extracting the maximum probability along for each time step.
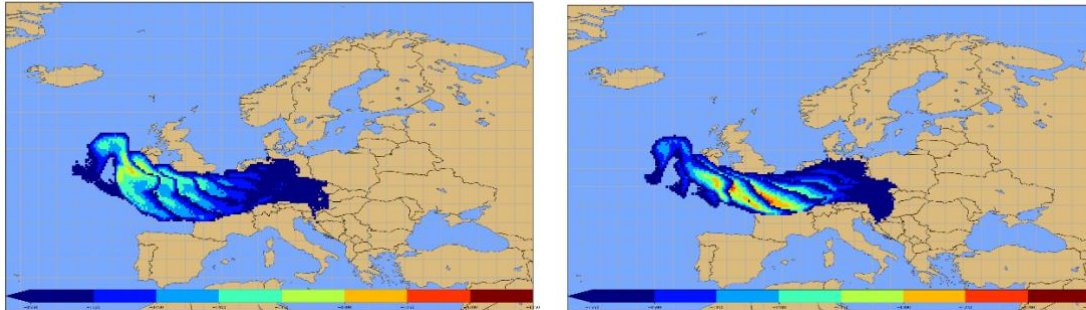
Figure 30 Time series of probability densities assuming a release lasting an hour (left) and ten hours (right). Each slice is separated in time by two hours.

This method seems to be limited by the sampling duration of the stations (three hours) which is mirrored in the start time, duration, and most probable location being roughly three hours from the actual release scenario. The meteorological uncertainties are not taken into account, which could potentially affect the method in meteorological conditions less predictable than ETEX-1.
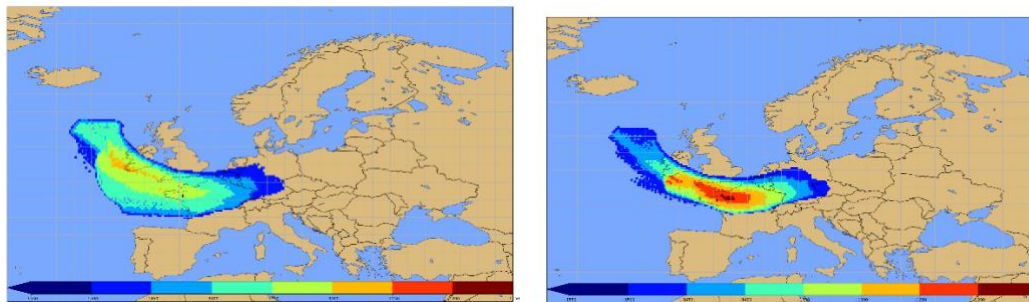
Figure 31 Maximum probability density for a release duration of one hour (left) and 10 hours (right).

Ensemble-statistical results of SNAP

Each of the model prediction members of the meteorological model described in section "Harmonie Ensemble Prediction System runs" were used as input to the dispersion model. The SNAP dispersion model was then run with the 159 stations as input, resulting in 21 estimates of probability of release corresponding to each meteorological ensemble member. These 21 estimates are included in Figure 32. Compared to Figure 29 several ensemble members show the assumed release location to be located between western France and as far upwind of the real location as the Celtic Sea.
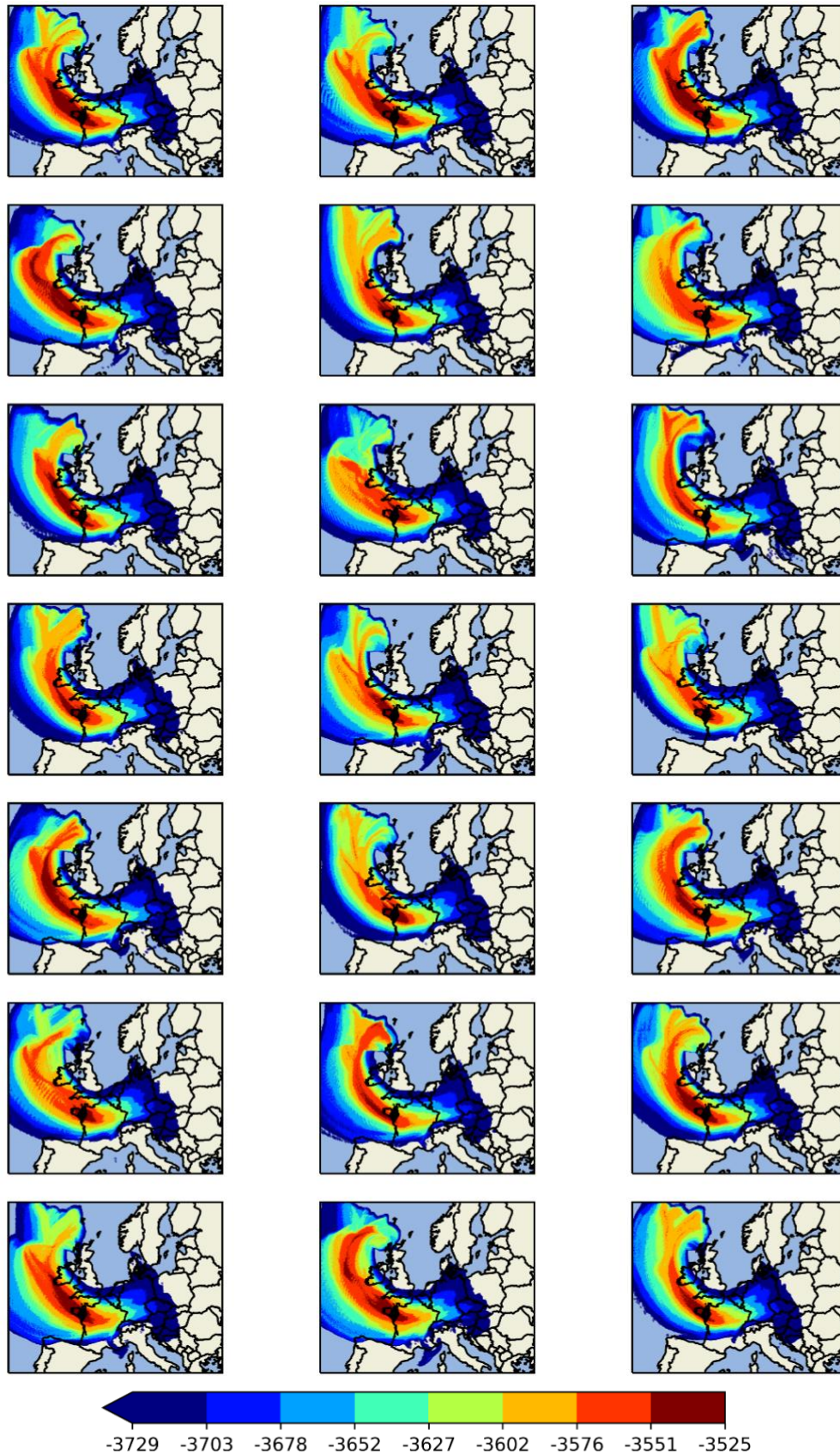
**Figure 32** Probabilities of release from the given locations for each of the 21 meteorological ensembles. The release location of Monterfil is marked with a black diamond. Values are log probability (not normalized). Larger values give a higher probability of a release at this location.

The mean ensemble probability is computed to reduce the amount of redundant information in the dispersion results. This is presented in Figure 33. The combination of ensembles restricts the most likely area of release to exclude parts of the Celtic sea, and limits the location of the most likely source location to an area closer to the actual release location. Examining the probabilities for a set of starting times in the probability distribution results in Figure 34, where the slice consistent with the real release start is more likely than release times both before and after. This also highlights an added benefit to this model approach, parameters can be adjusted and presented in real time without running the more expensive dispersion model.
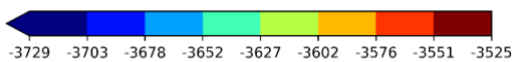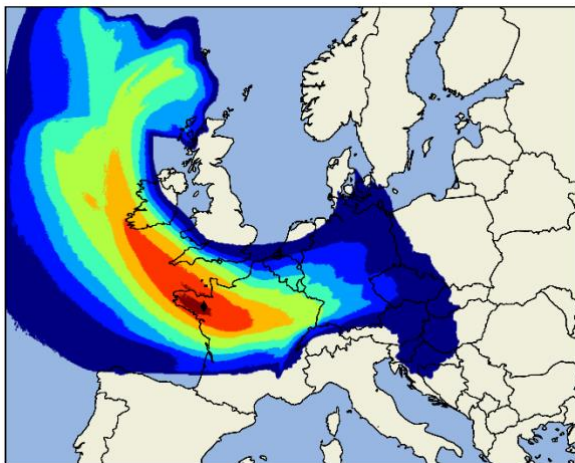
Figure 33 Probabilities for the mean of all 21 members. See Figure 32 for further details.
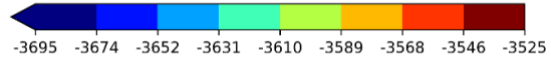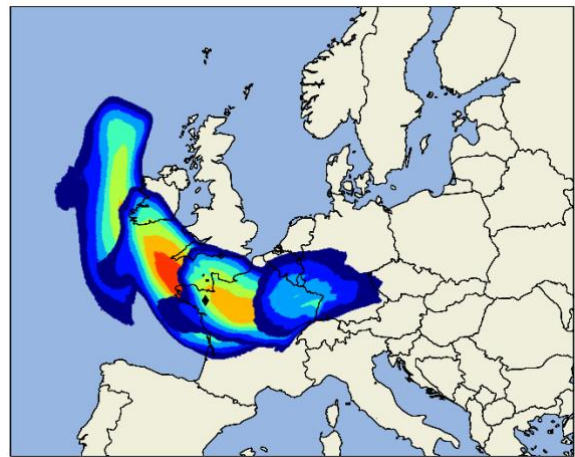
Figure 34 Successive slices show probability densities at 10 hours before the real release (slice furthest west) at the time of the release, 10 and 20 hours after the release. See Figure 32 for further details.
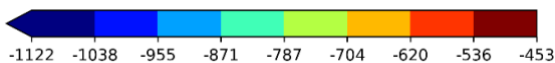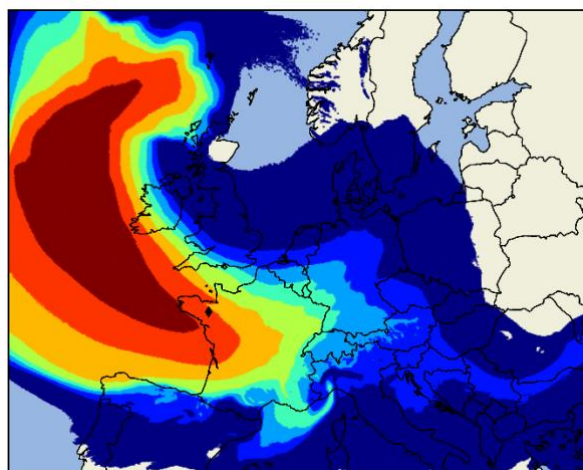
Figure 35 Source localisation only utilising detections to source localisation. See Figure 32 for further details.
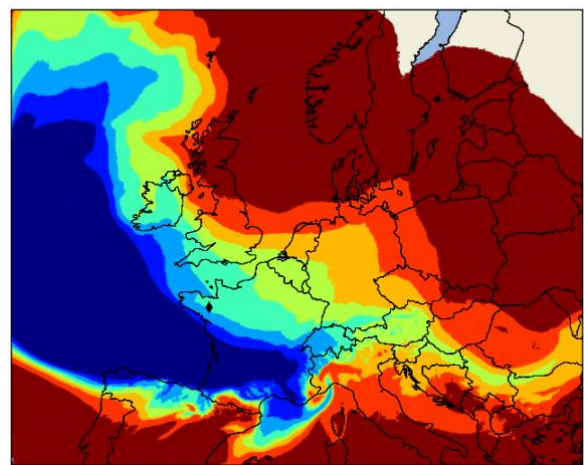
Figure 36 Probability density from only using non-detections for source localisation. Note that higher values are more likely. See Figure 32 for further details.

The added benefit of using non-detections can be illustrated with Figure 35 and Figure 36. The first figure shows the localisation results when only using stations with a detection. Regions affected later in the dispersion runs will be heavily overrepresented as the model fails to take into account growing dispersion volume compared to more complicated models such as (Yee, 2017; Senocak *et. al.,* 2008). Figure 36 shows the probability given by the method when only using stations which had measurements below their detection limit. The localization method uses the product of detection and non-detection, and the probabilities in Figure 36 will act as a penalty where the values are low. The penalty from non-detections is strong in the Bay of Biscay and southern parts of France. Figure 36 shows the penalty given by stations which had measurements below their detection limit. The penalty is strong in the Bay of Biscay and southern parts of France. This penalty forces the probabilities for the combined result in Figure 33 closer to the actual release location.

Results of SILAM

Approaching the ETEX inverse problem with extended 4D-VAR data assimilation

The current subsection outlines the ways of using comparatively classical 4-dimensional variational approaches to emergency inverse problems.

The key issue for the 4D-VAR applications in the inverse problems is that it does not imply any automatically imposed limitations on the source features: the basic formulations allow for the non-point release, time-varying release strength, source changing locations with time, etc. Some extensions to the classical 4D-VAR can be tried but their efficiency can be questionable.

Within SLIM, we examined the behavior of the "ultimate inverse problem": to find out the location and temporal profile of the pollution source without any a-priori constraint.

Theoretical basis of the experiment

In the generic case, the variational method for the inverse problem can be formulated as follows: the maximum likelihood estimate of the parameter $\boldsymbol{\xi}$ (emission intensity in this case) is the value minimizing the cost function

$$J(\xi) = \frac{1}{2}(y - Hx)^T R^{-1}(y - Hx) + \frac{1}{2}(\xi - \xi_b)^T B^{-1}(\xi - \xi_b)$$

Here H is the observation operator and x is the model-predicted concentration. The first term penalizes the deviation from the observations y whose accuracy is described by the covariance matrix R. The prior knowledge of $\boldsymbol{\xi}$ is included in the background value $\boldsymbol{\xi}_b$ (zero would correspond to a completely unknown source) and the background error covariance matrix B. The second term therefore penalizes the deviation from the prior $\boldsymbol{\xi}_b$. With the prior $\boldsymbol{\xi}_b = 0$, this term penalizes the final emission strength, i.e. works as a regularizer of Tikhonov type (Tikhonov, 1995; Press *et al.,* 2007).

Another type of regularization used in the below examples is the penalty for the source geometrical distribution:

$$J(\xi) = C \sum_{i,j} \|\xi(i,j,t)\|^{m/n}$$

where $n > m$ and i, j, t denote the discrete grid coordinates and time. This additional term penalizes the number of grid cells with non-zero emission. The strength of the regularization is controlled by its weight C whereas its sensitivity to absolute emission and steepness of the penalty to a newly appearing emission cell is controlled by the ratio m/n.

The forecast model (SILAM in the specific application) is used for computing the observation vectors for any time. In such case, the gradient of J with respect to ξ is presented as

$$J'(\xi) = M^* H^* R^{-1}(y - \mathrm{H}x) + B^{-1}(\xi - \xi_b),$$

where M^* and H^* are the tangent linear adjoint model and observation operators, respectively (Marchuk, 1995)

The forward dispersion model corresponding to the operator M and defining the time evolution of the model state is defined by the scalar transport equation

$$\frac{\partial c_n}{\partial t} + \frac{\partial}{\partial x_i}(u_i c_n) = \frac{\partial}{\partial x_i} \mu_{ii} \frac{\partial c_n}{\partial x_i} + S_n(x, t) + f_n(x, t),$$

where c_n is a concentration of the *n-th* species, $f_n(x,t)$ is the emission density, and the chemical sources and sinks are included in $S(c,t)$. If the reaction term is linear, i.e. $S(c, t) = \mathrm{k}c_n(x, t)$, then the adjoint of the above equation reads (Marchuk, 1995):

$$\frac{\partial c_n^*}{\partial t} - \frac{\partial}{\partial x_i}(u_i c_n^*) = \frac{\partial}{\partial x_i} \mu_{ij} \frac{\partial c_n^*}{\partial x_j} + \mathrm{k}c_n^*(x, t).$$

Here $c^*(x,t)$ is the first-order sensitivity of the functional J to a concentration perturbation at time t. Its solution corresponds to M^* in the gradient equation.

Basic 4D-VAR solution

The result of the source inversion with basic 4D-VAR without any regularization and any a-priori knowledge is shown in Figure 37. As expected, each station generates "own" source, which is turned on when the station measures non-zero concentrations and is switched off when the site records zeroes. The system then finds the strongest signal at one of the sites and pushes it up. As seen from the Figure 37, this approach stresses a location of one of the stations practically taken at random.
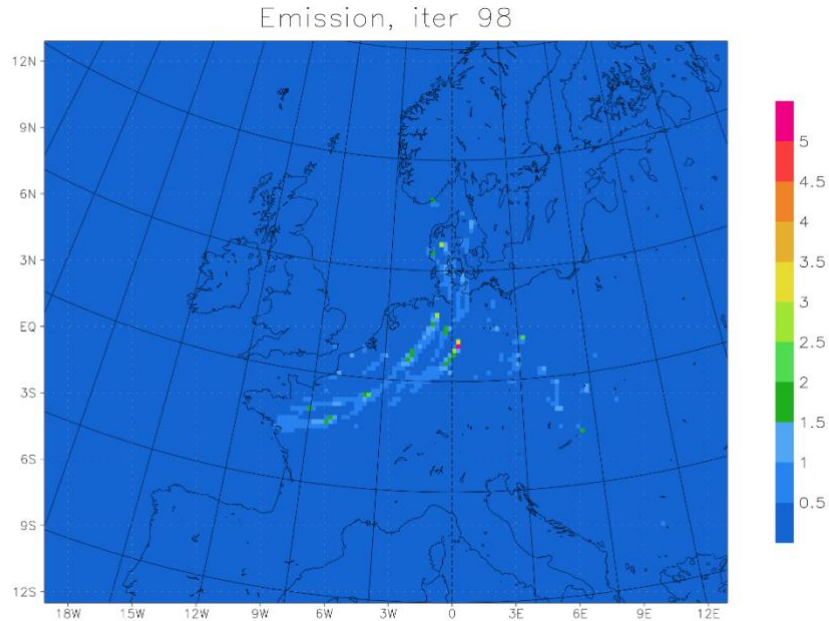
Figure 37 Time-integrated emission retrieved by basic 4D-VAR. Total emission 1065 kg. Meteorology: MEPS member 0.

Tikhonov regularization

The Tikhonov regularization penalizes for the overall strength of the solution: absolute emitted amount. The resulting solution (Figure 38) is more homogeneous because the individual strong points are suppressed, thus creating a multitude of emission locations, still attached to the individual stations. However, this kind of regularization shows also the actual place of emission.
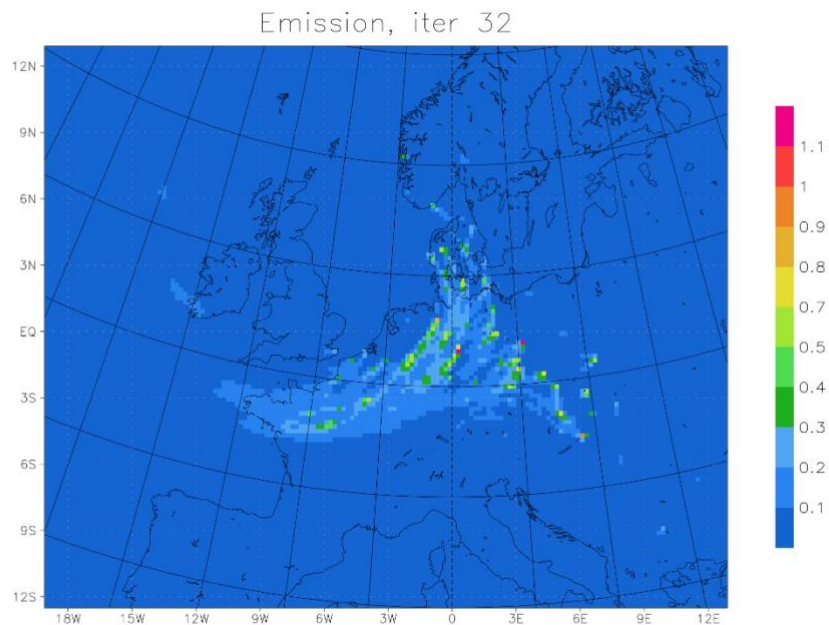
Figure 38 Time-integrated emission retrieved with regularized 4D-VAR with Tikhonov-type regularization. Total emission 475 kg. Meteorology: MEPS ensemble member 0.

Combined regularization: strength and size of emission field

The last set of configurations tried within the experiment used both types of regularization: Tikhonov-type and size-penalizing ones. The outcome however is still not quite satisfactory: the region of actual source location is quite well visible but the collection of "own" sources at the sites reporting the highest concentrations is still present in the solution. However, their contribution is further reduced.

Discussion

The behavior of variational assimilation reported in the current exercise has been noticed long ago. In fact, the conclusion on limited applicability of 4D-VAR to completely unconstrained inverse problems has been made by Sofiev and Atlaskin (2004). In that study, we have suggested a yet-another modification of the 4D-VAR approach, which has led to a better result, finally allowing the identification of the source location (Figure 39). However, the methodology included several poorly justified technical steps (low-pass filtering, background elimination, additional term to the main cost function), which have thin theoretical ground and require more rigorous considerations before recommending them to general use.
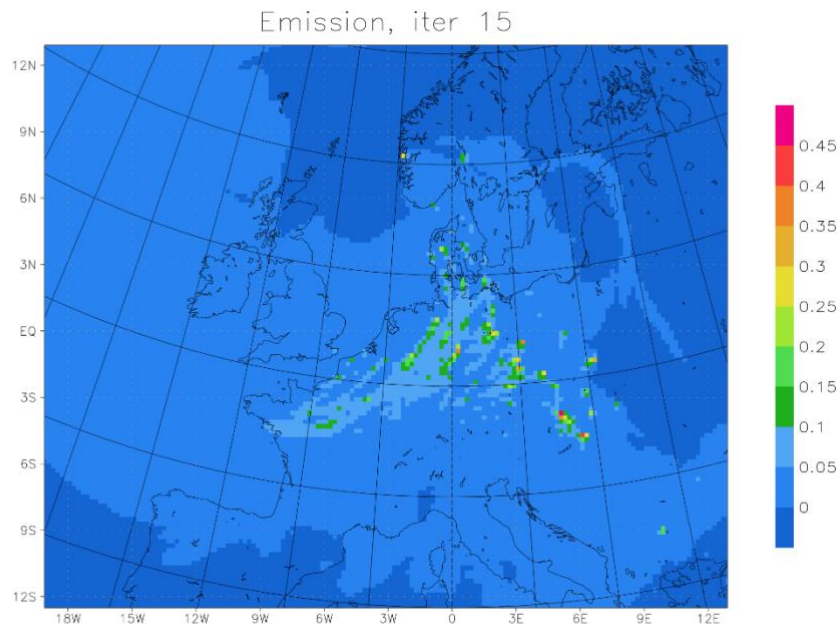
Figure 39 Time-integrated emission retrieved with Tikhonov- and size-regularizing modifications of the cost function. Total emission is 171 kg. Meteorology: MEPS ensemble member 0.
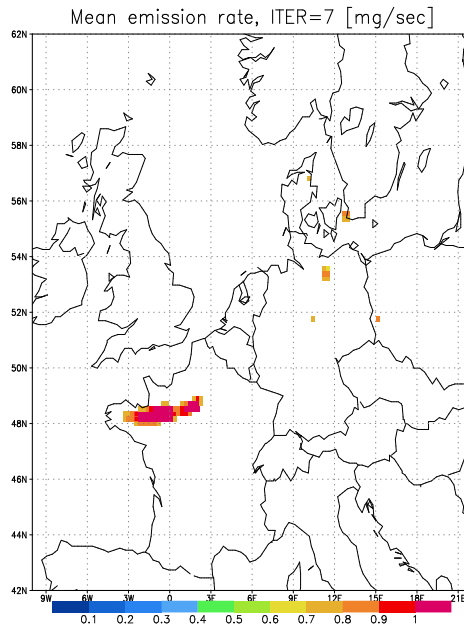
Figure 40 Solution obtained using modified 4D-VAR approach. Model: SILAM v.3, meteorology: HIRLAM v.5.

The above examples showed that variational data assimilation as a tool for inverse problems solution requires additional theoretical considerations before recommending it to a wide usage in real-life problems where the actual source location is not known. The method clearly has strong potential upon a proper combination of regularization and post-processing is found and justified.

Brute-force source inversion of ETEX-1 with SILAM

Source inversion with off-line transport models relies heavily on the meteorological driver. Inconsistencies between the actual meteorology and the modeled one lead to poor convergence of inversion. When a source-inversion method does not lead to unequivocal results it is often difficult to tell between the poor performance due to insufficiently accurate meteorological information, due to the lack of observations, or due to deficiencies of the method itself. To address the issue we used a brute-force approach to get the best possible estimate of the emission source for a given meteorological driver.

Experiment setup

The ETEX-1 experiment yielded about 4000 samples, out of which about 2500 were non-detections and about 250 detections with certain concentrations. For every observation and every ensemble member a footprint calculation was performed. The footprints were calculated at 0.1×0.1-degree grid (323×258 cells) aligned with the meteorological grid, i.e. at the half-resolution of the original meteorology. Such a setup allowed for using wind components at dispersion-cell interfaces and other quantities at the cell centers without any additional interpolation. The footprints were calculated starting from the end of the last observations (1994-10-27 09Z) for 120 hours backwards in time.

For the inversion we assumed that the source was located within the lowest model layer (25 m from the surface), therefore only the lowest-layer hourly-averaged "concentrations" of the footprints were stored. With such a lookup table we could evaluate the results of a forward simulation for any spatio-temporal distribution of near-surface emission sources without a need to perform additional model simulations.

The evaluation of the results was made with the following cost function

$$J = \sum_i \frac{(M_i - O_i)^2}{\sigma_i^2},$$

where M and O are modeled and observed concentrations, σ_i^2 is a variance of the observational error, and summation is taken over the whole set of valid observations. The observational error consists of many components, some of which are quite poorly quantifiable. We assumed the error consisting of a sum of a constant and fractional error. The constant and a fraction of the observed value were assumed identical among the observations. The emission source that minimizes the cost function is considered as the most consistent with the observations. Note that the location of the minimum of the cost function does not depend on the magnitudes of these errors, but only on their ratio. Modifying this ratio we could put more or less emphasis to detections vs non-detections.

The ETEX-1 dataset does not provide observational errors; therefore we used three expressions for the error. All errors were a sum of a constant absolute error of 0.01 ng/m³ (a discrete of the etex1_v1.1.960505 data files), and a relative error of 30%, 1% and 0.1% of the observed value. These errors are hereafter referred to as v0, v1, and v2, respectively. To simplify the comparisons of these cases the costs were normalized by the cost of zero emission:

$$J_0 = \sum_i \frac{O_i^2}{\sigma_i^2}$$

To identify the optimal source locations and emitted amount we calculated footprints for each of 21 ensemble members and a set of source durations of 1, 3, 6, 9, 12, 15 … 36 hours (273 time-resolving footprints for each measurement). Then within each footprint for every point of the map and every hour of the emission start the optimal emitted amount was calculated as the one minimizing the cost function, and the resulting time-resolving maps of emitted amount as a function of a point-source location and corresponding costs were stored.

Results

The minimum of the cost map over space and time gives the location and time of the tracer injection most consistent with given meteorology and given release duration. Corresponding value form the emitted amount maps gives the emitted amount that best fit the measurements in terms of a given cost function.

The set of scores v0 with the large relative component in measurement error gave a small reduction of scores, with quite small optimal emitted amount (Figure 41). The reason is that the large relative error puts a strong emphasis to the observations that reported zeros. Therefore the minimal cost is achieved for the release that is consistent with some of the non-zero observations, but does not reach the stations that observed zeros.

The spread of the optimal costs among the ensemble members is significant. Mbr015 while allowing for a decent cost reduction indicates no preferred release duration within 1–27 hours. Mbr008 does not allow for more than 5% cost reduction, except for a very short release. In average, all members tend to prefer shorter releases, and the strongest cost reduction corresponds to the largest release.

The maps of costs and emitted amount corresponding to the two least-scores points from Figure 41 are shown in Figure 42. In both cases the minimum of the cost-function is quite shallow (a bit less than 12% of total cost removed), but well localized. Emission maps show somewhat elevated values around the location of the minimal cost. Very high emission values are shown in areas that weakly affect a couple of remote stations with non-zero detections, but do not affect the rest of the stations. These high values, however, correspond to a negligible reduction of scores. The locations and timing of the optimal scores substantially differ among the simulations for the v0 cost function.
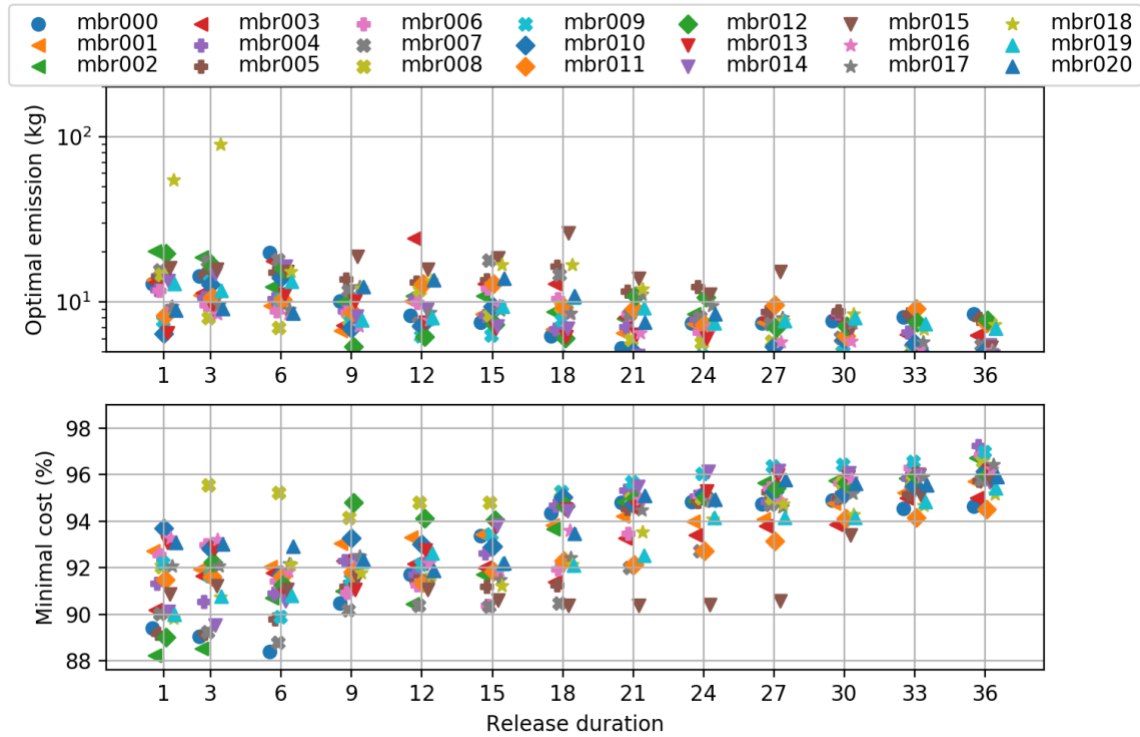
Figure 41 Optimal emission and minimal costs for 21 ensemble members as functions of the release duration for v0 error set. Some spread added along the x-axis to reduce the overlap of the markers.
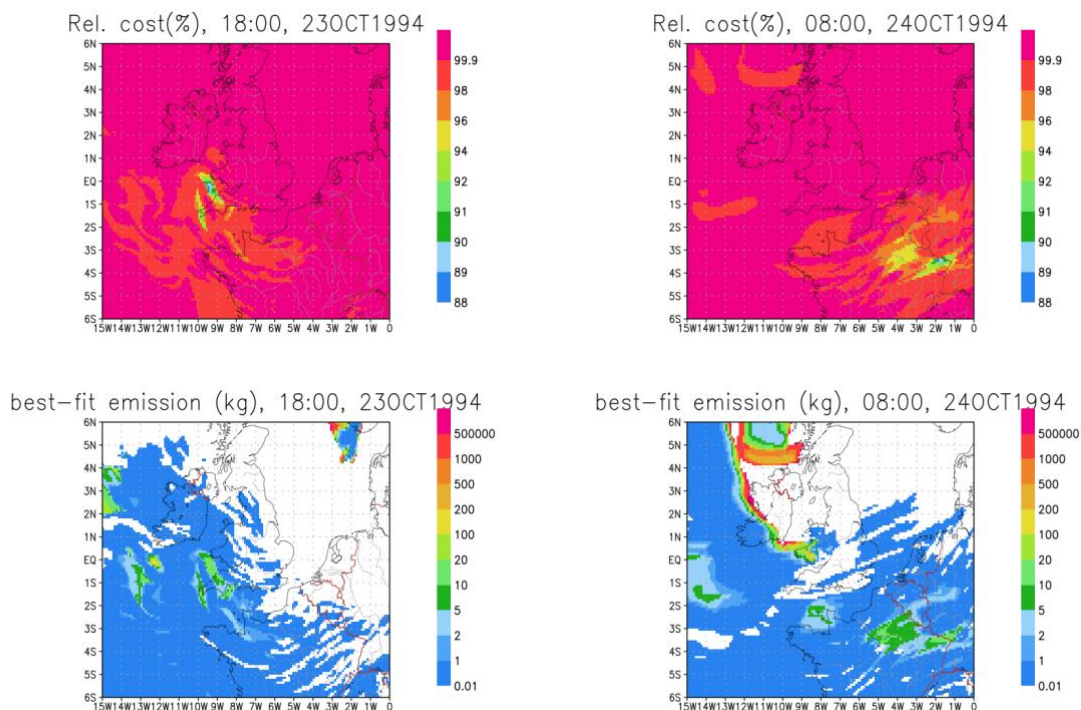
Figure 42 The maps of the minimum cost and corresponding emitted amount corresponding to two least-cost footprints given in Fig. 41: 1-hour long release started at 18Z 23.10 and transported with mbr002 meteo (left), and 6-hour long release started at 08Z 24.10 transported with mbr000.

In the v1 scoring we have reduced the relative component of the observation error to 1% of the value to put more emphasis on non-zero observations, so optimization gets more tolerant to the false-hits. Such a formulation of errors allowed for more significant reduction of the cost (Fig. 43), where more than a quarter of the cost could be removed, and corresponding releases got notably higher.

The ranking of the ensemble members is very similar to the v0 case: mbr008 again leads to the highest cost and lowest emissions, mbr015 has almost uniform minimal cost up to 27-hour release. Similar to the previous case the longer releases allow for less cost reduction than shorter ones.

The minimal costs panel in Figure 43 indicates clear leaders in cost reduction: mbr003 and mbr007. Unlike in v0 case, the optimal release is 9-hours long, and the best scores have a clear gap from others. The locations and timings of these releases (Figure 44) are quite close to each other and are within few hours and couple of hundreds of kilometers from the actual ones.
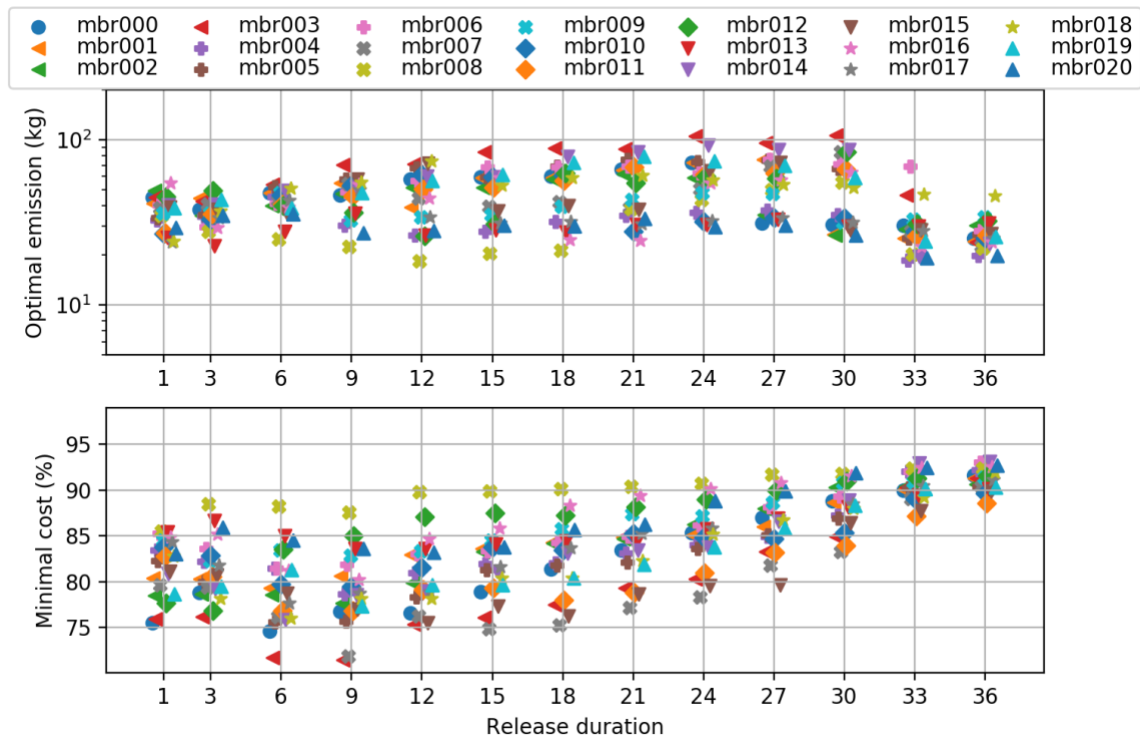
Figure 43 Optimal emission and minimal costs for 21 ensemble members as functions of the release duration for v1 error set. Some spread added along the x-axis to reduce the overlap of the markers.
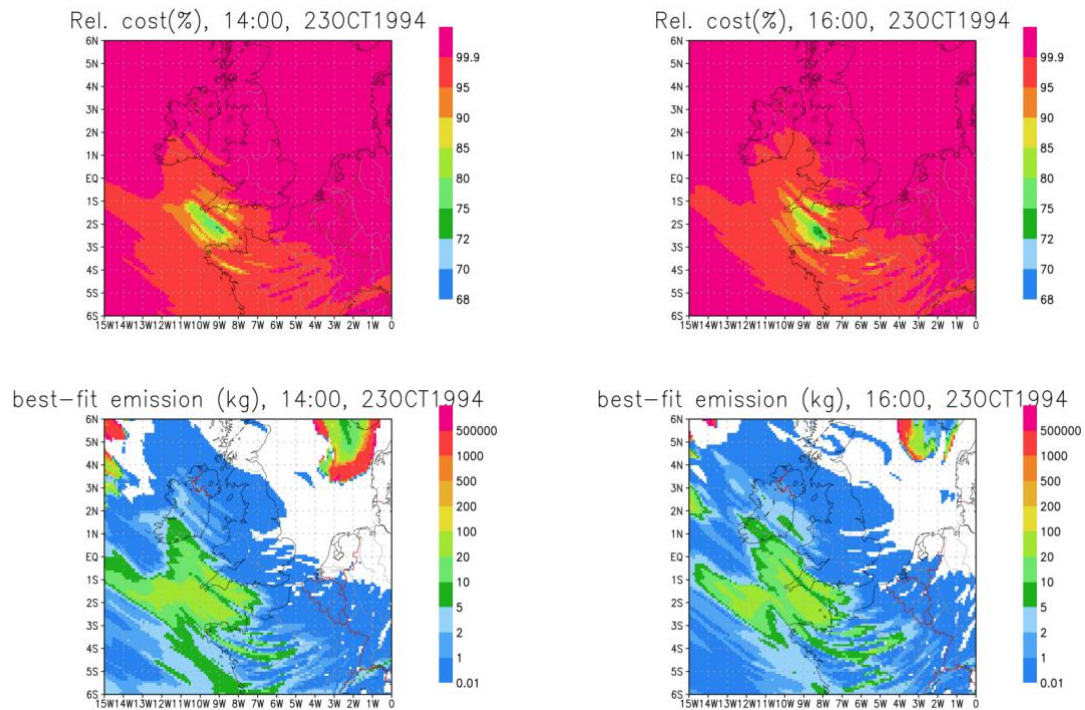
Figure 44 The maps of the minimum cost and corresponding emitted amount corresponding to two least-cost footprints given in Figure 43: 9-hour long release started at 14Z 23.10 and transported with mbr003 meteo (left), and 9-hour long release started at 16Z 23.10 transported with mbr007.

Further reduction of the relative-error component v2 leads to further reduction of the optimal scores (Figure 45). The best-performing ensemble members are the same as in the previous case. The gap in scores between the best-fit release duration (9 hours) and the true one (12 hours) has reduced. The near-optimal cases (mbr003 with 6- and 9-hour release in Figure 46, and mbr007 9-hour Figure 47, left) indicate very similar optimal source location ~100–200 km north from the true one and about a couple of hours difference in the release timing from the true one.

The best-performing member with the right release duration , and mbr015 12-hour has a local minimum of the cost around the right location, but has the absolute minimum of the cost at the different location and the time (Figure 47, right).
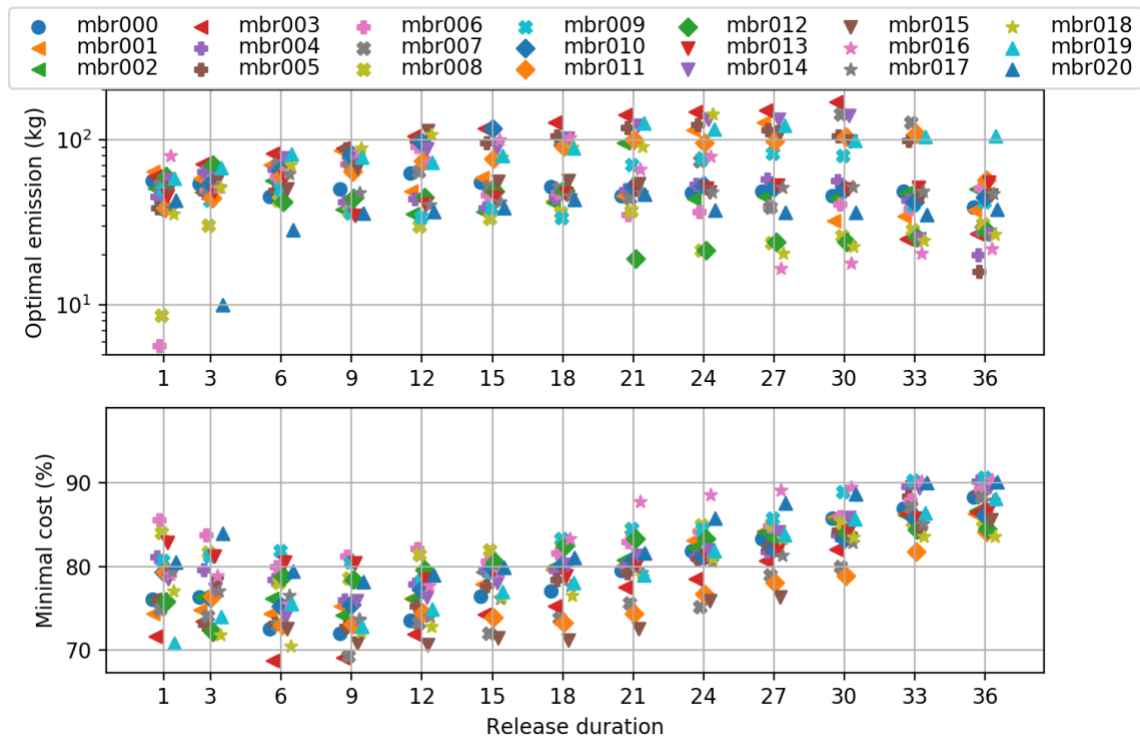
Figure 45. Optimal emission and minimal costs for 21 ensemble members as functions of the release duration for v2 error set. Some spread added along the x-axis to reduce the overlap of the markers.
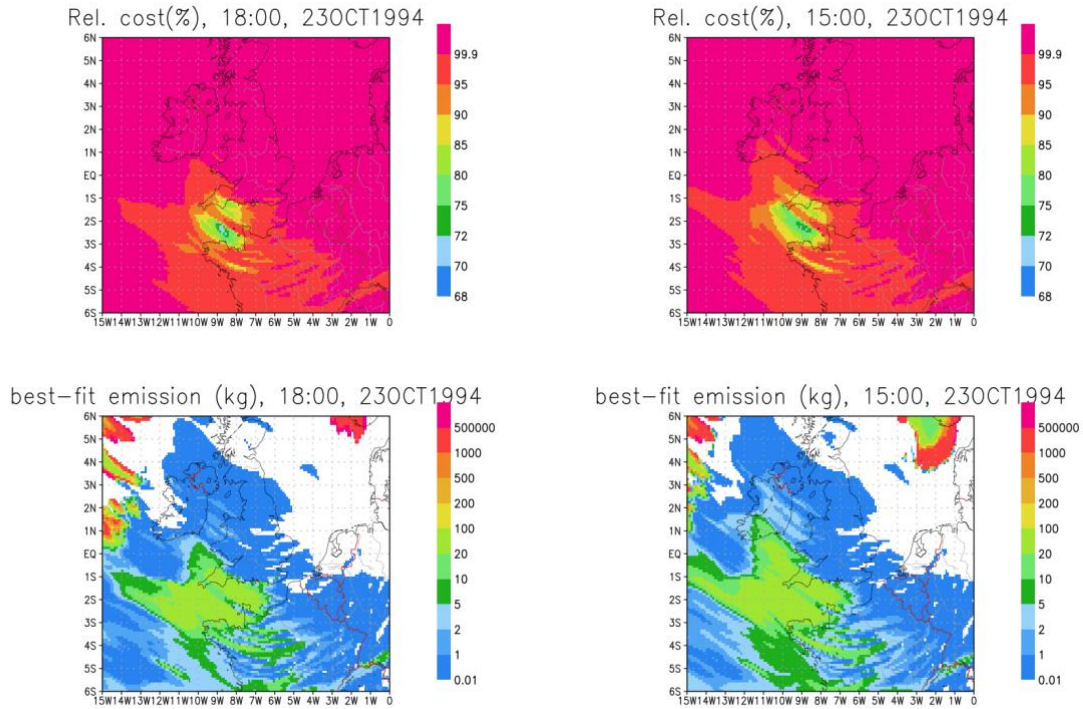
Figure 46 The maps of the minimum cost and corresponding emitted amount corresponding to two of least-cost footprints from mbr003 given in Fig. 45: 6-hour long release started at 18Z 23.10 (left) and 9-hour-long release started at 15Z 23.10(right).
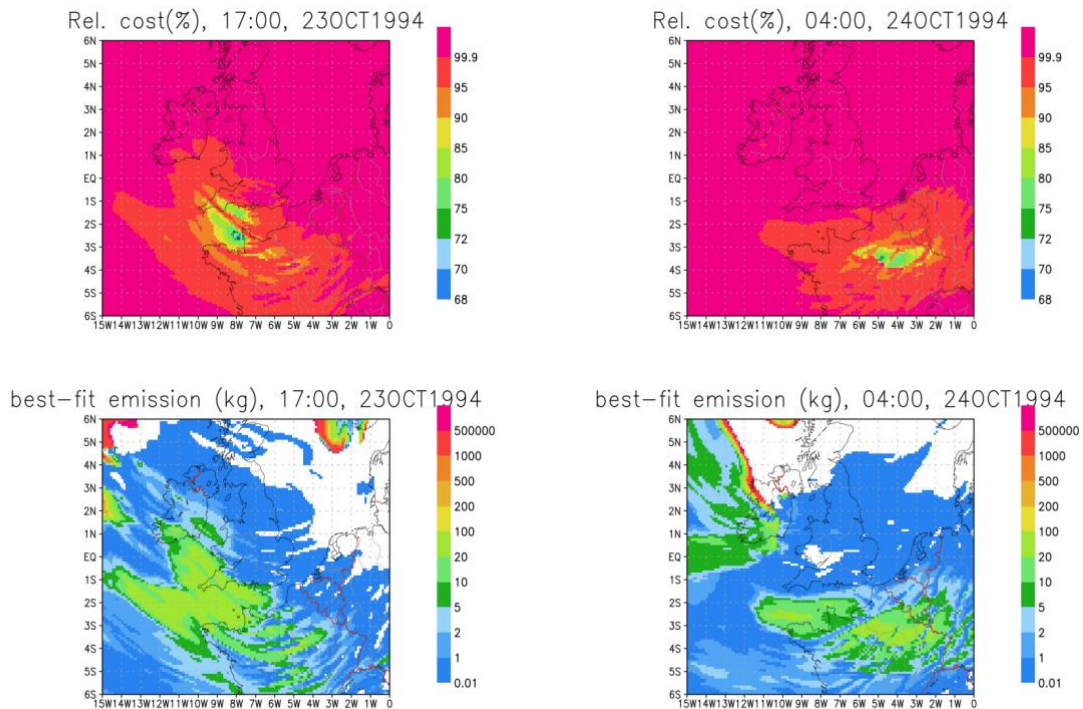
Figure 47 The maps of the minimum cost and corresponding emitted amount corresponding to two of least-cost footprints given in Fig. 45: 9-hour long release started at 14Z 23.10 and transported with mbr07 meteo (left), and 12-hour long release started at 04Z 24.10 transported with mbr015.

Conclusions

To perform an exhaustive check of possible source location and start-end times we evaluated the whole range of the options against the available ETEX-1 data set. The evaluation was possible with the adjoint modeling, where pre-calculated footprints were used to get the model data at the stations for each emission scenario.

With the exercise we could identify the source configuration (location and starting time) that is most consistent with the observed data for each of the meteorological ensemble members and a source duration. The least-cost estimates of the source time were within a couple of hours from the true one, and the location is about 100 km north from the true one.

We have limited the number of the meteorological data sets to 21 keeping the number of a member of the meteorological ensemble the same for every simulation. The members indicated different levels of consistency with the observed data. A combination of different members form different forecasts would probably allow for finding a configuration that gives even better results.

For the considered meteorological dataset the most consistent meteorological datasets have the closest to the reality emission source. It is not clear how to select the optimal number of meteorological ensemble members to ensure the reliability of the source inversion.

Some ensemble members provide more consistent inversion than others. Therefore they cannot be treated as equally probable scenarios, but rather more or less accurate representation of the real meteorological conditions. It would be interesting to identify meteorological scores that could select the best meteorological dataset for the inversion procedure. Then the computational cost of the inversion even with the brute-force approach would become affordable.

The Autumn 2017 Case of Ru-106

During the period 3–6 October 2017, the Incident and Emergency Centre of the International Atomic Energy Agency (IAEA) was informed by Member States that low concentrations of Ru-106 were measured in high-volume air samples in Europe. The detected isotopes did not contain any other radionuclides (e.g. other fission products such as Cs-137) and were at levels far below those requiring public protective actions, however not accounting for the anticipated higher concentrations at the release site. Corresponding data and information were obtained from the IAEA (2017a, 2017b). The data comprise 387 measurements of Ru-106, some of which correspond to levels below minimum detectable activities. The data are time-average concentrations corresponding to varying time periods of up to seven days, cf. Figure 48 below.

From a meteorological point of view, seven days can be a long time with potentially a number of meteorological phenomena such as front passages taking placing at the release site within the period. Possible sampling scenarios include evenly distributed low concentrations at the station site throughout the sampling period, or brief high concentrations corresponding to a narrow plume passing over the site in a short while. Therefore, such measurement data should possibly be discarded in a localization study. The discarded data can, however, be used for verification purposes.
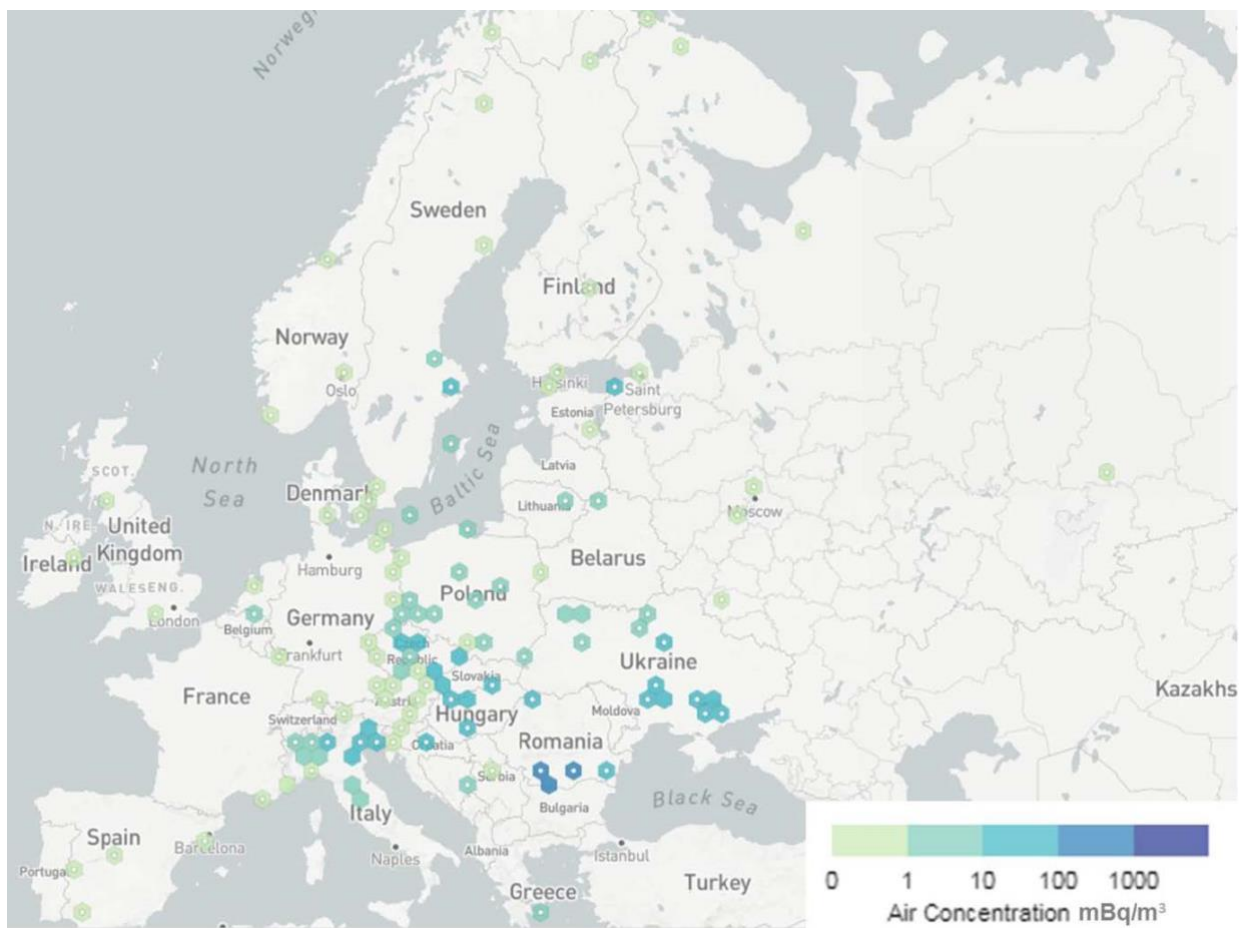

Figure 48 Locations where concentrations of Ru-106 in the air have been reported to the IAEA (IAEA, 2017a; 2017b). The measurements were taken during different sampling periods ranging from daily to weekly.

## Harmonie Ensemble Prediction System runs for the Ru-106 case

The HARMONIE-ALARO configuration used for the Ru-106 case is the same as that for the ETEX-1 case, except for the different, larger domain that covers Europe and a good part of Russia. The ensemble prediction runs cover the period 25 September – 5 October 2017 with two runs per day, each consisting of 1 control + 20 perturbed members.

The ensemble prediction runs show that the weather over most of Russia at the time of the estimated Ru-106 release was dominated by a high pressure system centred over north-west Russia that persisted for several days leading to relatively calm and dry conditions in the western part of Russia. Mean sea level pressure, including ensemble uncertainty, is shown in Figure 49 which is valid at 0 UTC 27 September 2017, i.e. near the subsequently estimated time of release. Figure 50 shows wind from a north-easterly direction near the two potential release points in Russia, and Figure 51 shows a precipitation "postage stamp" for the time around the estimated release.
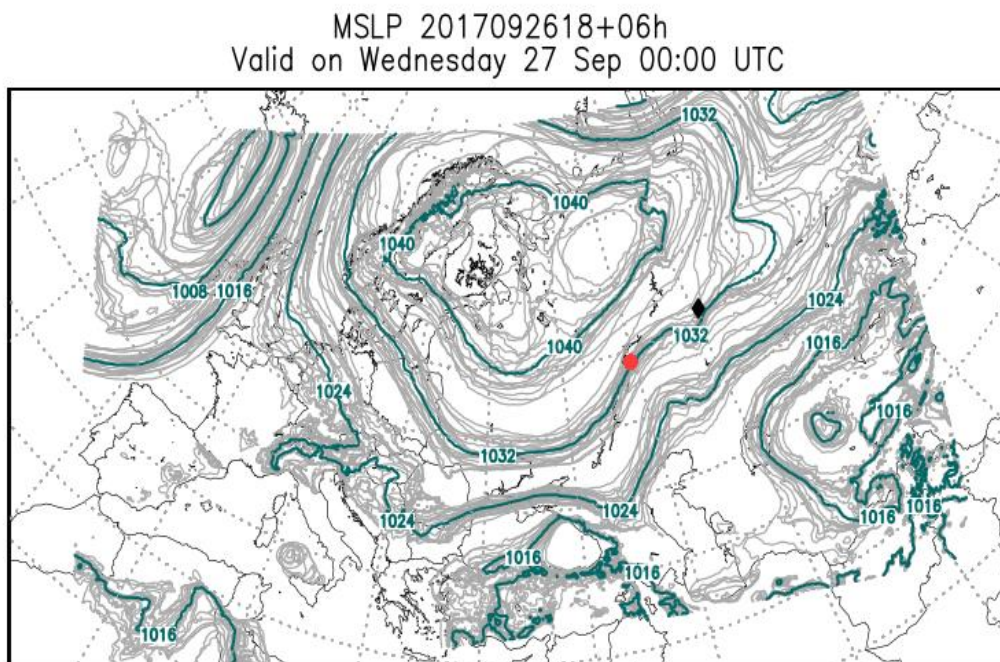
Figure 49 Mean sea level pressure spaghetti plot valid near the estimated time of the Ru-106 release. Locations of the two potential release points are indicated by the red dot and black diamond. Unperturbed control run is coloured, the 20 perturbed members are grey.

10m wind 2017092618+06h
Valid on Wednesday 27 Sep 00:00 UTC
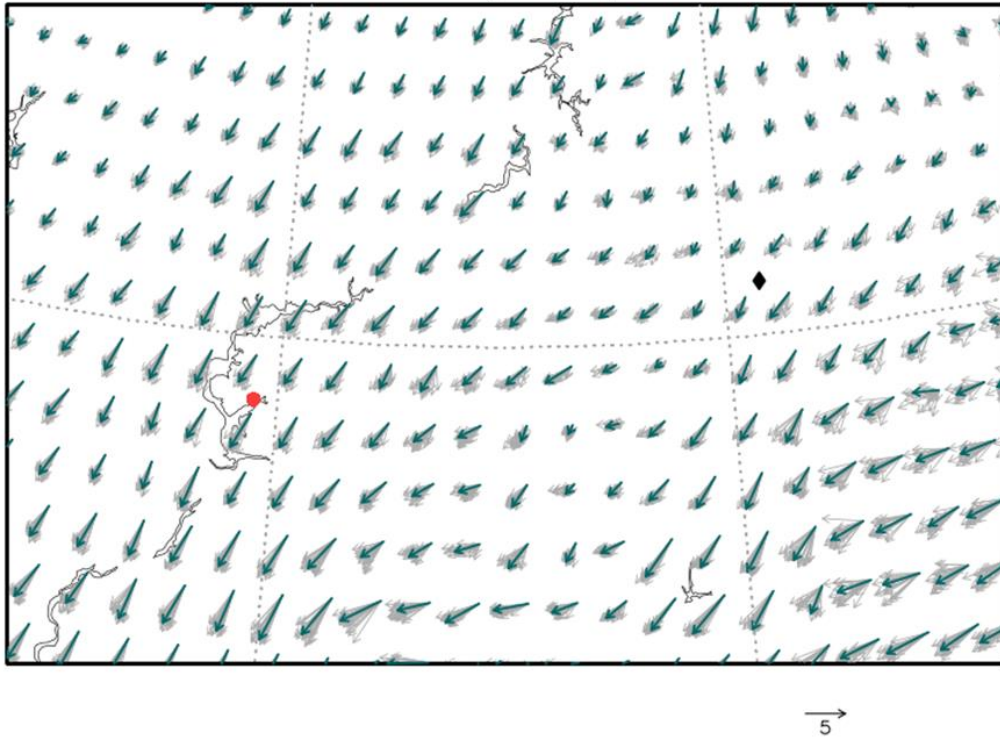
Figure 50 As Figure 49, but for 10m wind vectors in the area around the two potential release points.

2017092618+12h, precip [mm/12h]
Valid on Wednesday 27 Sep 06:00 UTC
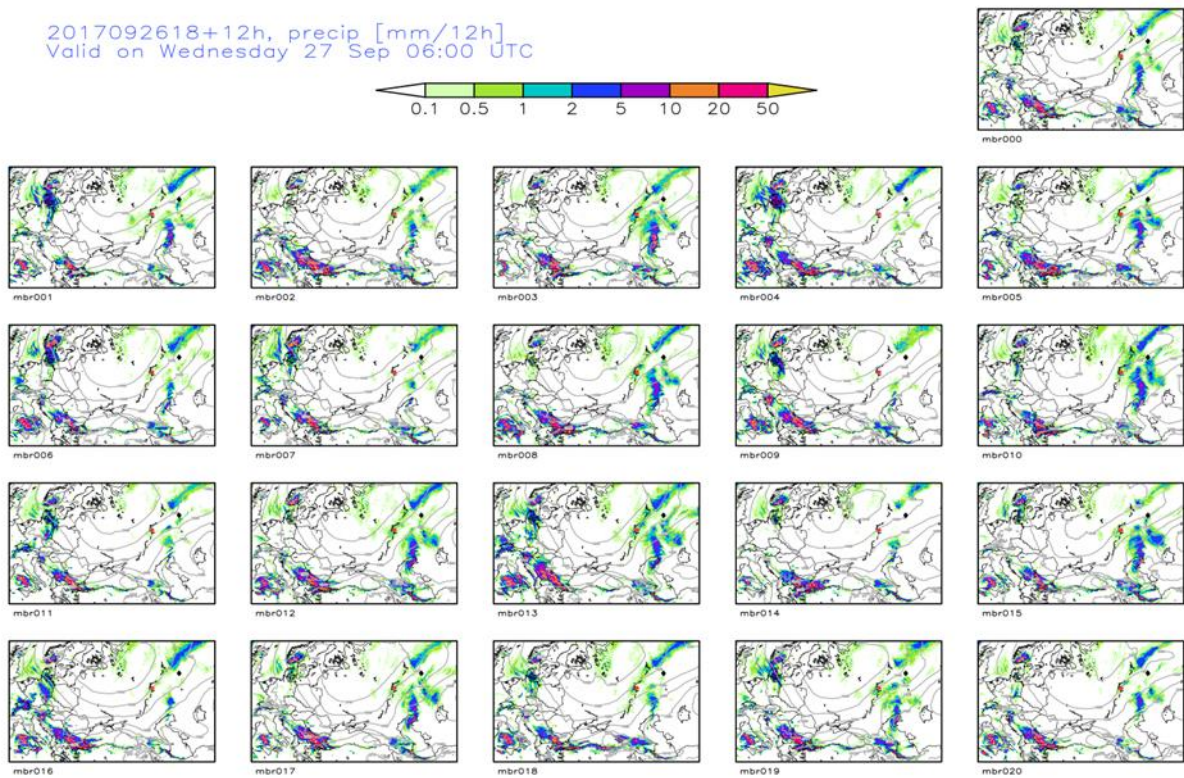
Figure 51 Precipitation "postage stamp" valid from 18 UTC 26 Sep - 06 UTC 27 Sep 2017 for the control run (mbr000) and the 20 perturbed members.

Deterministic results of DERMA

The filter station measurement data employed are confined to non-zero measurements and sampling periods less than 36 hours. Thereby, the data set is reduced to 89 measurement data. For each of these data, the DERMA model has been run in inverse mode backwards in time. Thereby the whereabouts of Ru-106 is estimated before arriving at the filter stations; cf. Figure 52 for a few examples. The observed time-average concentration values are used by the dispersion model by tracing Ru-106 back in time from the filter stations at measurement heights with start concentration values within the averaging time periods given by the measured average values. We assume that the detected Ru-106 originates from the same geographically fixed ground-level release location allowing for the release to have taken place during a finite time period.

As shown in Figure 52, individual measurements do not pin-point the location of the potential release point giving rise to extended geographical sectors only. However, by identifying the overlap of the inverse plumes, one obtains a better localization. In the following, model calculated influence functions, e.g. concentration, are shown at 2 m above ground. Obviously, the influence functions extend further in the vertical, but due to the assumption of a ground-level release, concentration values aloft are not shown here.
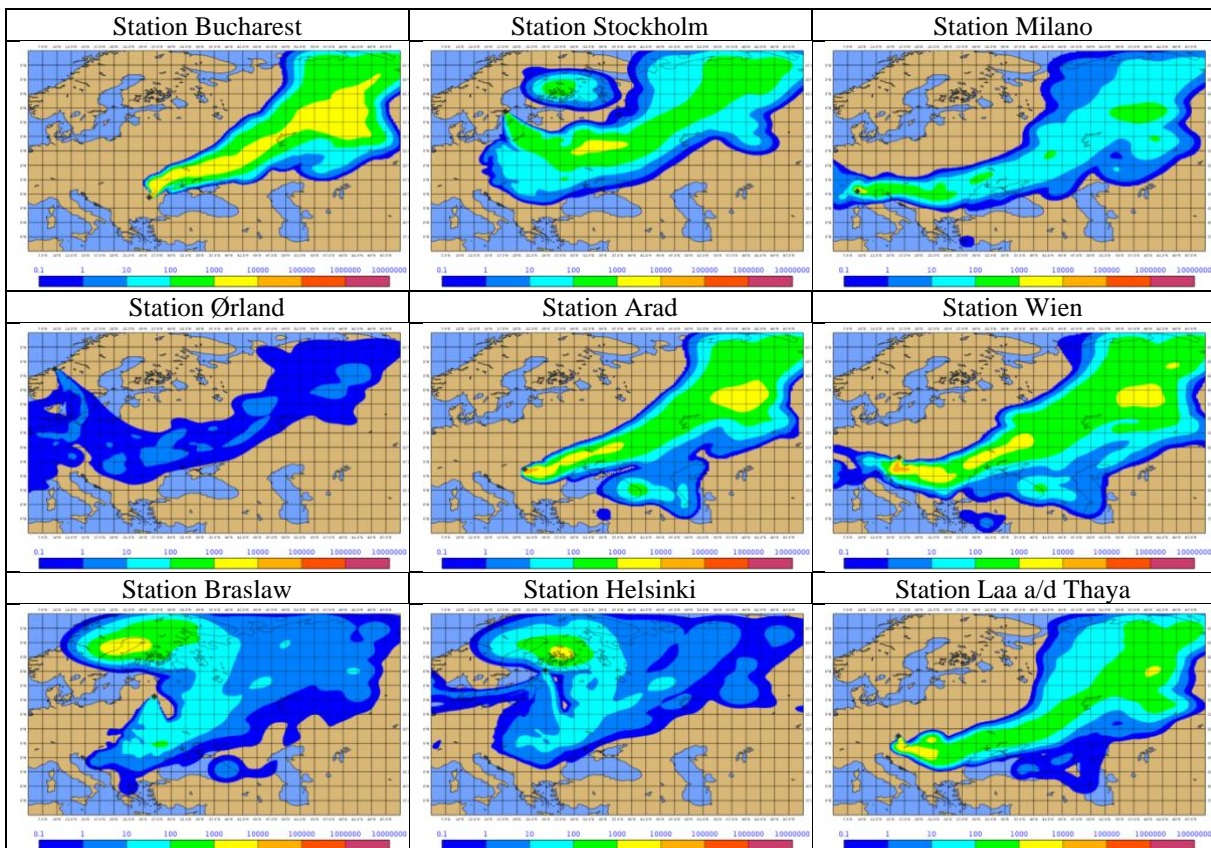
Figure 52 Time-integrated 2-m concentration in units of Bq h/m^3 of inverse plumes valid at 2017-09-26, 00 UTC. The filter stations are indicated by black diamonds.

Figure 53 shows the time series of the 20th percentile of the set of inverse concentration values corresponding to the non-zero filter station measurements.

2017-09-26, 00 UTC	2017-09-26, 12 UTC	2017-09-27, 00 UTC
2017-09-27, 12 UTC	2017-09-28, 00 UTC	2017-09-28, 12 UTC
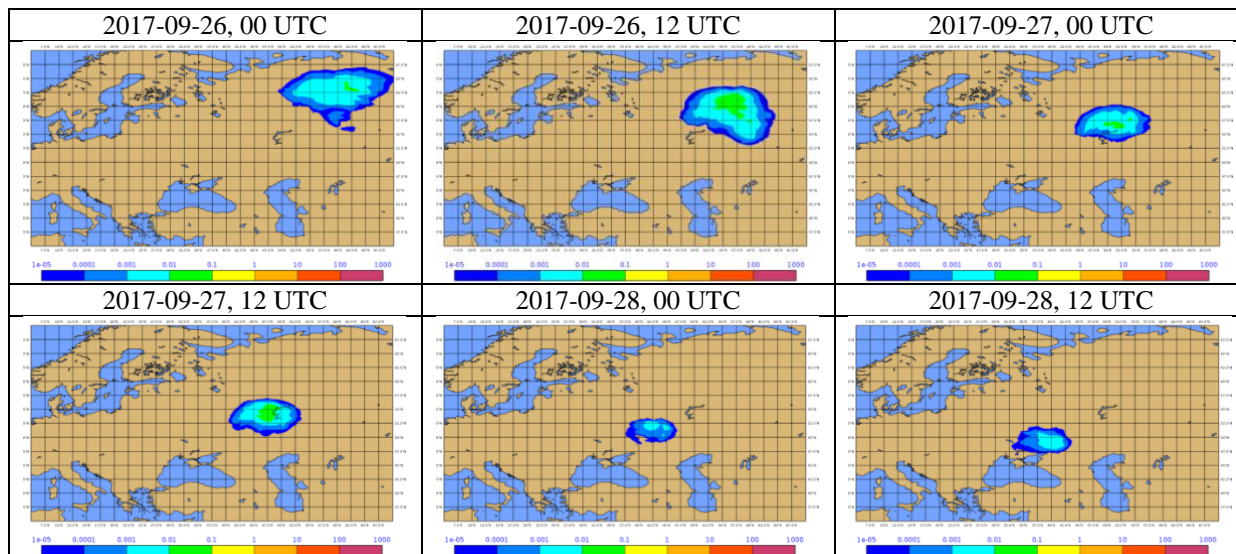
**Figure 53** Time series of the 20th percentile of the set of inverse concentration values corresponding to the filter station measurements.

The time series of these 20th percentile maps has been combined in one plot in the left-hand side of Figure 54 which thereby depicts the estimate of the potential location of the release of Ru-106. The release point is thus expected to be located inside a narrow geographic zone ranging from around Perm and Yekaterinburg in the north-east to Odessa in the south-west. In the right-hand side is shown the corresponding figure using the 30th percentile maps. The larger the percentage used for the percentile, the larger the disagreement is accepted between the individual inverse concentration calculations corresponding to measured values.

For operational use, the best (lowest) percentage used for the quantile calculation is not known a priori. The value depends both on the distribution of the measured concentration values and on how well-conditioned the problem is, i.e. how well the observations match the plume geographically and temporally. Thus, the recommendation is to calculate a range of percentiles which is anyway cheap from a computational point of view. In near real time in an operational environment, the problem is likely to be ill-conditioned at the early phase where only few measurements are available.
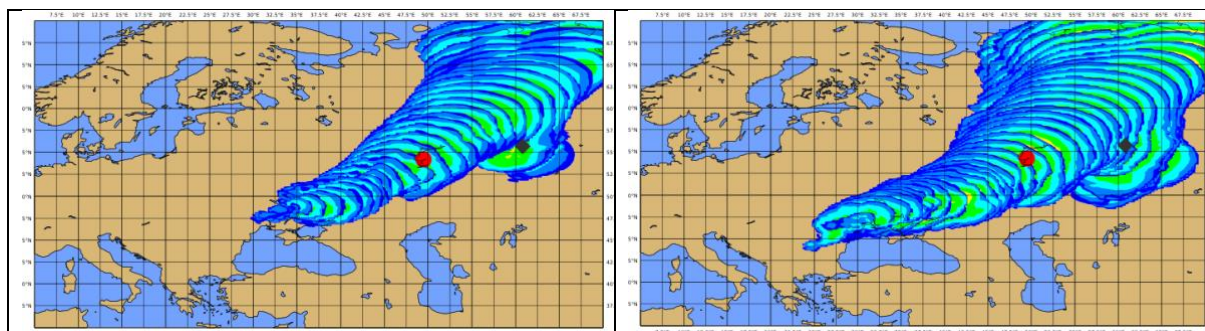
Figure 54 Estimates of the potential location of the release of Ru-106. The release point is located within a geographic zone ranging from around Perm and Yekaterinburg in the north-east to Odessa in the south-west. The left-hand figure consists of the overlapping time series of three-hourly 20th percentile inverse concentration maps from 2017-09-25 00 UTC to 2017-09-29 15 UTC, the right-hand figure consists of 30th percentile maps from 2017-09-25 00 UTC to 2017-09-30 18 UTC. With a red dot and a black diamond, the NIIAR and the Mayak nuclear facilities are indicated, respectively.

The geographic zones depicted in Figure 54 agree well with the corresponding zone estimated by a different method by Institut de Radioprotection et de Sûreté Nucléaire (IRSN, 2017). However, the method presented in the current paper is probably less computer resource demanding than the IRSN method.

It has been suggested that the release site could be the NIIAR nuclear facility, JSC "SSC RIAR", Russian Federation, 433510, Ulyanovsk region, Dimitrovgrad, Zapadnoye Shosse 9, cf. http://www.niiar.ru. If this is so, then according to the time series of the inverse model results, the release should have taken place within the time period 0–16 UTC on 2017-09-27. Likewise, it has been suggested that the release could be the Mayak Production Association, Russian Federation, Ozersk, Tjeljabinsk oblast, Lenin str. 31, cf. http://www.po-mayak.ru/. If so, according to the inverse model results, the release should have taken place in the time period 5–13 UTC on 2017-09-26.

Ensemble-statistical results of DERMA

For each of the ensemble prediction model members described in section "Harmonie Ensemble Prediction System runs for the Ru-106 case", the DERMA atmospheric dispersion model system has been set up to run in inverse mode using the observational data set described in the previous section.

Overlap method

The overlap method (Sørensen, 2018) is applied to the combined set of filter station measurement data confined to non-zero measurements and sampling periods less than 36 hours. This amounts to 89 non-zero observational data which multiplied by 21 meteorological ensemble members equals nearly two thousand time series of inverse concentration fields constituting the input to the localization procedures based on calculation of percentiles hereof.
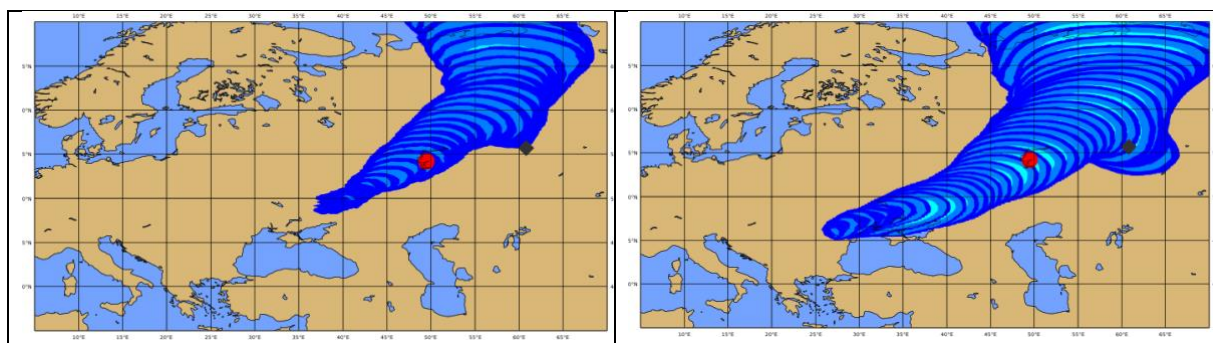
Figure 55 Estimates of the potential location of the release of Ru-106 using the NWP model ensemble and limiting the filter station measurement data to non-zero measurements and sampling periods less than 36 hours. The release point is located within a geographic zone ranging from around Perm and Yekaterinburg in the north-east to Odessa in the south-west. The left-hand figure consists of the overlapping time series of three-hourly 20th percentile inverse concentration maps from 2017-09-25 00 UTC to 2017-09-29 15 UTC, the right-hand figure consists of 30th percentile maps from 2017-09-25 00 UTC to 2017-09-30 18 UTC. With a red dot and a black diamond, the NIIAR and the Mayak nuclear facilities are indicated, respectively.

In the left-hand side of Figure 55 are shown the time series of the 20th percentile maps combined in one plot, which thereby depicts the estimate of the potential location of the release of Ru-106. In the right-hand side is shown the corresponding figure using the 30th percentile maps.

The geographic zones depicted in Figure 55 agree well with the corresponding zones estimated by the deterministic calculation, Figure 54.

If the NIIAR nuclear facility is the release point, then according to the percentile plots, the release should have taken place in the time period from around 15 UTC on 26 September to 15 UTC on 27 September, 2017. Likewise, if the release point is Mayak, then the release should have taken place in the time period from around 06 UTC on 24 September to 12 UTC on 26 September. In both cases, the estimated release period is longer than for the deterministic results.

Figure 56 shows similar results, for each of the individual meteorological ensemble members. From this multi-plot, the effects of the inherent meteorological uncertainties on the localization of the source can be readily seen.
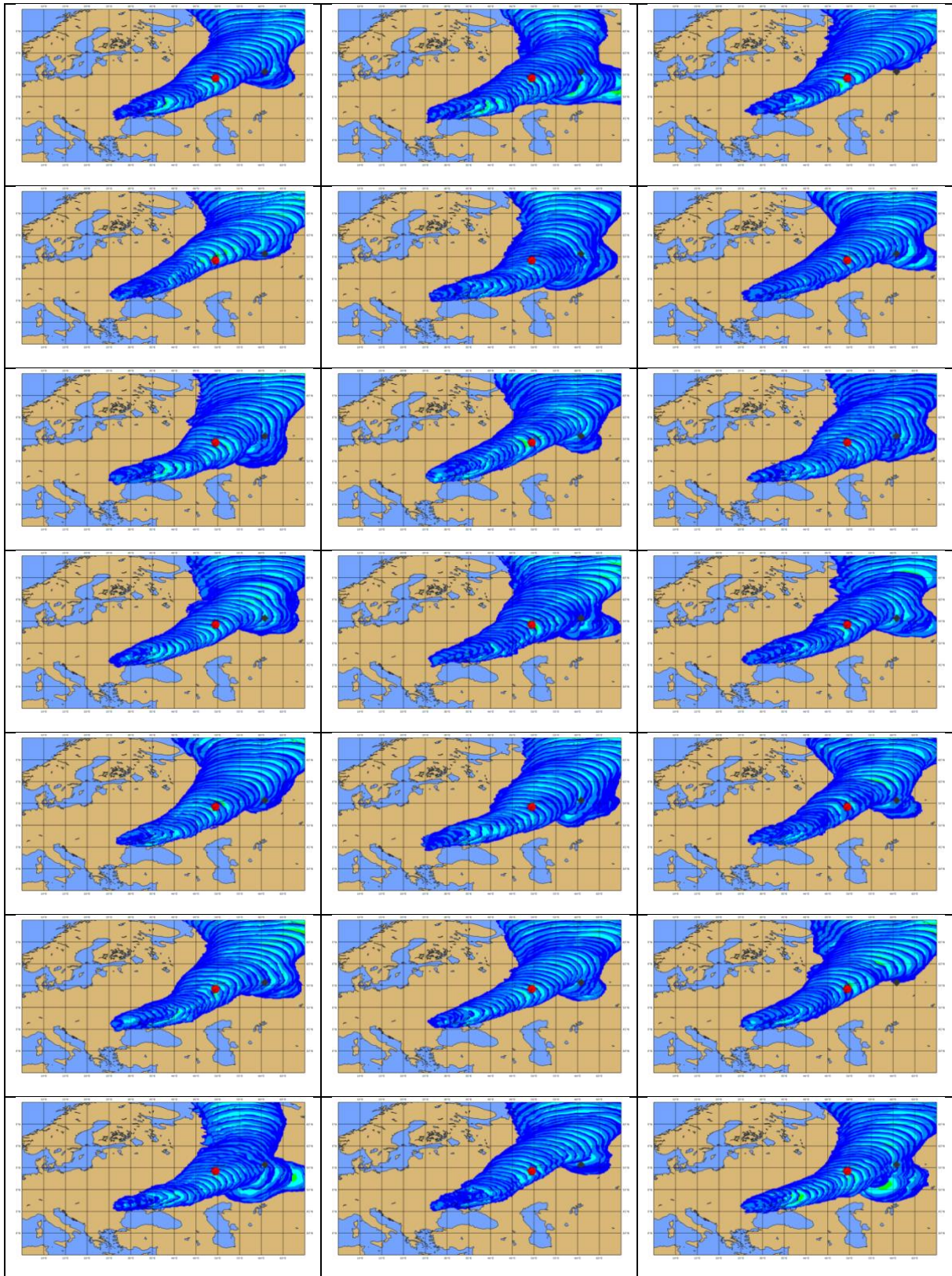
Figure 56 Estimates of the potential location of the release site for each of the NWP model ensemble members. For details, cf. Figure 55.

By abandoning the constraint that the sampling periods are less than 36 hours, and including also the week-long sampling periods, the data set is enlarged to 238 non-zero observations which multiplied by 21 meteorological ensemble members equals nearly five thousand time series of inverse concentration fields constituting the input to the localization procedures based on calculation of percentiles hereof.
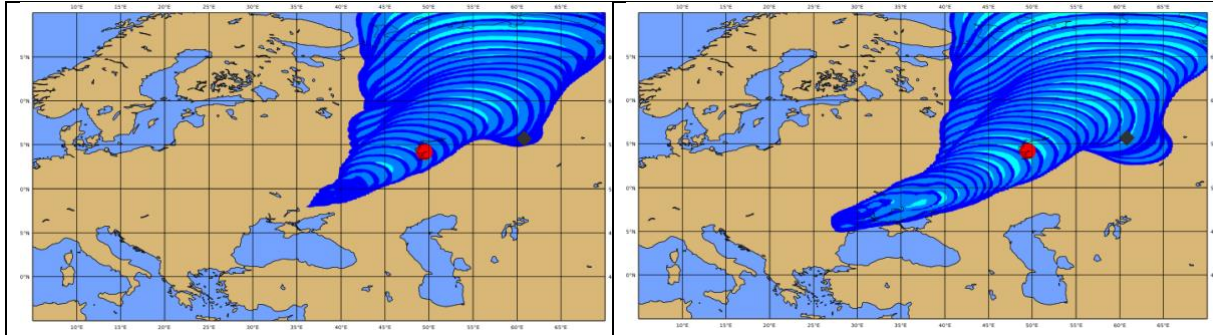

Figure 57 Estimates of the potential location of the release of Ru-106 using the NWP model ensemble and extending the filter station measurement data to include also week-long periods. The release point is located within a geographic zone ranging from around Perm and Yekaterinburg in the north-east to Odessa in the south-west. The left-hand figure consists of the overlapping time series of three-hourly 20th percentile inverse concentration maps from 2017-09-25 00 UTC to 2017-09-29 15 UTC, the right-hand figure consists of 30th percentile maps from 2017-09-25 00 UTC to 2017-09-30 18 UTC. With a red dot and a black diamond, the NIIAR and the Mayak nuclear facilities are indicated, respectively.

In the left-hand side of Figure 57 are shown the time series of the 20th percentile maps combined in one plot, which thereby depicts the estimate of the potential location of the release of Ru-106. In the right-hand side is shown the corresponding figure using the 30th percentile maps.

Comparing Figure 55 and Figure 57, we see that the inclusion of measurement data corresponding to week-long filter station sampling periods implies that the overlap plots become wider, and thus that the localization is less focused. This agrees well with the initial assumption that daily measurements are of greater value for localization purposes due to the fact that a week can cover a number of different meteorological phenomena taking place over the station site.

Bayesian method

The results are obtained similarly to what was described for the ETEX-1 case in section "Bayesian inversion combined with an adjoint dispersion representation". In Figure 58, the results are shown for a selection of values of $\sigma_{\min}$ and α. In the ETEX-1 case, the values of $\sigma_{\min}$ and α were chosen based on examination of the error distribution $\left(R_i\left(\boldsymbol{m}^{(t)}\right) - d_i\right)/$ $\sigma_i\left(\boldsymbol{m}^{(t)}\right)$. Since the true source term is not known in the Ru-106 case, this is of course not an option. Instead, finding adequate values were based on trial and error. As discussed previously, the NIIAR and the Mayak nuclear facilities have been suggested as possible release sites. Thus, these are marked on the figures with a red and black diamond, respectively.
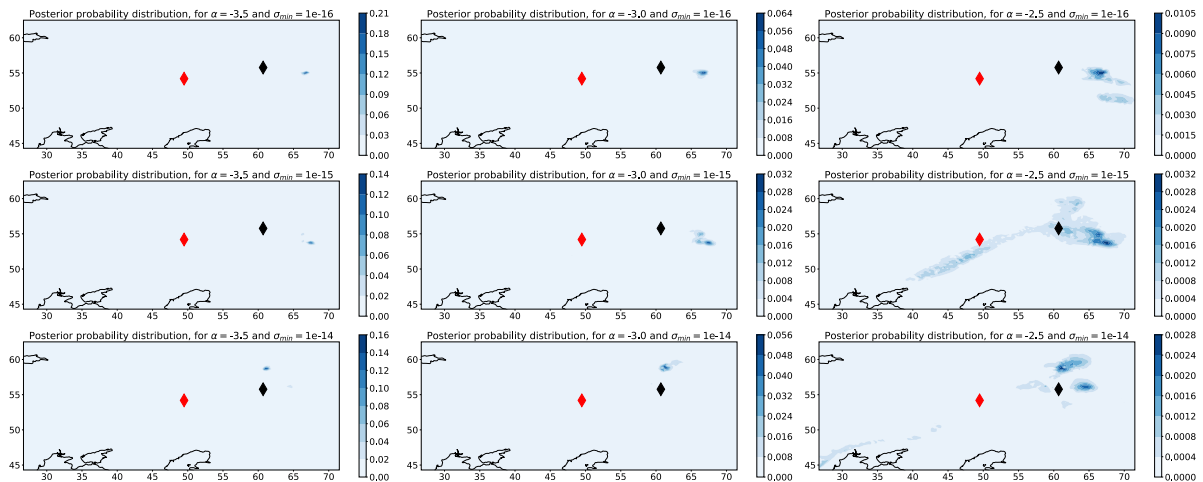
Figure 58 Posterior probability distributions for Ru-106 case. The red and black diamonds show the locations of the NIIAR and the Mayak nuclear facilities, respectively. The figures differ only by the values of $\boldsymbol{\sigma}_{\min}$ and $\boldsymbol{\alpha}$ (shown in the figure titles).

Again, we see that the choice of $\sigma_{\min}$ affects the location of the peak of the posterior probability distribution, whereas α changes the width of the posterior distribution. Thus, the behaviour of these parameters is consistent with what we saw in the ETEX-1 case. Since the adequate values of $\sigma_{\min}$ and α are unknown, we can, at best, hope for the correct source location to be located within, or near, one of the resulting posterior distributions. It is important to note, however, that all distributions point towards locations somewhat near the Mayak nuclear facility. Especially when we allow for larger distribution widths (the right column in Figure 58), the distributions to some extend agree that the most likely area is somewhere either east or north of Mayak.

Again, we examine the role of the meteorological ensemble by comparing to an experiment where the standard deviation $\sigma_{C_i^*}$ is set to $\sigma_{C_i^*} = 0.5\ C_i^*$. The result is shown in Figure 59 (right) and compared to the ensemble-based approach in Figure 59 (left). As in the ETEX-1 case, we see that the two probability distributions are quite similar (at least when comparing to the variation we get for different values of $\sigma_{\min}$).
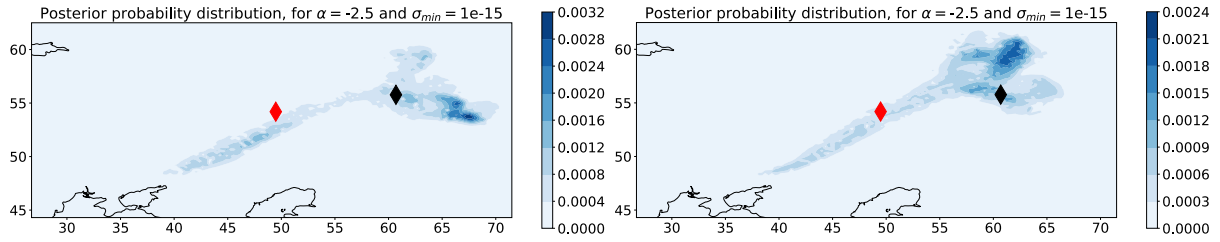
Figure 59 The left figure shows the result using the standard deviation of the ensemble members to estimate the model uncertainty, whereas the right figure shows the result assuming $\boldsymbol{\sigma_{C_i^*} = 0.5\, C_i^*}$.

Assuming that we have found some adequate values of $\sigma_{\min}$ and α, the results indicate that there is an area of higher probability around the Mayak nuclear facility. This result is quite consistent for the different $\sigma_{\min}$ values ranging from 10^{-16} to 10^{-14}, and it is in agreement with the results of other studies.

As discussed previously, it is a disadvantage of this method that the choice of the hyperparameters $\sigma_{\min}$ and α may impact the location of the most likely source. Further, the results from both the ETEX-1 and the Ru-106 cases indicate that the meteorological ensemble did not provide an adequate estimate of the adjoint dispersion model uncertainty without additional assumptions, and that the resulting posterior distribution does not change significantly when using a simpler uncertainty quantification method. This indicates that source localization does not rely on an accurate uncertainty description, which correctly captures the meteorological uncertainties. Thus, further studies should perhaps examine much simpler approaches and try to avoid the need of the hyperparameters $\sigma_{\min}$ and α.

Deterministic results of MATCH

Both Markov Chain Monte Carlo and percentiles for individual plumes were applied to the Ru-106 case in 2017, using the MATCH model.

Markov Chain Monte Carlo

The MCMC approach was applied having starting points in three locations: Dimitrovgrad, Mayak and an additional position in between. The full dataset (387 measurements) of various sampling integration times where used. The approach converges in all cases but end rather close to the starting point. The additional point in between Dimitrovgrad and Mayak converge to more or less the same location as when starting in Mayak. Figure 60 shows the results for these three evaluations. Making a step to Figure 62 and percentiles of time-integrated total columns there is a signal that both Dimitrovgrad and Mayak may be possible release sites, being on a path of max percentile values. The MCMC approach very much search towards a nearby point on this path of max values that falls within a similar emission time-profile as for the starting point in the MCMC procedure.
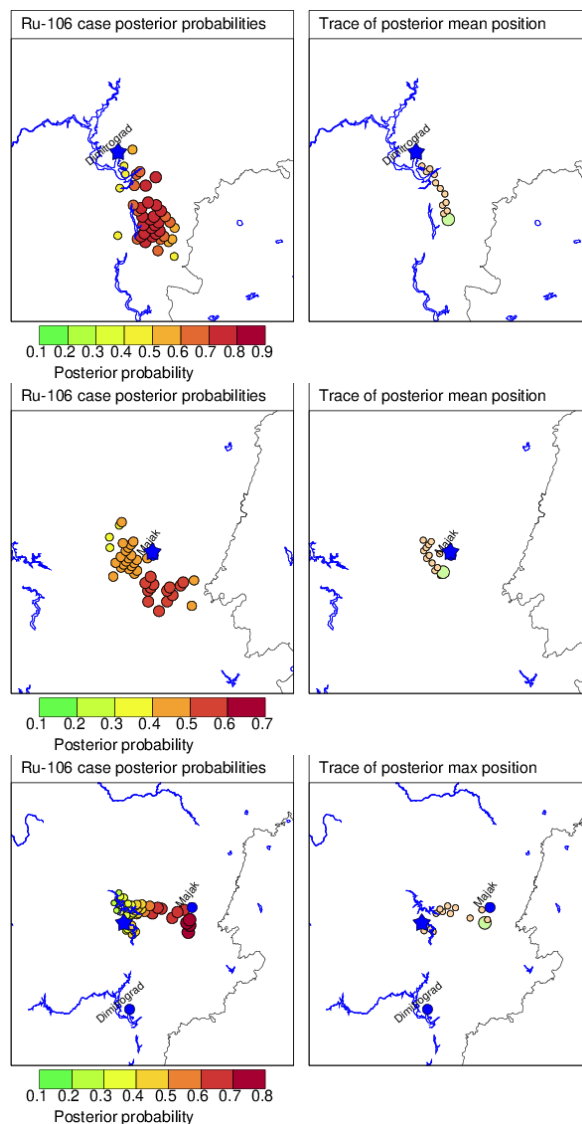
**Figure 60** Markov Chain Monte Carlo simulations for Dimitrovgrad (top) and Mayak (middle), and a location in between these sites (bottom). Posterior probabilities for visited locations are shown to the right and the mean path thru the iterations are shown to the left (for the bottom case max position trace became more informative). The starting point for MCMC is marked with a blue star, and the end point with a green bullet.

Percentiles for individual plumes

The percentile approach was as for the ETEX-1 case evaluated on a reduced set of measurements. From in total 387 measurements a set of 131 did provide measurements with up to 36 hours sampling times. From this latter sub-set 30 measurements were depicted. The first 10 with highest measured values were taken and the remaining 20 were randomly selected by weighted bootstrapping (conditional on measured values). Figure 61 shows all the sites for the 131 measurements (left) and the used sites with the selected 50 measurement (right).
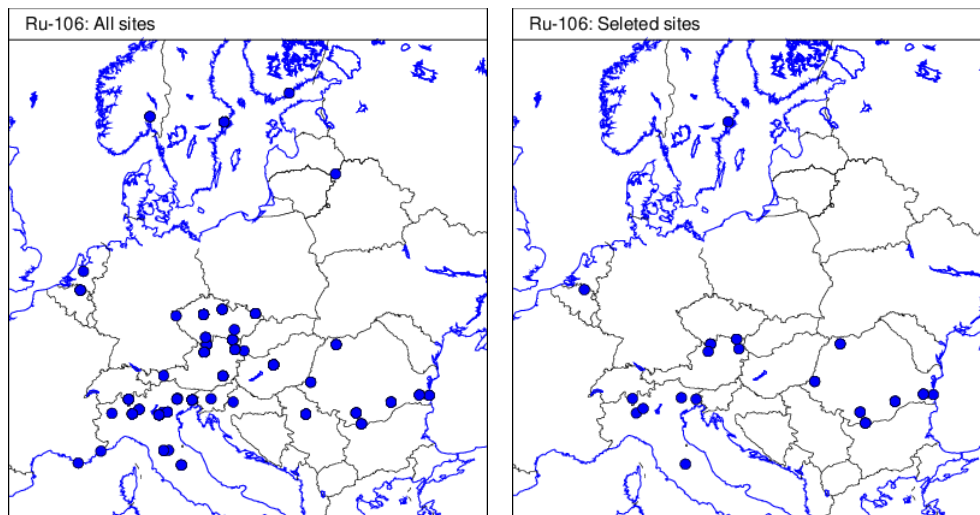
Figure 61 All sites provided from IAEA providing measurement with up to 36 hours sampling times (left) and the selected ones (right).

Individual plumes were made for each measurement with a unit response assumed valid over a depth of 50 m and distributed over the time-interval for the measurement (ranging from 7 to 36 hours). In post processing, each inverse plume was scaled by measured value associated with the plume.

Figure 62 shows the 70th percentile of total columns as well as 70th percentiles of time-integrated total columns for the 25, 27 and 28 September, 2017. The total column is selected to include a vertical extension of the source. The percentiles of time-integrated columns should be interpreted as showing possible source location at any time back to the date plotted. This covers a larger area for the Ru-106 case but showing max values in a band from Italy, Ukraine and southern Russia. The plotted dates are selected to illustrate approximate dates for any releases at Dimitrovgrad and Mayak.
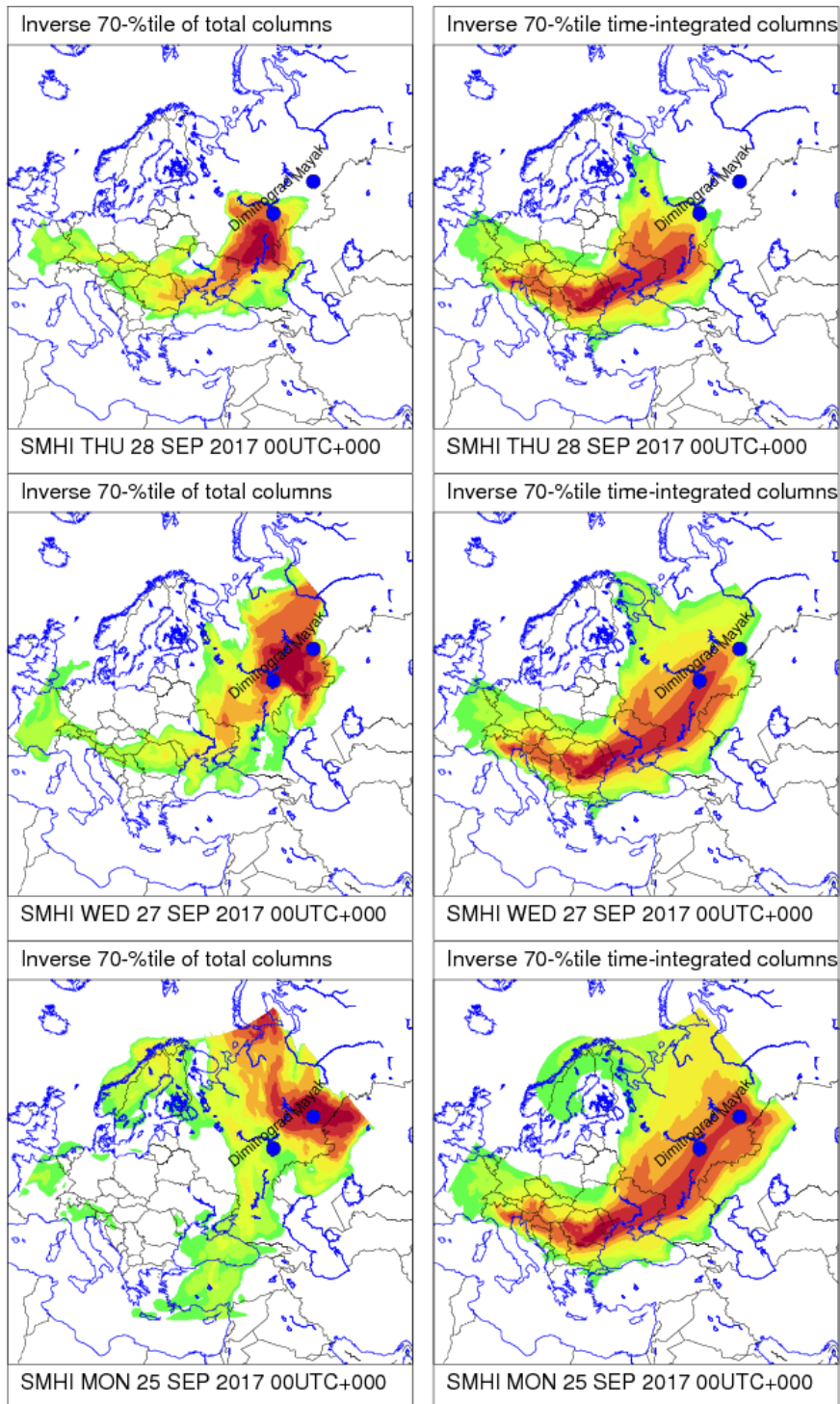
Figure 62 Assignments of possible source areas as given by 70th percentiles of total columns (left) and 70th percentile of time-integrated total columns (right). The percentiles are normalised to simplify plotting. Dates plotted are 28 Sep 00 UTC, 2017 (top), 27 Sep 00 UCT (middle) and 25 Sep 00UTC (bottom). The locations for Dimitrovgrad and Mayak are plotted.

Ensemble-statistical results of MATCH

The MATCH results are for the ensemble weather data confined to statistics from column integrated inverse plumes. The MCMC approach is for this part left for later exercises. The observations used are the same as shown in Figure 61 above. As for the ETEX-1 case MATCH has been applied to a reduced set of ensemble members: 0, 5, 10, 15 and 20. In order to make the MATCH model digest the observations in one run the domain and resolution lead to memory issues. The weather ensemble predictions where therefor remapped to $0.1°×0.1°$ resolution. This is not a limitation given that the observation responses are at least a day long and a model resolution of $0.5°×0.5°$ then becomes ambitious.

We will for the Ru-106 present the following statistics

- Sum of plumes, 90 percentiles, level of agreement (voting) for a few ensemble members
- Overlay plots including several time-steps for 90 percentile and voting for a few ensemble members
- Overlay plots with mean and median of 90 percentile and voting.

The level of agreement (voting) is made up by counting the number of adjoint plumes that are above a given threshold, normalised by the number of plumes available. The threshold is crucial for this measure and for the Ru-106 case set to 10^{-3}.

In Figure 63 we illustrate the various outputs with sum of plumes, 90 percentiles and voting for the members 0, 10 and 15 at 12 UTC 26 September, 2017. The figure illustrates that the 90 percentile is very much confined while the voting is broader and as expected the full sum is mostly spread. For this date both the sum of plumes and 90-percentile have max close to Mayak, while the level of agreement has max somewhat to toward north.
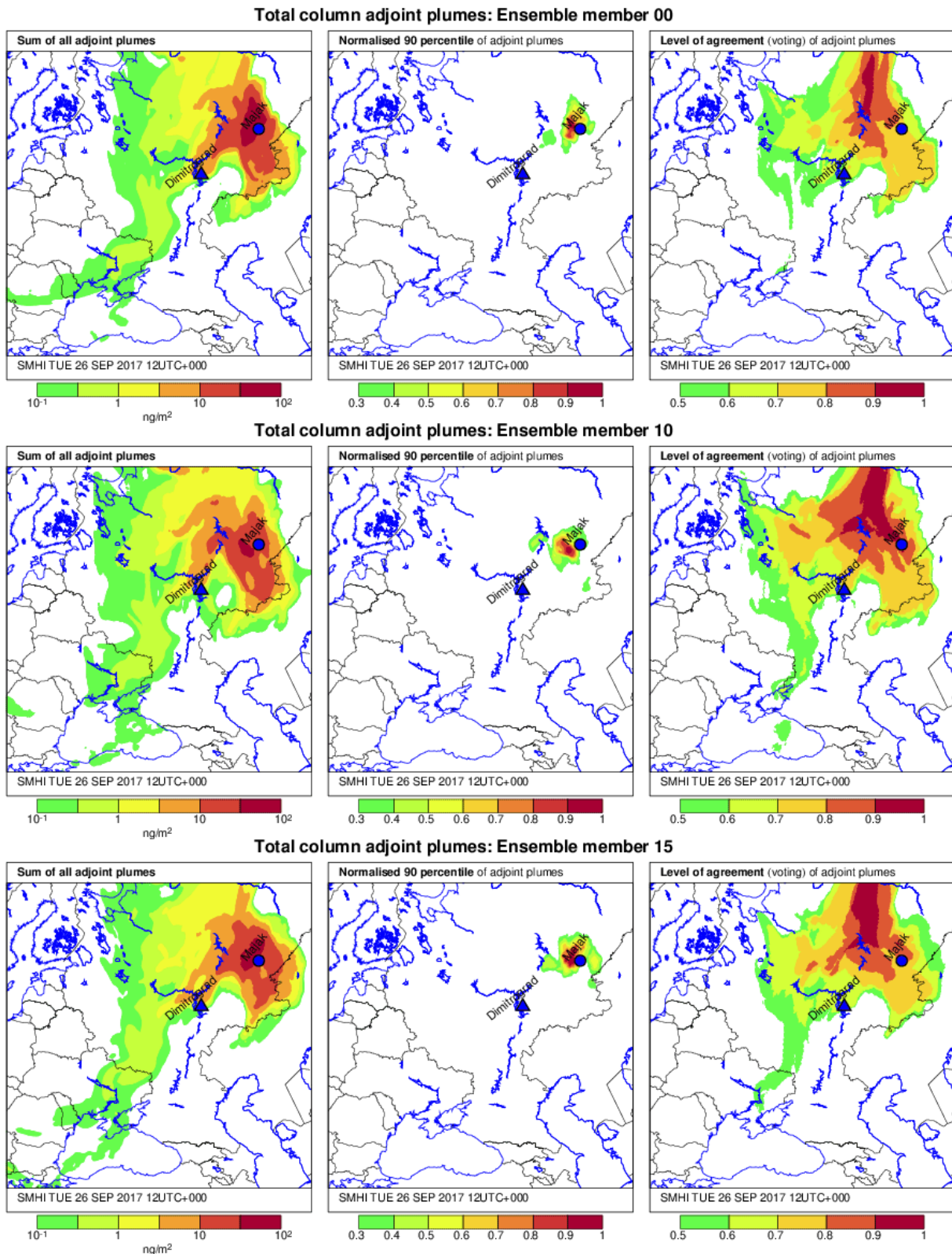
Figure 63 Example of statistics for 12UTC 26 September, 2017, for the Ru-106 case and for 3 ensemble members: 0 (top), 10 (middle) and 15 (bottom), where the sum of adjoint plumes are shown together with the 90 percentile and level of agreements (voting).

In Figure 64 and Figure 65 are overlay plots where selected timesteps are plotted together for the member 0 and 20, and for 90 percentile and level of agreement, respectively. Here the time difference is 12 hours and the colour scheme is alternating in order to better separate the time-steps. The two alternating colour schemes goes from green to red and blue to red, respectively. The 90 percentiles provide a more restricted adjoint response while the level of agreement aggregates more of the information from the individual adjoint plumes. There are differences in the outcome using the ensemble weather predictions but the main feature remains similar. The setup with consecutive ensemble runs where each member is disconnected from its predecessor with the same member number may contribute to the similarities.
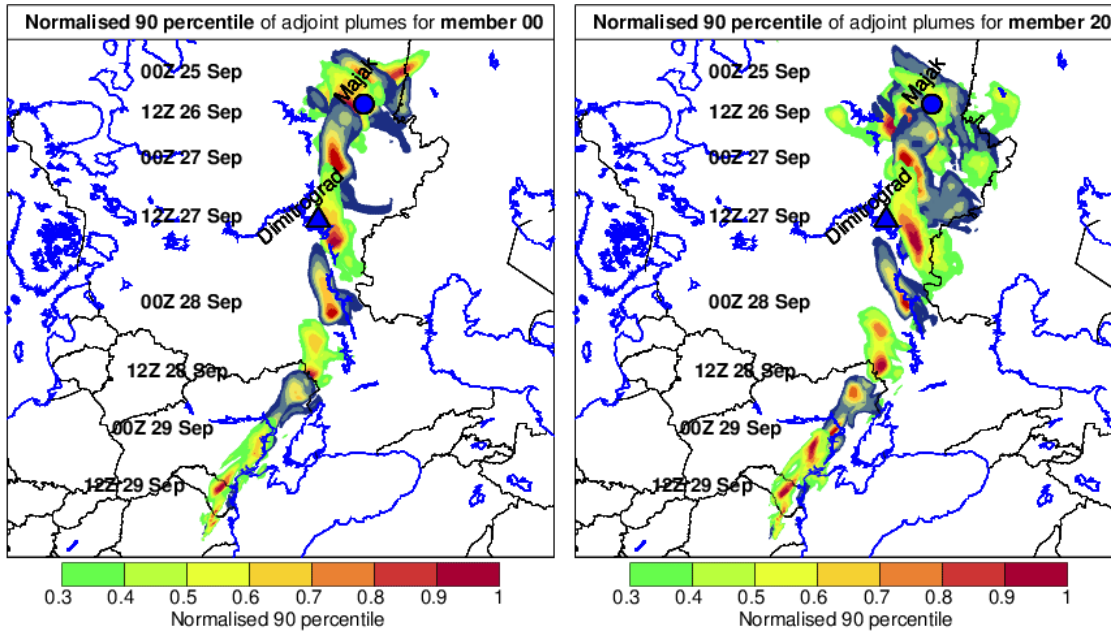

Figure 64 Overlay figure for selected dates for **90 percentiles** for member 0 and 20. Alternating colour schemes are used to separate the time-steps.
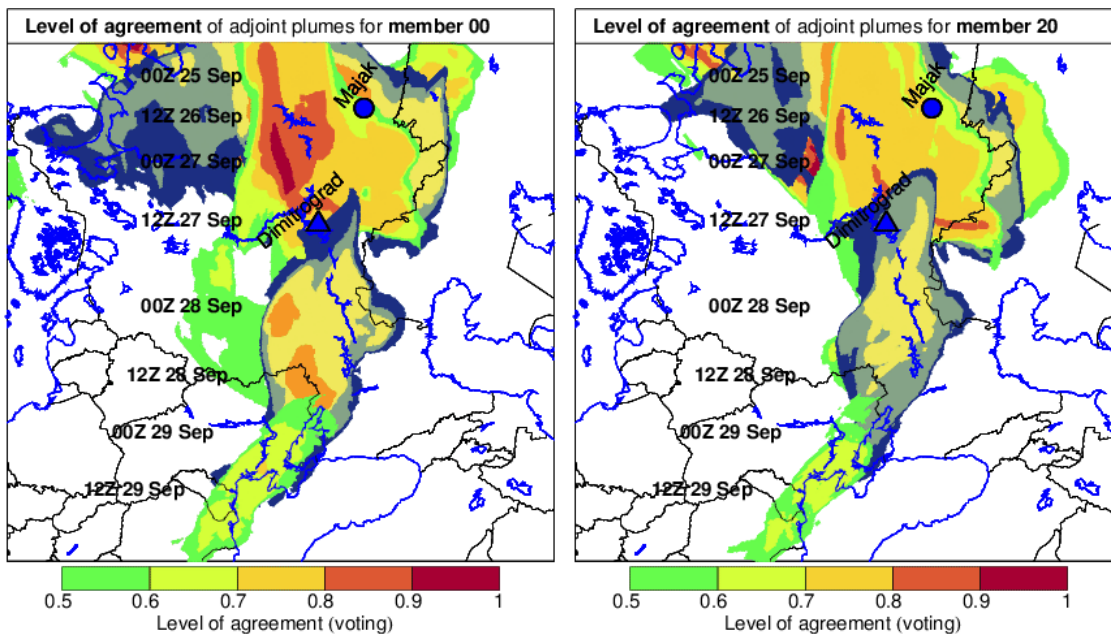
Figure 65 Overlay figure for selected dates for **level of agreement** (voting) for member 0 and 20. Alternating colour schemes are used to separate the time-steps.

In Figure 66 and Figure 67 the ensemble mean and median (of this restricted number of members) are shown for 90 percentile (Figure 66) and level of agreement (Figure 67). These figures may represent the final output comprising the ensemble runs. Apparently the 90 percentile provides a more user-friendly output.
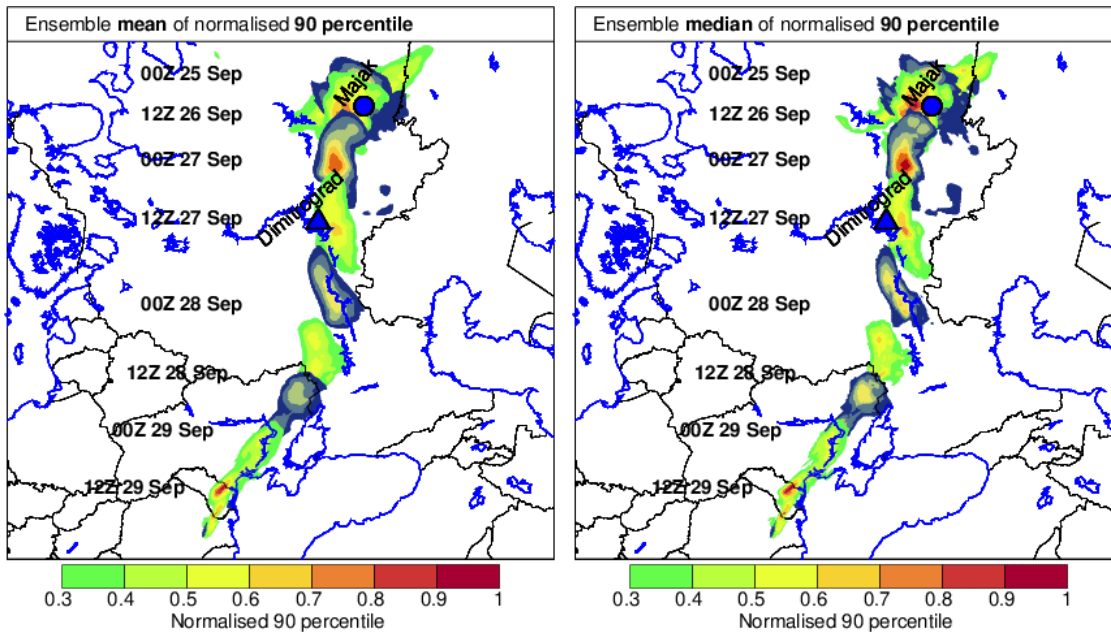
Figure 66 Overlay figure for selected dates for **ensemble mean** and **median** of **90 percentiles**, Alternating colour schemes are used to separate the time-steps.
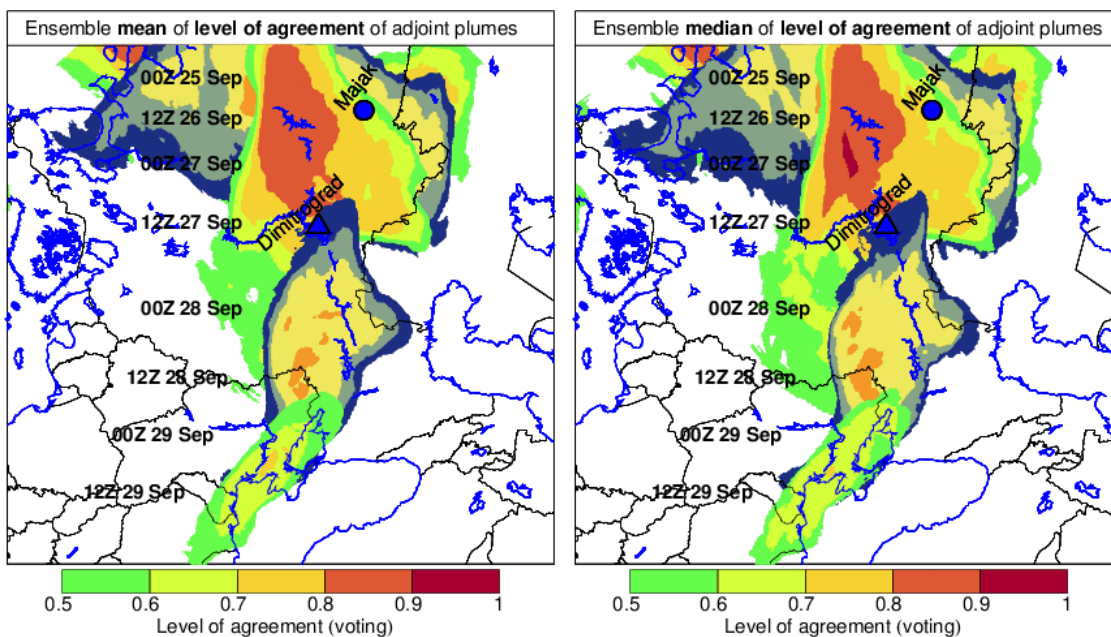
Figure 67 Overlay figure for selected dates for **ensemble mean** and **median** of **level of agreement** (voting). Alternating colour schemes are used to separate the time-steps.

Not clearly shown in the figures is that the 90 percentiles very much circulate around the Mayak site from 12UTC 25 September to 12UTC 26 September. Considering Mayak the likely site this time-range may then be suggested.

The overlay plots are suitable for printed version of the output, while for a real-time application a web-based visualisation system should enable the user to scroll through the data.

The level of agreement provides somewhat messy figures when overlaying several dates in the same figure. However, at the early stage where less observations are available the level of agreement (voting) would be the only alternative to just show the sum of adjoint plumes.

Deterministic results of SNAP

For the Ruthenium case, all 383 measurements, shown in Figure 68 were used, combining both the measurements below LOD and detections. The adjoint model was run back until 2017-09-22, 03 UTC. Figure 69 shows the maximal probabilities along with the development in time of the probability densities. The areas of high probability cover a larger area than for the ETEX-1 case, making an estimate for source location coarser.
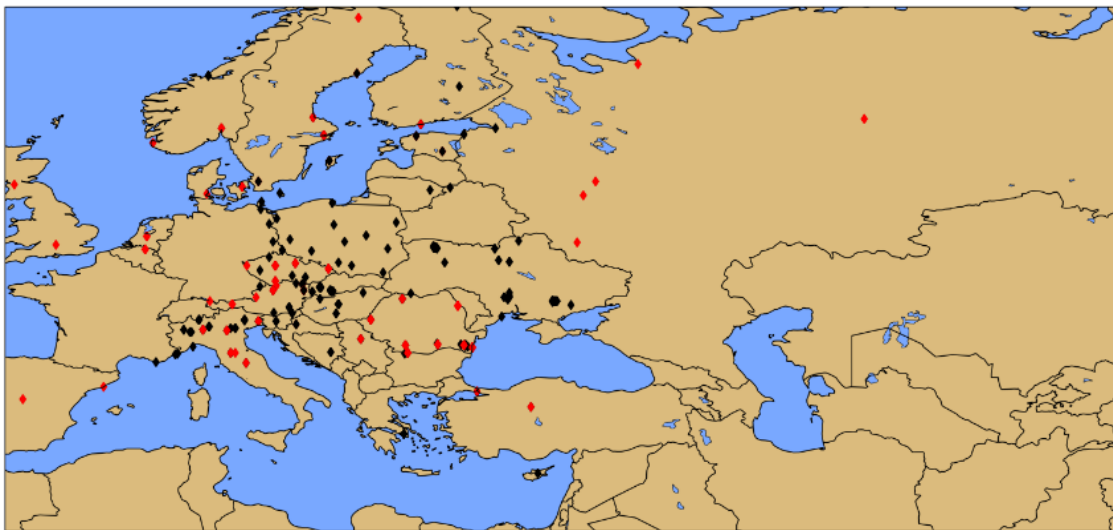
Figure 68 Location of stations in the Ruthenium case. Red diamonds show stations with measurements below LOD, black diamonds show measurements above LOD.

Examining different release durations gives Figure 70, showing the maximum probability densities for longer release durations than shown in Figure 69. The smaller area of the highest probabilities (dark red) for the two hour release duration, and much smaller areas for ten hours suggest a source lasting for only a short duration.
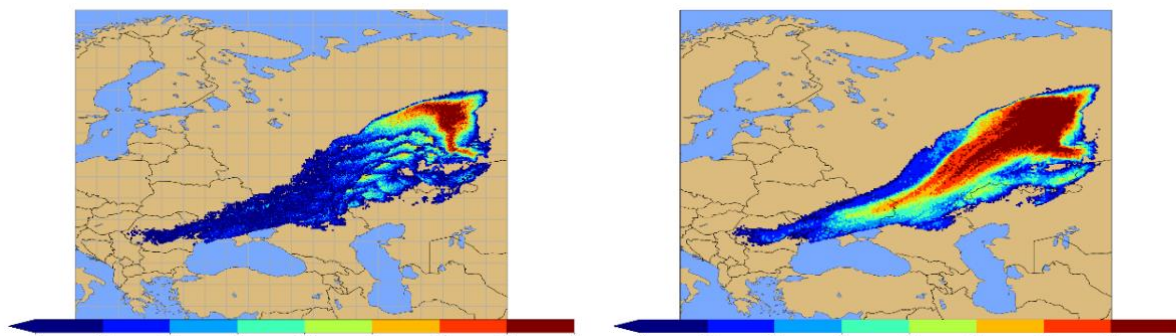
Figure 69 Probability densities assuming a one hour duration of the release for the period 2017-09-26, 00 UTC – 2017-09-28, 15 UTC. On the left slices of probability densities for every sixth hour are shown. On the right the maximum probability densities are presented.

The larger spread in probability densities could be a result of different thresholds and LOD for the various stations, compared to the more homogenous ETEX-1 case, suggesting the probabilities used should be dynamic per station, and scale with the dilution volume. The deterministic meteorological model used in the simulations does not capture any meteorological uncertainty, which might affect the long-range transport severely.
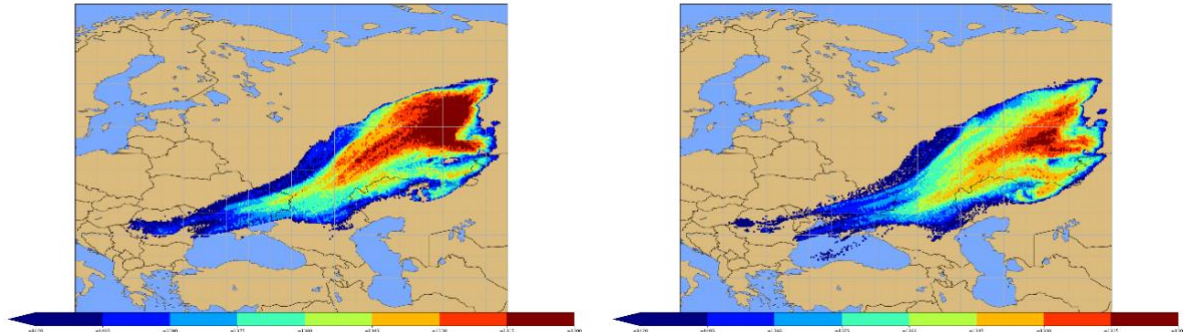
Figure 70 Maximum probability densities between 2017-09-26, 00 UTC - 2017-09-28, 15 UTC, assuming a two hour release duration on the left, and a ten hour release duration on the right.

Ensemble-statistical results of SNAP

The 21 ensemble meteorological members described in section "Harmonie Ensemble Prediction System runs" and 369 measurements (252 above the detection limit) were used to produce 21 estimates of the probability densities for the ruthenium case. The individual estimates are presented in Figure 71. A clear source localisation is not apparent, with the localisation favouring areas covered later in the dispersion runs.
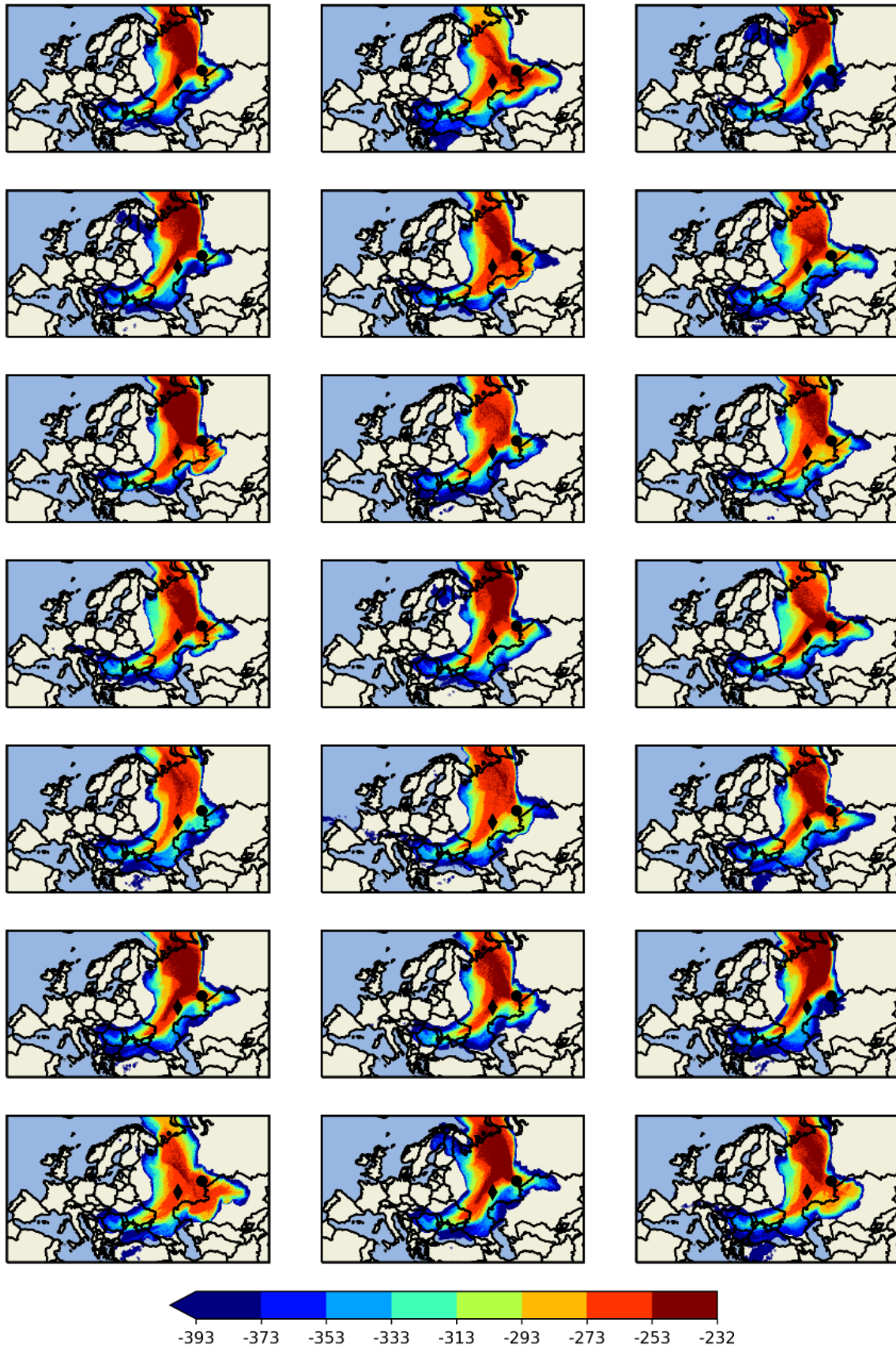
Figure 71 Probability densities resulting from dispersion results using the 21 meteorological ensemble members. Mayak and the Dimitrovgrad are indicated with a black circle and diamond respectively. Values are log probability (not normalized). Higher values signify higher probability of a release at this location.

Examining the ensemble mean of the individual probability densities results in Figure 72, both Mayak and Dimitrovgrad remain approximately equally likely when considering probability likelihoods. Examining individual start-times of the simulated release suggests a release around 2017-09-26T0 to 2017-09-26T12 is the most likely, see Figure 73.

The added benefit of using non-detections is shown in Figure 74 and Figure 75, where only stations with detection and those below their detection limit are used respectively. The measurements below the detection limit will eliminate areas to the northwest of Mayak and Dimitrovgrad.

Figure 72 Source localisation in the ruthenium case for the mean ensemble probability. See Figure 71 for further details.

Figure 73 Source localistion for the ruthenium case when considering starting times of releases at 2017-09-25T12 (furthest north), 2017-09-26T0, 2017-09-26T12, and 2017-09-27T0. See Figure 71 for further details.

Figure 74 Source localisation using only stations with valid detections. See Figure 71 for further details.

Figure 75 Source localisation using only stations where detections were below the sensitivity of the station. Note that higher values are more likely. See Figure 71 for further details.

A possible reason for the difficulties in localising the source area could be due to varying duration of measurements at the stations. Figure 76 shows how inhomogeneous the measurement periods are. This is problematic as shorter sampling periods could give higher detection limits, and more false negatives for the examined method.
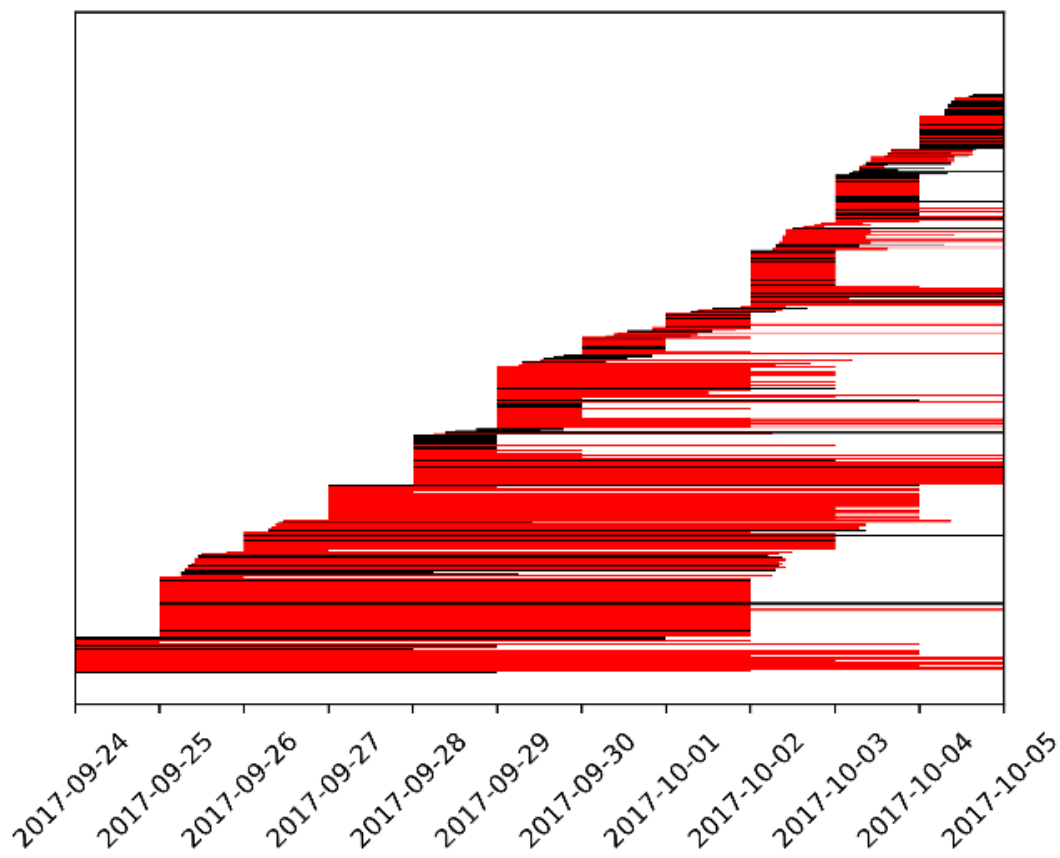
Figure 76 Station measurements during the ruthenium episode. Red bars mark measurements above the limit of detection (LOD), black bars mark measurements below the LOD.

ARGOS and Source Localization

The Long Range dispersion model interface in ARGOS is capable of providing an ensemble of source terms – a list of possible release descriptions for the same accident type – and to handle multiple results from a single Long Range (LR) request, including a set of statistical results from a so-called 'Ensemble' run.

This feature is implemented in collaboration with the Danish Meteorological Institute (DMI) on whose HPC facility a single model run request from ARGOS in parallel produces a number of deterministic results (each in its own file) and a number of statistical results (all in the same file) – all based on the same input request but with differing source terms – from the ensemble of source terms – and with different versions of NWP model data. Statistical results will be available for the ensemble of NWP model data for each source term and for the combination of all source terms and all NWP model data.

Concentration Measurements in ARGOS

The ARGOS-DSS features several different options for visualising different kinds of radiological measurements. An example is shown below where a plot of European Monitoring Stations is presented in ARGOS. Station data are imported using the EURDEP-protocol, see Figure 77.
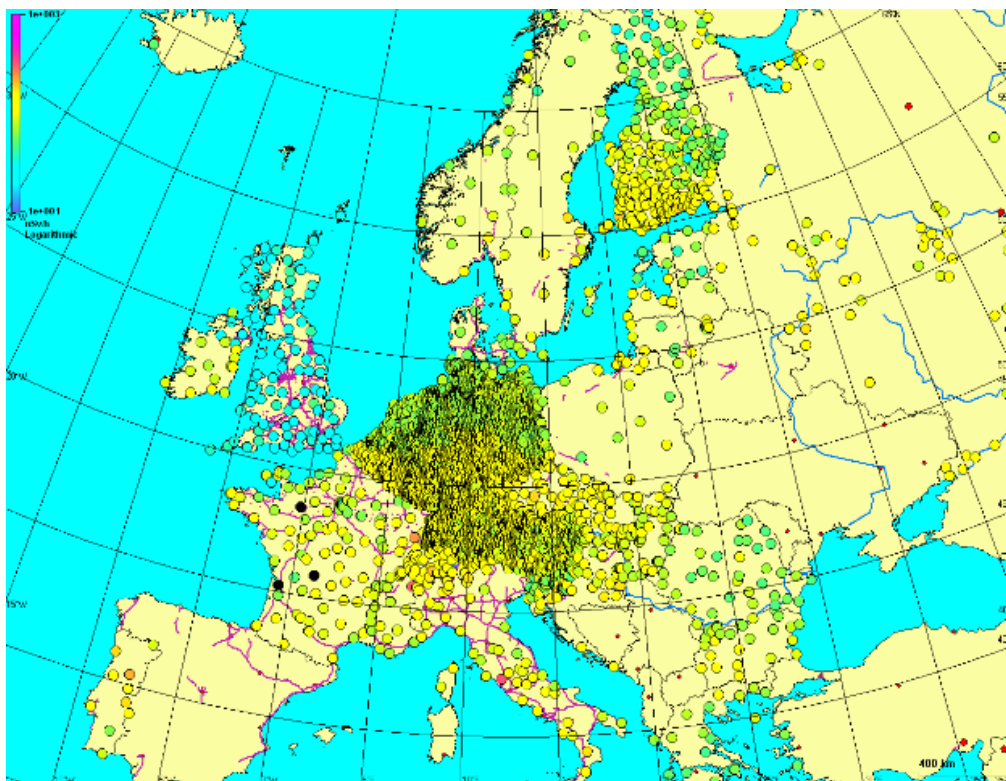
Figure 77 European Monitoring Stations presented in ARGOS.

The typical output from these types of Permanent Monitoring Stations is a dose rate; normal unit μSv/h.

Likewise, ARGOS is capable of importing and presenting data from Air Sample Stations – again importing data using the EURDEP-protocol. Typical output from these Air Sample Stations is an air concentration; normal unit Bq/m^3 (per nuclide).

Request for Source Localization Calculation from ARGOS

The existing Request dialog in ARGOS today is focused on doing forward Atmospheric Dispersion modelling; giving the user options for selecting a release point (a reactor) and a release description (source term – or ensemble of source terms) and a release time, see Figure 78.

Figure 78 Forward atmospheric dispersion modelling request dialog in ARGOS.

For Source Localization Calculations (SLC) the needs are quite different from (normal) forward ADM. The user needs to provide a (number of) detection(s) of time-average air concentrations to be part of the request sent to the model. As ARGOS already today have a module for presenting different measurements in the system (see section above) it would be natural to base the GUI for requesting SLC on the existing GUI for selecting measurement data to be visualized in the system. Due to the number of different types of measurement data, the GUI for selection is rather complicated, see Figure 78.

The needs for SLC can be narrowed down to these three parameters:

- The area of interest – the area from which the system should select measurement data
- The time frame of interest – the time period from which the system should select measurement data
- The type of measurements
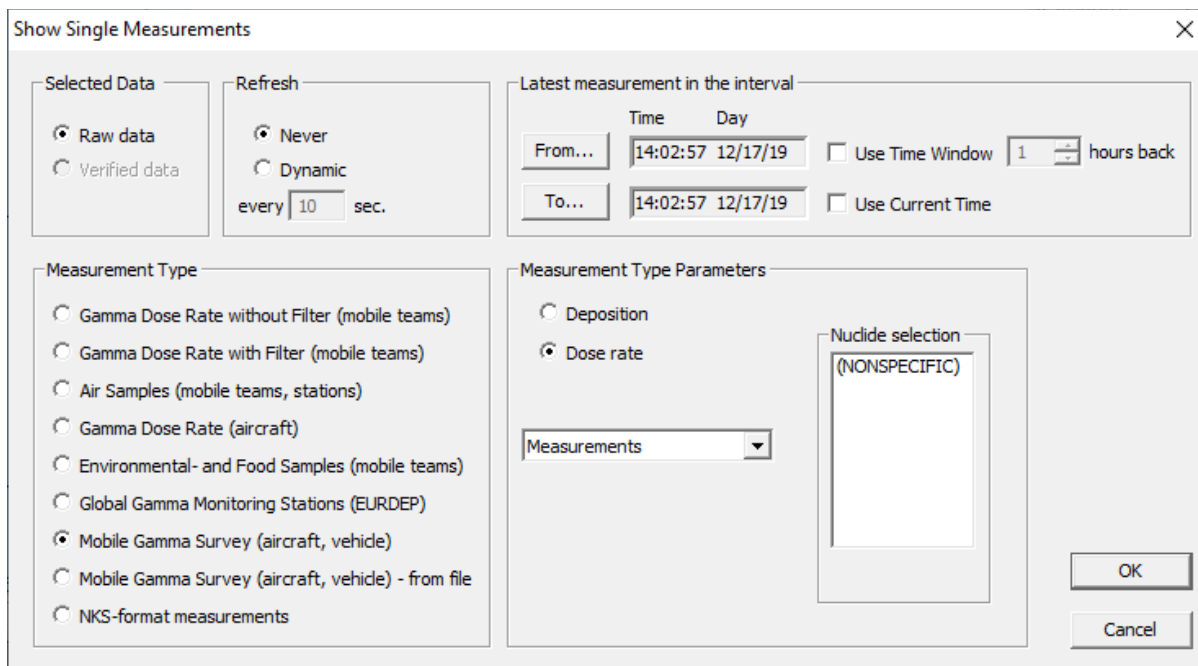
Figure 79 GUI for selecting measurement data to be visualized in the system.

Area of interest

The easiest way of defining the Area Of Interest (AOI) is to simply use the current map selection in the system – the part of the map that the user is viewing when the request is made. As an alternative, one could consider providing the user with the option of defining the AOI explicitly; giving the specific coordinates of the lower left and upper right corners of the AOI. Whereas, using traditional selections of AOI such as a radius around a release point has been deemed obsolete in this case; as there is no (known) release point.

Time period of interest

The simple setting of a "From time" and a "To time" will be maintained as the mean of selecting the time frame for sampling measurements that the system should select data for.

Do note that such a selection is necessary as some organizations are using their ARGOS installation as the primary source of storing (historical) measurement data. Thus the system can have measurement data for an arbitrary period back in time. However, when requesting an SLC, one will only have to provide data for the period in which elevated concentrations are recorded by at least part of the stations.

As Air Sampler Stations typically have substantial sampling periods, one will have to ensure that these periods are fully covered by the overall time period of interest.

Types of measurements

As can be seen from the GUI for visualising measurements in ARGOS above, ARGOS can handle quite many types of measurements. In order to simplify the GUI, we will restrict the selection for SLC to be limited to:
• Permanent Monitor Stations – dose rates
• Air Sampler Stations – air concentrations
Or a combination of the two.

It has to be considered how to distinguish between "lack of data" from a station and "below detection limit measurements". Of course, in the radiological domain there will always be some background radiation.

Permanent gamma-monitors and filter stations

In Europe, many radiological filter station measurements are taken once a week. However, in special cases it is possible to change to daily measurements. From a meteorological perspective, a week can be a long time covering a number of different meteorological phenomena taking place over the station site within the period. Additionally, a week could be longer than the accidental release. Thus, if the intended use of the measurements among other things is to assist in locating the release point, daily measurements are of much greater value. The filters are changed manually, and in most cases sent by regular mail for analysis. This implies a delay in retrieving the measurement data, and it means that short-lived radionuclei have decayed when the filter is measured.

The detection limit depends first of all on the amount of air drawn through the filter. Thus, the pump efficiency and the measurement period are key parameters for the detection limits, and therefore detection limits vary across Europe. In addition, the presence of many radionuclei on a filter makes it difficult to measure concentrations accurately.

There are currently no international agreements on routine distribution of filter station concentration measurements. For the October 2017 case of Ru-106 measurements in Europe, the IAEA collected the available filter station data (IAEA, 2017a,b).

The European Radiological Data Exchange Platform (EURDEP), see https://eurdep.jrc.ec.europa.eu/Entry/, is a network for the exchange of radiological monitoring data between most European countries. Currently, EURDEP is used for the European automatic gamma monitoring network which does not provide activity concentrations, only gamma dose rates. However, EURDEP might be used also for filter station measurements which could be very helpful in future events.

In comparison with filter-stations, the gamma monitoring network in Europe is much denser and reports automatically at high frequency, e.g. hourly, all of which make such data attractive for an operational nuclear DSS. However, in order to use the gamma-monitoring data for inverse modelling it is beneficial that measurements of nuclide-specific average activity concentrations are provided. Further, the measurement sensitivity is several orders of magnitude worse than for filter stations. Thus, gamma monitoring results are most likely only useful for source localization at the early phase of a nuclear accident.

The Comprehensive Nuclear-Test-Ban Treaty Organization (CTBTO) includes a monitoring network of 80 radiological stations measuring radioactive particles, around half of them also noble gasses. Near real time access to these data will be very helpful for locating an unknown release of radionuclei.

Presenting results from Source Localization Calculation in ARGOS

As part of the AVESOME NKS project (Sørensen *et al.,* 2020; 2019), the concept of presenting model results to the user in the form of time dependent probability plots was introduced together with the ability of dealing with percentile plots. This ability will be re-used to present the results from the SLC modelling.

In order to assist the user in pinpointing potential release sites and release periods, time series of inverse percentile plots can be superimposed with the ARGOS-database of nuclear facilities, see e.g. Figure 80 below. This applies both to cases where the atmospheric dispersion model has been run on deterministic numerical weather prediction model data and where it has been using ensemble-statistical meteorological data.

ETEX-1 case

In Figure 80, the 70th percentile of the inverse instantaneous concentration field in arbitrary units is shown at 0 UTC, 24 October, 1994. The time slider can be moved back and forth in time thereby showing the distribution at different time steps. The time series of these plots, corresponding to Figure 13, can be used for determining potential release locations and release periods. The actual ETEX release site in Monterfil is indicated in the plot.
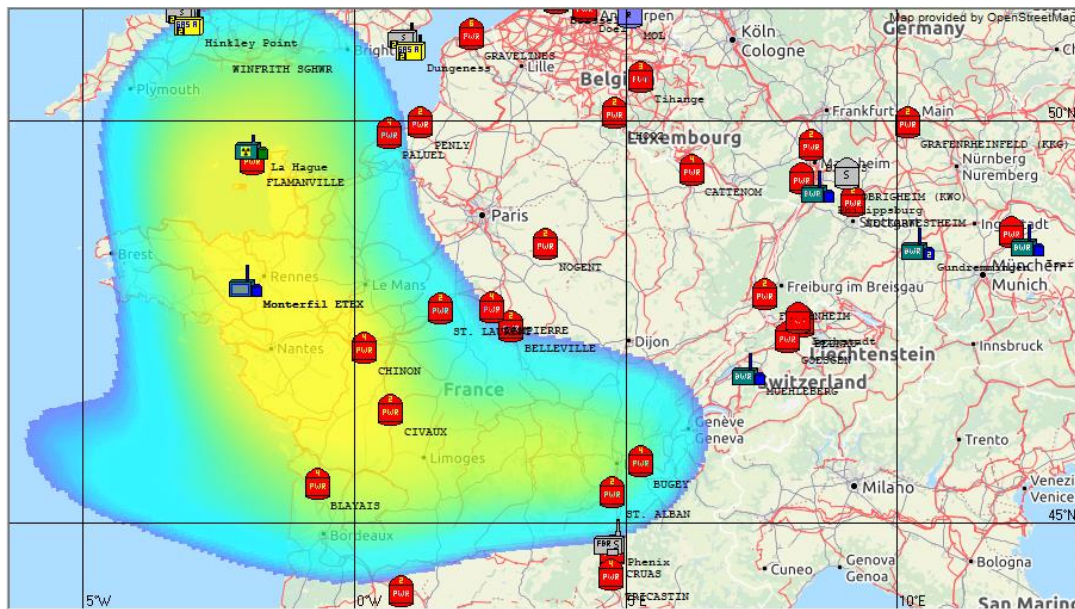
Figure 80 ARGOS presentation of the 70th percentile of Ensemble statistical SLC modeling for the ETEX-1 case, valid at 0 UTC, 24 October, 1994, superimposed with nuclear facilities and the ETEX release site at Monterfil.

Another possibility is to select a point on the map and present a time series plot for that particular point. In Figure 81 is shown such a time series plot of the 70th percentile of inverse concentration at the actual ETEX release site.
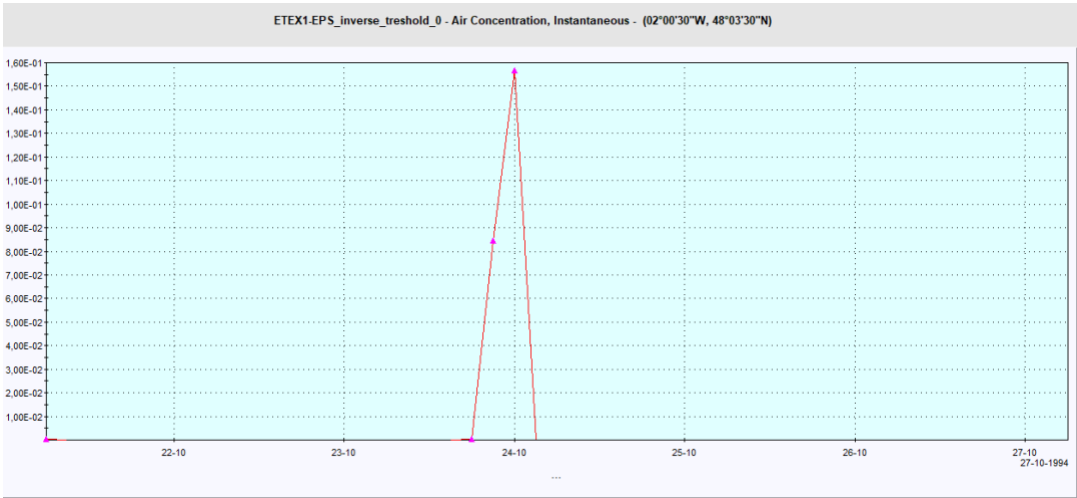
Figure 81 ARGOS presentation of a time series plot for the 70th percentile of Ensemble statistical SLC modelling for the ETEX-1 case at the actual release point.

Ru-106 case

In Figure 82, the 30th percentile of the inverse instantaneous concentration field in arbitrary units is shown at 3 UTC, 27 September, 2017. As for the ETEX-1 case, the time slider can be moved back and forth in time thereby showing the distribution at different time steps. The time series of these plots, corresponding to Figure 55, can be used for determining potential release locations and release periods. The NIIAR nuclear site is indicated in the plot.
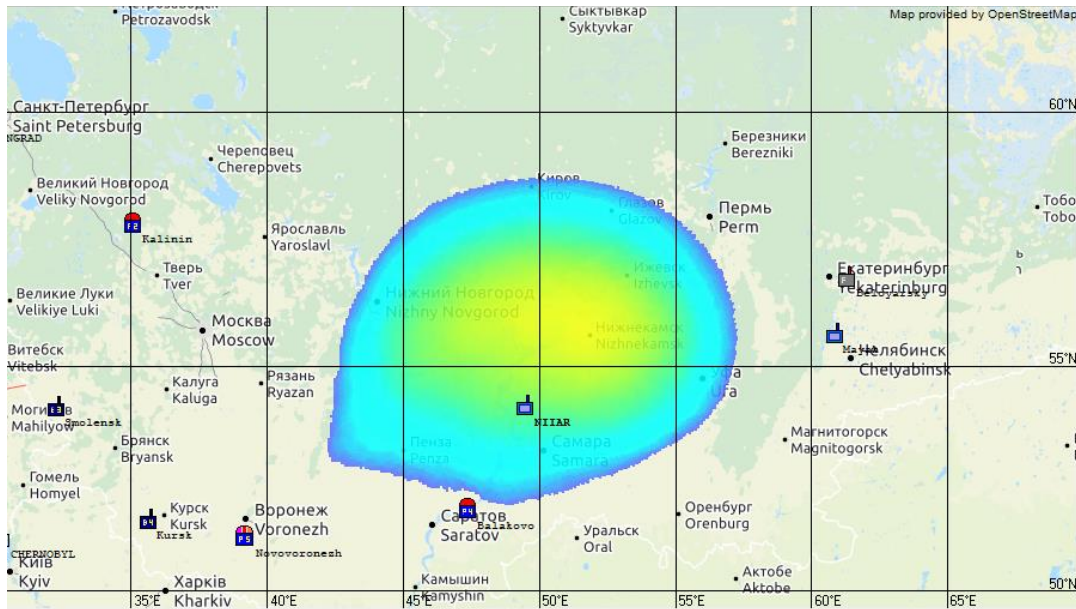
Figure 82 ARGOS presentation of the 30th percentile of Ensemble statistical SLC modelling for the Ru-106 case, valid at 3 UTC, 27 September, 2017, superimposed with nuclear facilities including the NIIAR site.

As already mentioned for the ETEX-1 case, another possibility is to select a point on the map and present a time series plot for that particular point. In Figure 83 is shown such a time series plot of the 30th percentile of inverse concentration at the NIIAR nuclear facility.
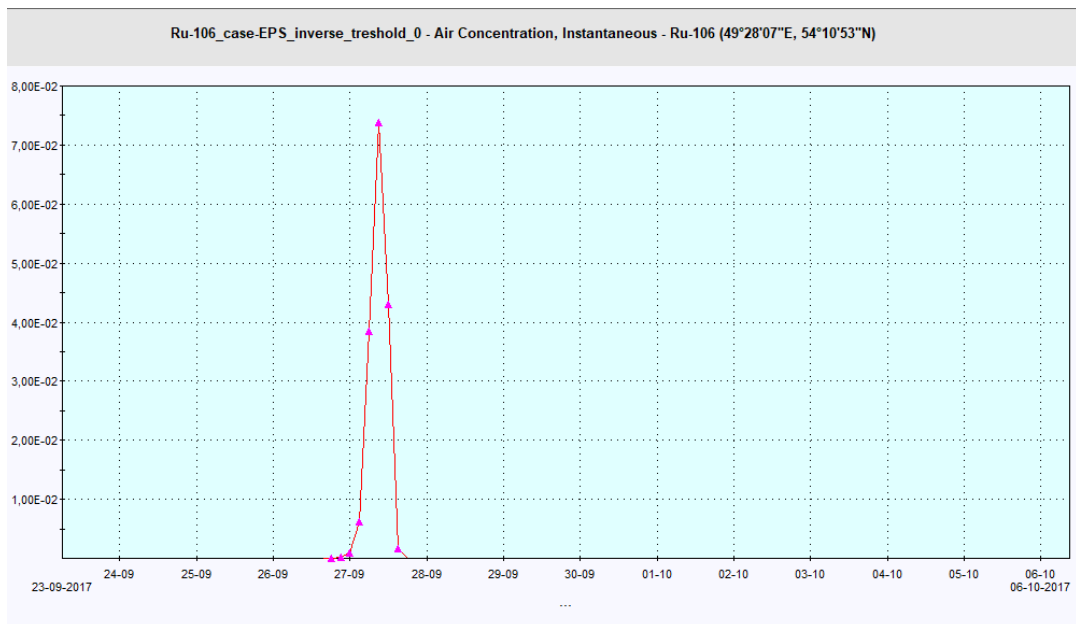
Figure 83 ARGOS presentation of a time series plot for the 30th percentile of Ensemble statistical SLC modelling for the Ru-106 case at the NIIAR nuclear facility.

In Figure 84 and Figure 85, similar plots are shown focusing on the Mayak nuclear facility.
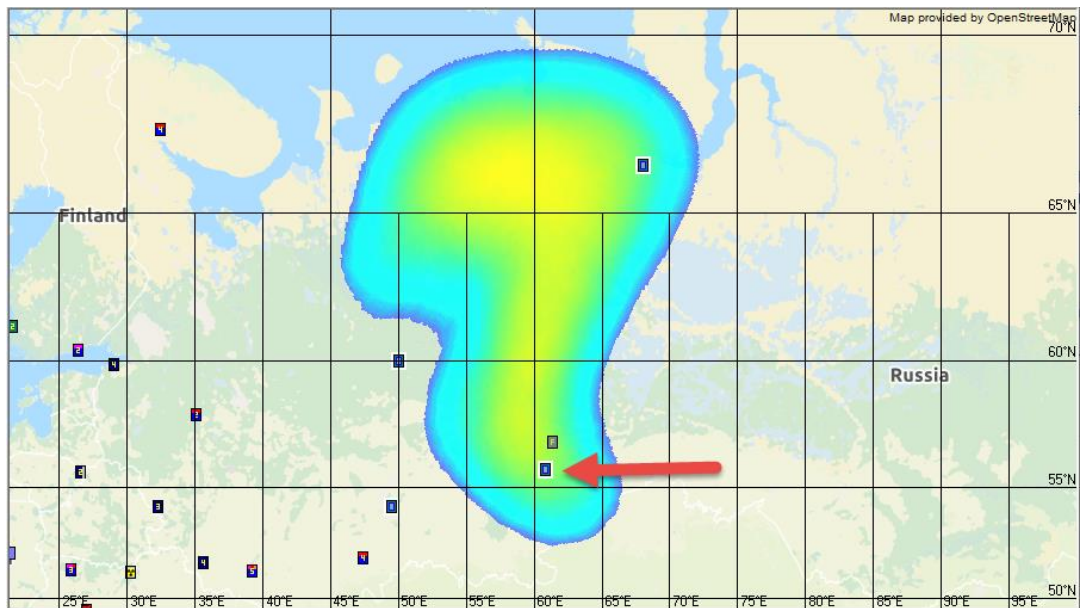
Figure 84 ARGOS presentation of the 30th percentile of Ensemble statistical SLC modelling for the Ru-106 case, valid at 12 UTC, 25 September, 2017, superimposed with nuclear facilities including the Mayak site indicated by a red arrow.
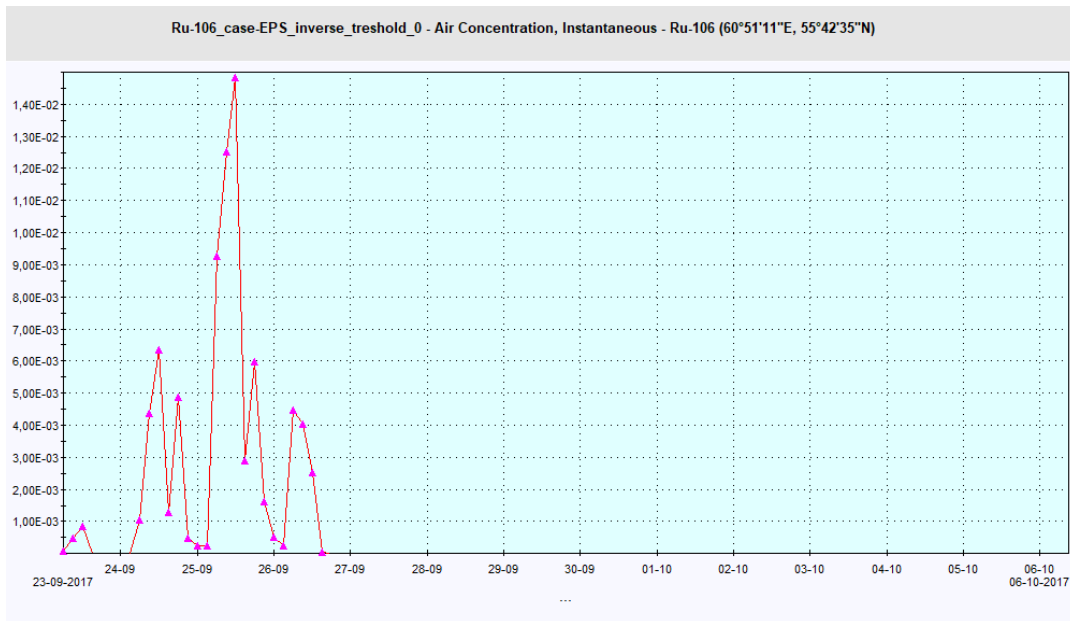

Figure 85 ARGOS presentation of a time series plot for the 30th percentile of Ensemble statistical SLC modelling for the Ru-106 case at the Mayak nuclear facility.

Conclusions and Outlook

Various methods for localization of an unknown source of radionuclides, which have been accidentally released to the atmosphere, are developed employing measurements of activity concentrations. The methods have been applied to two cases, viz. the European Tracer Experiment (ETEX) and the October 2017 case of Ru-106 in Europe.

For the two selected cases, deterministic numerical weather prediction model data have been obtained from the global model of the European Centre for Medium-Range Weather Forecasts (ECMWF). Furthermore, the Harmonie ensemble prediction system has been set up for these cases and run providing a 21-member ensemble describing the inherent meteorological uncertainties.

The atmospheric dispersion models DERMA, MATCH, SILAM and SNAP have been applied to the geographical and temporal localization problem. At first, the models used deterministic numerical weather prediction model data, and subsequently data of the Harmonie ensemble prediction system, whereby the effects of meteorological uncertainty on the determination of the release locations and release periods have been estimated.

From the given set of measured concentrations, inverse instantaneous activity concentration fields (for the Ru-106 case, inverse concentration fields for ETEX-1) are calculated by the dispersion models. An overlap method, described in terms of percentiles or in terms of a level of agreement approach, is applied to the intersection of these inverse concentration fields, whereby localization of the unknown source is provided for expert judgement in terms of geographical areas and release time periods. Another method utilises a simplified Bayesian approach on the set of inverse concentration calculations. Depending on the measured concentrations, the overlap areas and periods can be more or less extensive. A Markov Chain Monte Carlo approach could be a refinement, but in this case a qualified first guess of the source location has to be at hand. Finally, a four-dimensional variational (4D-VAR) method, as well as a simpler but much more expensive brute-force source-inversion approach have been applied.

The effects of the inherent meteorological uncertainties are quantified by incorporating the MUD methodology (Sørensen *et al.,* 2014) in the inverse modelling approach. As can be seen from the results obtained for the selected cases, the inherent meteorological uncertainty as expressed by the numerical weather prediction model ensemble does not seem to affect the geographic and temporal localization of the sources very much. The geographical distribution of filter stations and the measurement periods seem to play a much larger role, at least for both of the selected cases.

We have further seen that the inclusion of measurement data corresponding to week-long filter station sampling periods implies that the overlap plots become wider, and thus that the localization is less focused. This agrees well with the initial assumption that daily measurements are of greater value for localization purposes due to the fact that a week can cover a number of different meteorological phenomena taking place over the station site.

A number of different approaches have been employed for localizing the release point and release period of the selected cases. However, qualitatively the methods have provided similar results, and it is therefore not possible to prioritize these methods.

For the two selected cases, the available filter-station measurements are used. This mimics the situation at a late phase of an accidental release of radionuclides. At the early stage of an event, however, measurements will probably be available only from gamma monitoring networks. In this case, one should expect to have only gamma dose rates available given as the total of the various radionuclides released. Unfortunately, dose rate data are not directly applicable by all methods, since nuclide-specific concentration measurements are necessary to initialize the inverse models.

Treating the measured dose rates as concentrations can, however, be sufficient for source localization purposes. Such treatment of dose rates can be justified when the radiation dose is dominated by a single radionuclide or by a family of radionuclides which have comparable half-lives, and similar for the dose conversion factors. Without knowledge on nuclide composition, and if the half-life is long compared to the time span from the release to the measurement, the mean dose rate can in this case probably be treated as concentration of a non-depositing inert species.

The gamma stations in Europe are numerous and positioned densely, and they report frequently, e.g. hourly, and automatically, all of which make them attractive for source localization purposes. A disadvantage, however, is the detection limit, which is not as fine as for filter stations. Thus, especially in the early phase of an accidental release, gamma stations not too far from the release site may be useful. In a later phase, filter station data including stations far from the release site should replace the use of gamma station data.

As an outlook, methods for estimating the time-dependent emission profile for the various radionuclides detected should be developed for the locations that the various SLIM approaches point out to be of interest. These methods must be suited for operational use in nuclear DSSs, and they should include estimates of the inherent uncertainties. Previously, due to lack of computational power, ensemble-prediction methods could not be applied for operational real-time decision support. However, with modern supercomputing facilities available e.g. at national meteorological centres the proposed methodology should be feasible for real-time use, thereby adding value to decision support.

References

Andersson, C., Bergström, R., Bennet, C., Robertson, L., Thomas, M., Korhonen, H., Lehtinen, K.E.J., and Kokkola, H. 2015. MATCH-SALSA – Multi-scale Atmospheric Transport and CHemistry model coupled to the SALSA aerosol microphysics model – Part 1: Model description and evaluation. *Geosci. Model Dev.* **8**, 171–189. doi:10.5194/gmd-8-171-2015

Baklanov, A. and J. H. Sørensen. Parameterisation of radionuclide deposition in atmospheric dispersion models. *Phys. Chem. Earth* **26** (2001) 787–799

Baklanov, A., A. Mahura and J. H. Sørensen. Methodology for Prediction and Estimation of Consequences of Possible Atmospheric Releases of Hazardous Matter: 'Kursk' Submarine Study. Atmos. *Phys. Chem.* Vol. **3** (2003) 747–762

Bartnicki, J., H. Haakenstad, and Ø. Hov. Operational SNAP model for remote applications from NRPA. *Norwegian Meteorological Institute Report* (2011) 12–2011

Bartnicki, J., I. Amundsen, J. Brown, A. Hosseini, Ø. Hov, H. Haakenstad, H. Klein. Atmospheric transport of radioactive debris to Norway in case of a hypothetical accident related to the recovery of the Russian submarine K-27. *Journal of environmental radioactivity* **151** (2016) 404–416

Bengtsson, L., U. Andrae, T. Aspelien, Y. Batrak, J. Calvo, W, de Rooy, E. Gleeson, B. H. Sass, M. Homleid, M. Hortal, K.-I. Ivarsson, G. Lenderink, S. Niemelä, K. P. Nielsen, J. Onvlee, L. Rontu, P. Samuelsson, D. S. Muñoz, A. Subias, S. Tijm, V. Toll, X. Yang, and M. Ø. Køltzow. The HARMONIE–AROME Model Configuration in the ALADIN–HIRLAM NWP System. *Monthly Weather Review* (2017) **145** No. 5 https://doi.org/10.1175/MWR-D-16-0417.1

Casella, G., and George, E. I. (1992). Explaining the Gibbs sampler. *The American Statistician*, *46*(3), 167-174

ETEX web-site (2019), https://rem.jrc.ec.europa.eu/etex/

Frogner, I., Andrae, U., Bojarova, J., Callado, A., Escribà, P., Feddersen, H., Hally, A., Kauhanen, J., Randriamampianina, R., Singleton, A., Smet, G., van der Veen, S., and Vignes, O. HarmonEPS—The HARMONIE Ensemble Prediction System. *Weather and Forecasting* **34** (2019) 1909–1937

Gloster, J., A. Jones, A. Redington, L. Burgin, J. H. Sørensen, R. Turner. International approach to atmospheric disease dispersion modelling. *Veterinary Record* 03 (2010a) **166** (12):369. DOI:10.1136/vr.166.12.369a

Gloster, J., A. Jones, A. Redington, L. Burgin, J. H. Sørensen, R. Turner, P. Hullinger, M. Dillon, P. Astrup, G. Garner, R. D'Amours, R. Sellers and D. Paton. Airborne spread of foot-and-mouth disease – model intercomparison. *Veterinary Journal* **183** (2010b) 278–286

Graziani, G., Klug, W., and Nodop, K. Real-time Long-range Dispersion Model Evaluation of the ETEX First Release. **EUR 17754 EN** (1998) 92-828-3657-6 European Commission

Hastings, W. (1970). Monte Carlo sampling methods using Markov chains and their applications. *Biometrika* 57 (1), 97–109

Hersbach, H, Bell, B, Berrisford, P, et al. The ERA5 global reanalysis. *Q J R Meteorol Soc.* **146** (2020) 1999–2049. https://doi.org/10.1002/qj.3803

Hoe, S., J. H. Sørensen and S. Thykier-Nielsen. The Nuclear Decision Support System ARGOS NT and Early Warning Systems in Some Countries around the Baltic Sea. In: Proceedings of the 7th Topical Meeting on Emergency Preparedness and Response, September 14–17, 1999, Santa Fe, New Mexico, USA

Hoe, S., H. Müller, F. Gering, S. Thykier-Nielsen and J. H. Sørensen. ARGOS 2001 a Decision Support System for Nuclear Emergencies. In: Proceedings of the Radiation Protection and Shielding Division Topical Meeting, April 14–17, 2002, Santa Fe, New Mexico, USA

IAEA. Convention on Early Notification of a Nuclear Accident. (1986) https://www.iaea.org/publications/documents/treaties/convention-early-notification-nuclear-accident

IAEA. Updated Technical Attachment Status of Measurements of Ru-106 in Europe, 2017-10-20, 12:00 UTC, prepared by the Incident and Emergency Centre of the IAEA. Available through national radiation protection authorities. (2017a)

IAEA, Status of Measurements of Ru-106 and Ru-103 in Europe at 2017-11-24, 15:00 UTC, prepared by the Incident and Emergency Centre of the IAEA. Available through national radiation protection authorities. (2017b)

IRSN. Detection of Ruthenium 106 in France and in Europe: Results of IRSN's investigations. November 9, 2017 http://www.irsn.fr/EN/newsroom/News/Documents/IRSN_Information-Report_Ruthenium-106-in-europe_20171109.pdf

Kahnert, M., Variational data analysis of aerosol species in a regional CTM: Background error covariance constraint and aerosol optical observations operators, *Tellus*, 60B, 753-770, (2008)

Kahnert, M. (2018). Information constraints in variational data assimilation. *Q. J. R. Meteorol. Soc.* 144, 2230-2244

Keats, A., Yee, E., and Lien, F.-S. (2006). Bayesian inference for source determination with application to complex urban environment. *Atmospheric Environment,* 41, 465–479

Keats, A., Yee, E., Lien, F.-S., and D'Amours, R. (2008). Bayesian inversion of concentration data: Source reconstruction in the adjoint representation of atmospheric diffusion. *Journal of Wind Engineering,* 96, 1895–1816

Keller, J. D., Kornblueh, L., Hense, A. and Rhodin, A. Towards a GME ensemble forecasting system: Ensemble initialization using the breeding technique. *Meteorol. Z.* (2008)**17** (2008) 707–718

Klein, H., and Bartnicki**,** J. (2018). The Severe Nuclear Accident Programme, Concert Air2 Bulletin, Issue 24, 2018, page 4

Lauritzen, B., A. Baklanov, A. Mahura, T. Mikkelsen and J. H. Sørensen. K-model description of probabilistic long-range atmospheric transport in the Northern Hemisphere. *Atmos. Environ.* **40** (2006) 4352–4369

Lauritzen, B., A. Baklanov, A. Mahura, T. Mikkelsen and J. H. Sørensen. Probabilistic risk assessment for long-range atmospheric transport of radionuclides. *J. Envir. Radioactivity* **96** (2007) 110–115

Magnusson, L., Nycander, J. and Källén, E. Flow-dependent versus flow-independent initial perturbations for ensemble prediction. *Tellus* **61A** (2009) 194–209

Mahura, A., A. Baklanov and J. H. Sørensen. Methodology for evaluation of possible consequences of accidental atmospheric releases of hazardous matter. *Radiat. Prot. Dos.* **103** (2003) 131–139

Mahura, A. G., A. A. Baklanov, J. H. Sørensen, F. L. Parker, V. Novikov, K. Brown, K. L. Compton 2004: Assessment of Atmospheric Transport and Deposition Patterns Related to Russian Pacific Fleet Operations. *Environmental Monitoring and Assessment* **101** (2005) 261–287

Marchuk, G.I. Adjoint equations and analysis of complex systems. *Kluwer Academic Publisher* (1995)

Mosegaard, K., and Tarantola, A. (1995). Monte Carlo sampling of solutions to inverse problems. *Journal of Geophysical Research: Solid Earth*, *100*(B7), 12431-12447

Pudykiewicz, J. A. Application of adjoint tracer transport equations for evaluating source parameters. *Atmos. Environ.* **32** (1998) 3039–3050

Rao, S. Source estimation methods for atmospheric dispersion. *Atmos. Environ.* **41** (2007) 6964–6973

Mikkelsen, T., S. Alexandersen, H. Champion, P. Astrup, A. I. Donaldson, F. N. Dunkerley, J. Gloster, J. H. Sørensen and S. Thykier-Nielsen. Investigation of Airborne Foot-and-Mouth Disease Virus Transmission during Low-Wind Conditions in the Early Phase of the UK 2001 Epidemic. *Atmos. Chem. Phys. Disc.* **3** (2003) 677–703

PDC-ARGOS. http://www.pdc-argos.com

Press, W. H., Teukolsky, S. A., Vetterling, W. T., and Flannery, B. P. (2007). Numerical Recipes: The Art of Scientific Computing (3rd ed.). Section 19.5. Linear Regularization Methods. New York: Cambridge University Press. ISBN 978-0-521-88068-8

Robertson, L. and Langner, J. 1998. Source function estimate by means of variational data assimilation applied to the ETEX-1 tracer experiment. *Atmos. Environ.* **32**, 4219-4225

Robertson, L., Langner, J. and Engardt, M., An Eulerian limited-area atmospheric transport model, *J. Appl. Met.* 38, 190-210, 1999

Robertson, L. 2004. *Extended back-trajectories by means of adjoint equations.* Swedish Meteorological and Hydrological Institute, **RMK No. 105**, 37 pp.

Saltbones, J., A. Foss, and J. Bartnicki. Norwegian Meteorological Institute's real-time dispersion model SNAP (Severe Nuclear Accident Program): Runs for ETEX and ATMES II experiments with different meteorological input. *Atmospheric Environment* **32** no. 24 (1998) 4277–4283

Schubert, S. D. and Suarez, M. Dynamical Predictability in a Simple General Circulation Model: Average Error Growth. *Journal of Atmospheric Sciences* **46** (1989) 353–370

Seibert, P. Methods for source determination in the context of the CTBT radionuclide monitoring system. In: Proceedings Informal Workshop on Meteorological Modelling in Support of CTBT Verification, Vienna (2000)

Seibert, P. Inverse modelling with a Lagrangian particle dispersion model: application to point releases over limited time intervals. In: Gryning, S.E., Schiermeier, F.A. (Eds.), Air Pollution Modeling and its Application XIV (2001) Plenum Press, New York, pp. 381–389

Seibert, P. Inverse modelling of atmospheric trace substances on the regional scale with Lagrangian models. In: Proceedings of the EUROTRAC-2 Symposium, 11–15 March 2002, Garmisch-Partenkirchen, Germany (2002)

Senocak, I., N. W. Hengartner, M. B. Short, and W. B. Daniel. Stochastic event reconstruction of atmospheric contaminant dispersion using Bayesian inference. *Atmospheric Environment* **42** no. 33 (2008) 7718-7727

Smith, A., and Gelfand, A. (1992). Bayesian statistics without tears: A sampling-resampling perspective. *The American Statistician* 42 (2), 84–88

Sofiev, M., and Atlaskin, E. An example of application of data assimilation technique and adjoint dispersion modelling to an inverse dispersion problem based on the ETEX experiment. In: Air Polution Modelling and Its Applications XVII. Presented at the International Technical Meeting on Air Pollution Modelling and its applications (2004) Springer, pp. 61–65

Sofiev, M., Vira, J., Kouznetsov, R., Prank, M., Soares, J., and Genikhovich, E. Construction of the SILAM Eulerian atmospheric dispersion model based on the advection algorithm of Michael Galperin. *Geosci. Model Devel*. (2015) **8** 3497–3522

Sørensen, J.H., Bartnicki, J., Blixt Buhr, A.M., Feddersen, H., Hoe, S.C., Israelson, C., Klein, H., Lauritzen, B., Lindgren, J., Schönfeldt, F., Sigg, R. Uncertainties in atmospheric dispersion modelling during nuclear accidents. *J. Environ. Radioact.* **222** (2020) 1-10 https://doi.org/10.1016/j.jenvrad.2020.106356

Sørensen, J. H. Method for source localization proposed and applied to the October 2017 case of atmospheric dispersion of Ru-106. *Journ. Envir. Radioactivity* **189C** (2018) 221–226 https://doi.org/10.1016/j.jenvrad.2018.03.010 https://www.sciencedirect.com/science/article/pii/S0265931X18300146

Sørensen, J. H. Sensitivity of the DERMA Long-Range Dispersion Model to Meteorological Input and Diffusion Parameters. *Atmos. Environ.* **32** (1998) 4195–4206

Sørensen, J. H., D. K. J. Mackay, C. Ø. Jensen and A. I. Donaldson. An integrated model to predict the atmospheric spread of foot-and-mouth disease virus. *Epidemiol. Infect.* (2000) 124, 577–590

Sørensen, J. H., C. Ø. Jensen, T. Mikkelsen, D. Mackay and A. I. Donaldson. Modelling the atmospheric spread of foot-and-mouth disease virus for emergency preparedness. *Phys. Chem. Earth* **26** (2001) 93–97

Sørensen, J. H., A. Baklanov and S. Hoe. The Danish Emergency Response Model of the Atmosphere. *J. Envir. Radioactivity* **96** (2007) 122–129

Sørensen, J. H., B. Amstrup, H. Feddersen, U. S. Korsholm, J. Bartnicki, H. Klein, P. Wind, B. Lauritzen, S. C. Hoe, C. Israelson, and J. Lindgren. Meteorological Uncertainty of atmospheric Dispersion model results (MUD). **NKS-307** ISBN 978-87-7893-385-0, http://www.nks.org/en/nks_reports/view_document.htm?id=111010212220490 (2014)

Sørensen, J.H., B. Amstrup, H. Feddersen, J. Bartnicki, H. Klein, M. Simonsen, B. Lauritzen, S. C. Hoe, C, Israelson and J. Lindgren. Fukushima Accident: UNcertainty of Atmospheric dispersion modelling (FAUNA). **NKS-360** ISBN 978-87-7893-444-4 (2016), http://www.nks.org/scripts/getdocument.php?file=111010213440189

Sørensen, J. H., B. Amstrup, T. Bøvith, H. Feddersen, R. Gill, M. Sørensen, F. Vejen, P. Astrup, N. Davis, B. Lauritzen, S. C. Hoe, J. E. Dyve, P. Lindahl. MEteorological uncertainty of ShOrt-range dispersion (MESO). **NKS-380** ISBN 978-87-7893-466-6 (2017), http://www.nks.org/en/nks_reports/view_document.htm?id=111010214043891

Sørensen, J. H., Schönfeldt, F., Sigg, R., Pehrsson, J., Lauritzen, B., Bartnicki, J., Klein, H., Hoe, S. C., and Lindgren, J. Added Value of uncertainty Estimates of SOurce term and Meteorology (AVESOME) – final report. NKS-420, ISBN 978-87-7893-509-0 (2019) http://www.nks.org/en/nks_reports/view_document.htm?id=111010214696230

Termonia, P., Fischer, C., Bazile, E., Bouyssel, F., Brožková, R., Bénard, P., Bochenek, B., Degrauwe, D., Derková, M., El Khatib, R., Hamdi, R., Mašek, J., Pottier, P., Pristov, N., Seity, Y., Smolíková, P., Španiel, O., Tudor, M., Wang, Y., Wittmann, C., and Joly, A.: The ALADIN System and its canonical model configurations AROME CY41T1 and ALARO CY40T1. *Geosci. Model Dev.* **11** (2018) 257–281, https://doi.org/10.5194/gmd-11-257-2018

Tikhonov, A. N. Numerical methods for the solution of ill-posed problems. Kluwer Academic Publishers (1995)

Vira, J. and Sofiev, M. On variational data assimilation for estimating the model initial conditions and emission fluxes for short-term forecasting of SOx concentrations. *Atmospheric Environment* **46** (2012) 318–328 https://doi.org/10.1016/j.atmosenv.2011.09.066

Wotawa, G., L.-E. De Geer, P. Denier, M. Kalinowski, H. Toivonen, R. D'Amours, F. Desiato. Atmospheric transport modelling in support of CTBT verification—Overview and basic concepts. *Atmospheric Environment* **37**, no. 18 (2003) 2529-2537

Yee, E. (2008). Automated computational inference engine for Bayesian source reconstruction: Application to some detections/non-detections made in the CTBT International Monitoring System. *Journal of Wind Engineering* **96** 1895–1816.

Yee, E. (2012). Probability theory as logic: Data assimilation for multiple source reconstructions. *Pure Applied Geophysics* **169** 499–517.

Yee, E. Automated computational inference engine for Bayesian source reconstruction: Application to some detections/non-detections made in the CTBT International Monitoring System. *Applied Mathematical Sciences* **11** no. 32 (2017) 1581-1618.

Acknowledgements

Disclaimer
The views expressed in this document remain the responsibility of the author(s) and do not necessarily reflect those of NKS. In particular, neither NKS nor any other organisation or body supporting NKS activities can be held responsible for the material presented in this report.

Title	Source Localization by Inverse Methods (SLIM)
Author(s)	Jens Havskov Sørensen[1] (co-ordinator) Henrik Feddersen[1] Kasper Skjold Tølløse[1] Rostislav Kouznetsov[2] Mikhail Sofiev[2] Heiko Klein[3] Magnus Ulimoen[3] Lennart Robertson[4] Jan Pehrsson[5] Bent Lauritzen[6] Dan Bohr[7] Agnieszka Hac-Heimburg[7] Carsten Israelson[7] Anna Maria Blixt Buhr[8] Jonas Lindgren[8] Tero Karhunen[9] Tuomas Peltonen[9]
Affiliation(s)	[1]Danish Meteorological Institute (DMI) [2]Finnish Meteorological Institute (FMI) [3]Norwegian Meteorological Institute (MET Norway) [4]Swedish Meteorological and Hydrological Institute (SMHI) [5]PDC-ARGOS [6]Technical University of Denmark (DTU) [7]Danish Emergency Management Agency (DEMA) [8]Swedish Radiation Safety Authority (SSM) [9]Radiation and Nuclear Safety Authority (STUK)
ISBN	978-87-7893-549-6
Date	March 2022
Project	NKS-B / SLIM
No. of pages	94
No. of tables	0
No. of illustrations	85
No. of references	67

Abstract
max. 2000 characters

In early October 2017, the IAEA was informed that low concentrations of Ru-106 were measured in high-volume air samples in Europe from routine monitoring networks. However, no information was given that an accidental release of Ru-106 had taken place. Such events signify the need for prompt and accurate responses from national radiation protection authorities in such cases. This requires that methodologies, suited for operational use, are developed for spatial and temporal localization of the source of contamination based on available monitoring data.

For operational use, nuclear decision-support systems should be extended with modules handling such monitoring data automatically, e.g. by employing EURDEP, and conveying selected data to the national meteorological centre accompanied by a request to run an atmospheric dispersion model in inverse mode. The aim would be to determine a geographical area in which to find the potential release point as well as the release period.

The following results are obtained:
- Two case studies are identified and selected, viz. the European Tracer Experiment (ETEX-1) and the October 2017 case of Ru-106 in Europe.
- Methods for temporal and spatial source localization are developed, implemented and described.
- Deterministic NWP model data are derived from the ECMWF corresponding to the selected cases.
- Quality-controlled measurement data of ground-level concentration are obtained from filter stations.
- The inverse methods for source localization are applied by using the DERMA, MATCH and SNAP atmospheric dispersion models to both cases using the deterministic meteorological data.
- A high-resolution limited-are ensemble prediction system based on the Harmonie NWP model has been set up and applied to the two selected cases.
- The inverse methods for source localization are applied by using the DERMA, MATCH, SILAM and SNAP atmospheric dispersion models to both cases using the ensemble-statistical meteorological data.

Key words

nuclear emergency preparedness, atmospheric dispersion model, source localization, inverse modelling, concentration measurements, uncertainty